Doctoral Dissertation

Comprehensive Study of Lithium Electrodeposition Mechanisms by Elucidating Diffusion Phenomena Using In-Situ Observation Techniques

その場観察技術を活用した

拡散現象の解明によるリチウム電析機構の包括的研究

March, 2025

Graduate School of Engineering, Hokkaido University

Division of Materials Science

Laboratory of Materials for Sustainable Engineering

北海道大学 大学院工学院材料科学専攻　環境材料学研究室

KAMESUI Go

亀水 豪

HOKKAIDO UNIVERSITY

Table of Contents

Chapter 1: General Introduction

1.1 Geopolitical significance of introducing renewable energy in Japan

The global transition toward renewable energy (RE) systems represents a fundamental shift in energy infrastructure, driven by environmental concerns and technological advances. Within this context, Japan's unique geographical, climatic, and cultural characteristics position it as a particularly compelling case study for RE implementation.

Japanese archipelagic geography presents distinctive opportunities for RE development. The nation's extensive coastline, stretching approximately 35,000 kilometers, offers substantial potential for tidal and wave power generation. The mountainous topography, encompassing 70 % of the land area, provides optimal conditions for geothermal and small-scale hydroelectric power installations. Moreover, the temperate climate, characterized by pronounced seasonal variations, facilitates diverse RE applications: abundant solar radiation supports photovoltaic systems, while seasonal wind patterns enable efficient wind power generation.

These natural advantages acquire heightened significance when considered against Japan's energy security challenges. The nation's extreme dependence on imported energy resources—approximately 94 % of its primary energy supply—creates substantial economic and geopolitical vulnerabilities. This situation is particularly concerning given the concentration of fossil fuel supplies in politically volatile regions, notably the Middle East. Historical events, such as the 1973 oil crisis, have demonstrated the potential severity of such dependencies.

Japan's location on the Pacific Ring of Fire introduces additional complexities to its energy infrastructure requirements. The frequency of seismic and volcanic activity necessitates robust and resilient energy systems. The 2011 Great East Japan Earthquake

and subsequent Fukushima nuclear disaster starkly illustrated the vulnerabilities of centralized energy infrastructure, particularly large-scale thermal and nuclear power facilities. This event catalyzed a fundamental reassessment of Japan's energy strategy, highlighting the potential advantages of distributed RE systems in enhancing disaster resilience.

The imperative for RE implementation extends beyond immediate practical considerations into the realm of cultural and historical significance. Japanese civilization has historically maintained a sophisticated relationship with nature, exemplified by the concept of "yaoyorozu no kami" (eight million deities) documented in the Kojiki, Japan's oldest historical record.[1] This traditional worldview, emphasizing harmonious coexistence with natural forces, provides a cultural foundation for modern RE adoption. The Japanese approach of maximizing natural benefits while maintaining vigilance against potential threats aligns remarkably well with RE system characteristics.

Recent geological predictions regarding the Nankai Trough megathrust and Tokyo inland earthquakes add urgency to the implementation of distributed energy systems. These impending seismic events, with potentially catastrophic implications for centralized infrastructure, underscore the strategic importance of developing robust, decentralized RE networks. The development of RE technologies also presents significant economic opportunities. Japan's established technological expertise and industrial infrastructure position it favorably to advance RE innovation. Success in this domain could strengthen Japan's international competitiveness while contributing to global sustainable development goals.

Thus, the strategic implementation of RE in Japan serves multiple interconnected objectives: enhancing energy security, reducing geopolitical vulnerabilities,

strengthening disaster resilience, and maintaining cultural continuity. This multifaceted approach demonstrates how RE adoption can address both immediate practical concerns and longer-term societal aspirations.

1.2 Challenges for the social implementation of renewable energy

1.2.1 The structure of energy dependence in modern society

Modern civilization fundamentally depends on sophisticated electrical infrastructure. The emergence of Cyber-Physical Systems, as proposed in Society 5.0, has deepened this dependence. The proliferation of Internet of Things devices is creating a society where everything, from industrial equipment to household appliances, is interconnected and controlled through network communication.

This social transformation brings innovative changes to industrial structures and lifestyles. However, it also creates new demands on power supply systems. Several challenges have emerged: increased power consumption from rapidly expanding data centers, charging infrastructure development for electric vehicles, and the need for high-quality power supply for smart factories.

The 2018 Hokkaido Eastern Iburi Earthquake exposed the vulnerability of this technology-dependent society. The blackout, triggered by the shutdown of the Tomato-Atsuma thermal power plant, revealed critical issues in the centralized power supply model. It highlighted several problems: the vulnerability of large-scale centralized power systems, cascading failure of social functions during widespread outages, and inadequate backup systems for critical infrastructure.

Under these circumstances, ensuring power supply stability has become a national priority. The acceleration of digital transformation demands higher power quality and supply reliability. Various measures are now essential to strengthen power system resilience. These include promoting distributed power sources and developing energy storage systems.

1.2.2 Challenges of renewable energy

Renewable energy (RE) has attracted significant attention as a promising solution to power supply challenges. The major types of RE exhibit the following characteristics[2,3];

Table 1. Comparison of renewable energy characteristics.

ENERGY SOURCE	ADVANTAGE	DISADVANTAGE
SOLAR POWER	Ease of installation and maintenance	Weather-dependent No night-time power generation
GEOTHERMAL POWER	Stable output Weather independent	Geographical restrictions Initial investment costs
TIDAL POWER	High predictability Stability	Installation site restrictions Impact on marine ecosystems
WIND POWER	High power generation efficiency Night-time power generation	Weather dependent Noise problems

The main technical challenge of RE systems is their output instability. Energy Storage Systems (ESS) are being developed as a solution to this challenge. Major ESS technologies include lithium-ion batteries, hydrogen energy storage, and flow batteries. For full-scale social implementation of RE, key challenges include advancing power generation forecasting through AI utilization and improving operational efficiency. While RE systems are expected to play an important role in strengthening disaster resilience, overcoming technical and economic challenges is essential. In particular, the advancement of storage systems is a key factor in the widespread adoption of RE.

1.3 The importance of developing secondary batteries

1.3.1 Technical requirements for next-generation rechargeable batteries

The development of high-performance secondary batteries has emerged as a crucial challenge in large-scale RE implementation. The lithium-ion battery (LIB), commercialized in 1992 through joint development by Asahi Kasei and Sony[4], significantly contributed to the widespread adoption of portable electronic devices. Its innovativeness was recognized with the 2019 Nobel Prize in Chemistry. While LIBs are planned for use in electric vehicles (EVs) and satellites, these applications require further improvements in energy density.

The energy density, a key performance indicator for secondary batteries, is expressed as the product of terminal voltage and electrode capacity. Based on this theoretical framework, this study proposes two approaches: revolutionary enhancement of electrode capacity using lithium metal anodes and expansion of operating voltage range through highly concentrated electrolytes.

1.3.2 Properties and problems of lithium metal anodes

Lithium metal possesses the lowest density (0.53 g cm^{-3}) among metals, combined with the lowest standard electrode potential (-3.04 V vs. SHE) and highest theoretical capacity (3,860 mAh g^{-1})[5–7]. These characteristics make it ideal as an anode material for next-generation secondary batteries, and it has long been used in primary batteries. However, its application in secondary batteries faces a fundamental challenge: dendrite growth.

During lithium electrodeposition in charging, the deposition morphology tends to be non-uniform. This non-uniformity is exacerbated by repeated charge-discharge cycles, potentially leading to serious problems such as short circuits from dendrite growth,

degradation of cycle characteristics, and fire hazards. Various approaches have been attempted to address this challenge.

The control of the solid electrolyte interphase (SEI) formed on the electrode surface is the most fundamental and important strategy. SEI forms immediately after starting electrochemical reaction through decomposition of electrolyte species, and its thickness and constituent elements significantly influence Li deposition morphology[8]. Previous studies have explored SEI composition optimization using additives[9] and artificial SEI formation[10]. Physical approaches include the introduction of three-dimensional porous structures to homogenize Li deposition sites[11], pressure-controlled deposition morphology[12], and deposition rate control through pulse electrolysis[13].

Combined strategies integrating these individual approaches have been proposed. However, no method has achieved complete resolution yet. New control methods based on deeper understanding of dendrite growth mechanisms are needed, particularly regarding the correlation between SEI formation processes and deposition morphology.

1.3.3 Highly Concentrated Electrolytes

The development of lithium-based electrolytes has progressed through three distinct generations.[14–16]

Conventional electrolytes, typically containing lithium salt concentrations around 1 mol L^{-1}, have been extensively studied and commercialized. These systems commonly employ carbonate-based solvents such as ethylene carbonate, dimethyl carbonate, diethyl carbonate, and ethyl methyl carbonate. The most widely used lithium salt is lithium hexafluorophosphate, though alternatives like lithium tetrafluoroborate, lithium perchlorate, and lithium bis(trifluoromethanesulfonyl) amide have also been

investigated. Conventional electrolytes demonstrate excellent ionic conductivity and well-established manufacturing processes. However, their organic solvents are highly flammable and show limited electrochemical stability, leading to continuous SEI formation and active lithium consumption.[17] Their poor thermal stability and salt concentration polarization during high-rate operation present additional challenges.

Highly concentrated electrolytes (HCEs), containing lithium salt concentrations above 3 mol L^{-1}, feature almost complete coordination between solvent molecules and Li^{+}[18,19]. The increased solvent molecule-Li^{+} interactions result in excellent properties including non-flammability and wide potential windows.[20–22]. However, their high viscosity and low conductivity tend to cause non-uniform Li deposition.

The latest innovation, locally highly concentrated electrolytes (LHCEs), are created by diluting HCEs with non-coordinating solvents.[23]。 Despite lithium salt concentrations of 1-2 mol L^{-1}, LHCEs maintain the Li^{+} coordination environment of HCEs. They successfully combine the advantages of HCEs' non-flammability and wide potential windows with low viscosity and high conductivity.

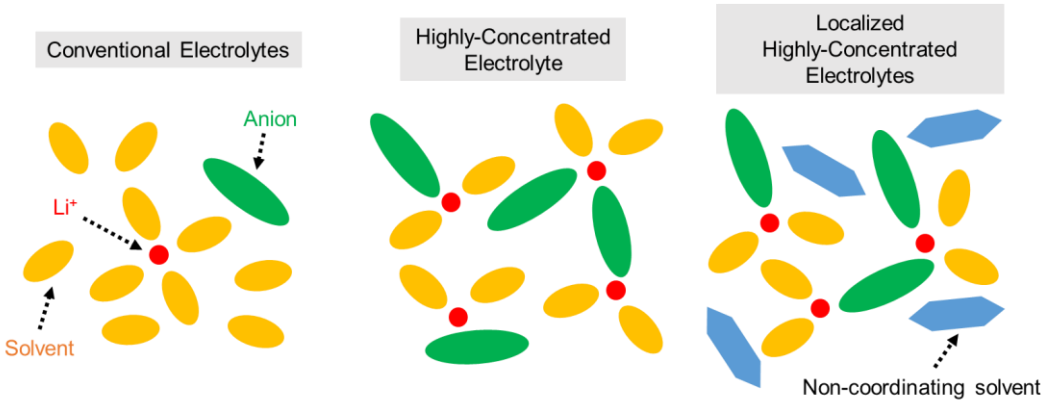

Figure 1. Schematic of the coordination state of chemical species in the electrolyte.

As shown in Figure 1, these structural differences between electrolyte systems

directly influence their physicochemical properties and electrochemical stability. Due to their excellent characteristics, LHCEs are attracting significant attention as next-generation battery electrolytes.

1.3.4 Next-Generation Storage Batteries

Table 2. Characteristics and Development Status of Next-Generation Lithium Metal Batteries

BATTERY TYPE	KEY FEATURES	TECHNICAL CHALLENGES
LITHIUM-SULFUR	Energy density of 400-600 Wh kg^{-1} Low cost material	Polysulfide shuttle effect Poor sulfur conductivity Limited cycle life
ALL-SOLID-STATE	Energy density of 400-700 Wh kg^{-1} High safety Bipolar stacking capability	Interface resistance Mechanical stress during cycling Manufacturing complexity
LITHIUM-AIR	Ultra-high theoretical energy density (3505 Wh kg^{-1}) Abundant cathode material (O_2)	Poor cycle efficiency Air impurity effects Complex reaction mechanisms

The pursuit of higher energy density storage systems has led to increased interest in secondary batteries utilizing lithium metal anodes. These next-generation systems promise theoretical energy densities several times higher than conventional lithium-ion batteries (200-250 Wh kg^{-1}). Table 2 summarizes the key characteristics, challenges, and commercialization prospects of three prominent candidates.

Lithium-sulfur batteries represent the most mature technology among these candidates.[24] Their cathodes typically comprise sulfur dispersed in conductive carbon matrices, while ether-based electrolytes or highly-concentrated electrolytes are chosen for their compatibility with polysulfide intermediates. Several groups have demonstrated

prototype cells with energy densities exceeding 500 Wh kg^{-1}.[25] However, the polysulfide shuttle effect—where dissolved sulfur species migrate between electrodes—remains a critical challenge, along with poor cycling stability.

All-solid-state batteries offer a promising approach to achieving both high energy density and safety through the elimination of flammable liquid electrolytes. Two main classes of solid electrolytes are being developed: oxides (e.g., $Li_7La_3Zr_2O_{12}$) offering high stability,[26] and sulfides (e.g., $Li_{10}GeP_2S_{12}$) providing high ionic conductivity.[27] A distinctive advantage of solid electrolytes is their single-ion conducting nature, resulting in a lithium-ion transference number of unity. This characteristic eliminates concentration polarization issues common in liquid electrolytes and enables more stable, high-rate operation. The solid-state architecture enables the use of high-voltage cathode materials and bipolar stacking, potentially leading to high energy densities. However, challenges in interface resistance and mechanical stress during cycling require further research.

Lithium-air batteries present the highest theoretical energy density but face the most significant technical challenges.[28] These systems utilize a porous carbon cathode where atmospheric oxygen is reduced during discharge, forming Li_2O_2 or LiOH depending on the electrolyte system. The complexity of oxygen reduction and evolution reactions, combined with sensitivity to air impurities, makes practical implementation particularly challenging.

A common thread among these next-generation systems is their reliance on lithium metal anodes, which offer the highest theoretical capacity (3860 mAh g^{-1}) among anode materials. However, unstable lithium deposition leading to dendrite formation presents a universal challenge across all these technologies. Understanding and

controlling lithium electrodeposition mechanisms is therefore crucial for realizing the practical potential of next-generation batteries. The fundamental insights gained from studying lithium deposition behavior will be essential for developing effective strategies to enable stable, long-term cycling of these advanced energy storage systems.

1.4 Mass transfer phenomena and deposition phenomena in electrolytes

Mass transport mechanisms of metal ions in electrolytes are governed by three fundamental transport phenomena: convection, diffusion, and migration[29]. In electrode surface reaction processes, these transport phenomena interact complexly to control the supply of reactants and removal of products. This section details the physicochemical nature of these transport phenomena.

1.4.1 Convection

Convection can be classified into two types. Natural convection occurs spontaneously due to density gradients arising from temperature or concentration differences in fluids, driven by buoyancy and gravity to eliminate density inhomogeneities. Forced convection is flow artificially created by external forces such as pumps, fans, or suction devices.

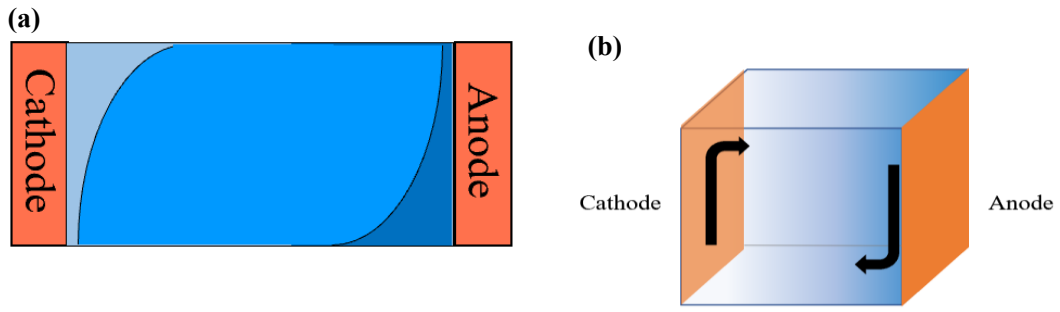

Figure 2. Schematic of (a) density distribution and (b) natural convection.

In electrochemical reactions, natural convection is induced by local changes in ion concentration near electrodes, creating density gradients, as shown in Figure 2. Forced convection, deliberately generated by mechanical forces, is utilized for mass transport control using devices such as rotating ring-disk electrodes (RRDE)[30].

1.4.2 Diffusion

Diffusion is spontaneous mass transport driven by concentration gradients. The diffusion flux in steady state is described by Fick's first law[31];

$$J = -D\frac{dc}{dx} \quad (1)$$

where J [mol s^{-1} cm^{-2}] is the mass flux and D [cm^2 s^{-1}] is the diffusion coefficient. The diffusion coefficient characterizes the amount of substance passing through unit area per unit time. For non-steady state systems where concentration and concentration gradients change with time, Fick's second law applies.

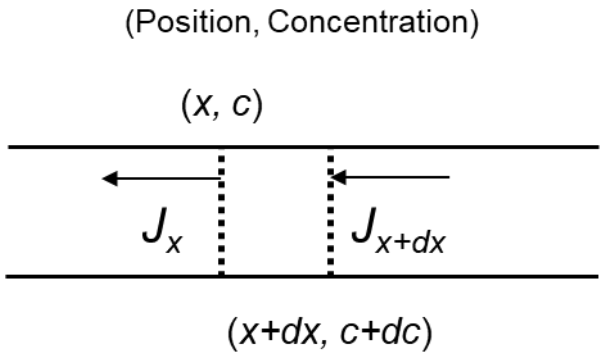

Figure 3. Time change of a concentration in a certain place.

Consider the temporal concentration change in a section dx between positions x and $x+dx$ in a rod with unit cross-sectional area (Figure 3). For concentration c at x and $c+dc$ at $x+dx$, with $\partial c/\partial t>0$, diffusion occurs from higher to lower concentration. The time change of concentration within dx is

$$\frac{\partial c}{\partial t} = \frac{J_x - J_{x+dx}}{dx} \tag{2}$$

using Eq. 1, Eq. 2 can be transformed into Eq. 3;

$$J_x = -D\left(\frac{\partial c}{\partial x}\right)_x \tag{3}$$

J_{x+dx} can be replaced by the following equation;

$$J_{x+dx} = J_x + \left(\frac{\partial J}{\partial x}\right)_x dx = -D\left(\frac{\partial c}{\partial x}\right)_x - \frac{\partial}{\partial x}\left(D\frac{\partial c}{\partial x}\right)_x dx \tag{4}$$

Given that D is a constant, Eq. (5) can be obtained from Eqs. (2), and (3);

$$\frac{\partial c}{\partial t} = D\frac{\partial^2 c}{\partial x^2} \tag{5}$$

Using Laplacce transform, the concentration function, *C(x,t)*, dependent on position and time can be expressed as

$$C(x,t) = C(\infty,t) \pm \frac{2i(1-t^+)}{zF\sqrt{D}}\sqrt{\frac{t}{\pi}}\, exp\left(-\frac{x^2}{4Dt}\right) + \frac{ix}{zFD}\, efrc\frac{x}{\sqrt{4Dt}} \tag{6}$$

where z is the valence, F is Faraday's constant, i is the applied current density, and t^+ is the transference number of cation. The erfc function is the complementary error function and can be written as

$$erfc(x) = \frac{2}{\sqrt{\pi}} \int_{x}^{\infty} e^{-t^2}\, dt = 1 - erf(x) \tag{7}$$

$$erf(x) = \frac{2}{\sqrt{\pi}} \int_{0}^{x} e^{-t^2}\, dt \tag{8}$$

At the electrode surface ($x = 0$), the concentration change with time is written as

$$C(0,t) = C(\infty,t) \pm \frac{2i(1-t^{+})}{zF\sqrt{D}} \sqrt{\frac{t}{\pi}} \tag{9}$$

Under diffusion-controlled ideal conditions, the surface concentration varies linearly with the square root of time.

The reaction current can be expressed using flux *J*;

$$i = zFJ \tag{10}$$

Here, diffusion dominates the transport of the solute near the electrode surface. Hence, by using Eq. (3) and the diffusion layer thickness δ, Eq. (10) becomes Eq. (11).

$$i = zFD\,\frac{C(\infty,t) - C(0,t)}{\delta} \tag{11}$$

Under diffusion-limited conditions, where $C(0, t) = 0$, Eq. 11 can be transferred as below;

$$i = zFD\frac{C(\infty, t)}{\delta} \tag{12}$$

Substituting Eq. (12) into Eq. (9) leads to the equation for obtaining D from δ;

$$D = \frac{\pi}{4}\left(\frac{\delta}{\sqrt{t}}\right)^2 \tag{13}$$

This study used equation (14) for D calculation in section 6.

1.4.3 Migration

Migration is a phenomenon where charged particles move in an electric field driven by electrostatic forces[29]。 In electrical circuits, electrons conduct in electrodes while ions serve as charge carriers in electrolytes. The migration flux J_m in electrochemical systems is described by the Nernst-Planck equation;

$$J_m = -uzFC\frac{\partial \varphi}{\partial x} \tag{14}$$

where u is the ionic mobility, z is the charge number, F is Faraday's constant, C is ion concentration, and φ is potential. The Einstein-Smoluchowski relation connects mobility u and diffusion coefficient D;

$$D = ukT \tag{15}$$

where k is the Boltzmann constant and T is absolute temperature.

The transference number is defined as the fraction of total current carried by a specific ionic species. In binary electrolytes, the transport number t_+ for cations is expressed as;

$$t^+ = \frac{z^+ u^+ C^+}{z^+ u^+ C^+ + z^- u^- C^-} \tag{16}$$

where subscripts + and - denote cations and anions, respectively. Under the electroneutrality condition in ideal binary electrolytes, the relationship below holds true;

$$z^+ C^+ = z^- C^- \tag{17}$$

This condition simplifies the transference number to;

$$t^+ = \frac{u^+}{u^+ + u^-} \tag{18}$$

In practical electrochemical measurements, transference numbers are evaluated using direct current (DC) polarization or AC impedance methods. The DC method employs the Bruce-Vincent equation[32];

$$t^+ = \frac{I_s(\Delta V - I_0 R_0)}{I_0(\Delta V - I_s R_s)} \tag{19}$$

where I_0 and Is are initial and steady-state currents, R_0 and Rs are initial and steady-state resistances, and ΔV is applied voltage.

In practical electrochemical systems, supporting electrolytes are added to increase solution conductivity and control migration contributions to mass transport. This addition reduces solution resistance, enables precise potential control, and promotes charge transfer reactions through electric double layer compression. For lithium-ion battery electrolytes, optimizing Li^+ transference numbers is key to improving charging rates. Highly concentrated and localized highly concentrated electrolytes have been developed to enhance Li^+ transport numbers[23]。 Under sufficiently high supporting electrolyte concentrations, potential gradients in the electrolyte are moderated, and mass transport becomes primarily diffusion-controlled. Under these conditions, the Nernst-Planck equation theoretically reduces to Fick's law.

1.4.4 Mass transfer and electrode reaction rates

Electrode reaction rates are governed by two factors: charge transfer processes and mass transport processes[29]. The overall reaction rate is determined by the slowest step (rate-determining step) among these processes. Understanding this interplay is fundamentally important for controlling and optimizing electrochemical reactions.

For electrochemical reactions at electrode surfaces, a general electron transfer reaction between oxidized species O and reduced species R can be expressed as:

$$O + ze^- \rightleftarrows R \tag{20}$$

The net current density i is expressed as the difference between cathodic current density i_c and anodic current density i_a;

$$i = i_c - i_a \tag{21}$$

According to the Butler-Volmer equation, these partial current densities are expressed as:

$$i = i_0\{\exp(-\alpha zF\eta/RT) - \exp(1-\alpha)\, zF\eta/RT\} \tag{22}$$

where i_0 is the exchange current density, α is the transfer coefficient, η is the overpotential, F is Faraday's constant, R is the gas constant, and T is absolute temperature. This equation serves as the fundamental expression quantitatively describing the relationship between activation barriers and overpotential in electrode reactions.

When mass transport is involved in electrode reactions, the ratio of reactant concentrations at the electrode surface C (0, t) to bulk solution C (∞, t) must be considered. The modified Butler-Volmer equation becomes follows[33];

$$i = i_0\left\{\frac{C_o(0,t)}{C_o(\infty,t)}\exp(-\alpha zF\eta/RT) - \frac{C_R(0,t)}{C_R(\infty,t)}\exp(1-\alpha)\, zF\eta/RT\right\} \tag{23}$$

This equation provides a more realistic description when electrode reactions are limited by both mass transport and charge transfer. Specifically, the concentration ratio terms explicitly represent mass transport effects. The Nernst-Planck equation unifies these transport phenomena:

$$J = -D\nabla C - (nFD/RT)C\nabla\varphi + Cv \tag{24}$$

where ∇C is the concentration gradient, $\nabla\varphi$ is the potential gradient, and v is the fluid

velocity vector. Each term represents contributions from diffusion, migration, and convection, respectively.

Under mass transport-limited conditions, the limiting current density is observed as expressed in Eq. (12). Importantly, the diffusion layer thickness δ strongly depends on the system's hydrodynamic conditions. Mass transport characteristics can be optimized through control of convection conditions.

1.4.5 Relationship between mass transfer phenomena and deposition reaction

The relationship between mass transfer phenomena and metal electrodeposition has been recognized as a critical factor in understanding and controlling deposition morphology.[34] Recent studies have highlighted several important aspects of this relationship that influence the practical performance of rechargeable batteries.

One fundamental concept is the effect of local mass transport conditions on deposition uniformity. Mass transport kinetics, particularly near the electrode surface, plays a decisive role in determining whether deposited metal forms uniform or dendritic structures.[35] The mass transport rate is closely related to the applied current density, and there exists a critical threshold above which non-uniform deposition becomes dominant.[36] This threshold is fundamentally connected to the diffusion limitation of metal ions in the electrolyte.

The electrolyte composition and concentration significantly influence mass transport behavior[37]. Recent investigations have shown that the electrolyte design can alter both the ion transport mechanisms and deposition patterns.[34] For instance, higher electrolyte concentrations can modify the ion transport properties, though this may come at the cost of increased viscosity which affects overall mass transport rates.[36]

Local concentration gradients near the electrode surface have emerged as a key factor linking mass transport to deposition morphology.[35] When severe concentration gradients develop due to mass transport limitations, the deposition pattern tends to shift from relatively uniform growth to dendritic formation.[36] This transition is accompanied by changes in the local electric field distribution and current density patterns. Temperature effects on mass transport-deposition relationships have also been identified as significant.[38] Elevated temperatures enhance ion mobility and diffusion rates, which can promote more uniform deposition patterns. However, temperature effects must be carefully balanced against potential adverse reactions at the electrode-electrolyte interface.

The formation and properties of the SEI layer introduce additional complexity to the mass transport-deposition relationship. The SEI layer characteristics influence local ion transport pathways and can affect the uniformity of metal deposition.[35] Understanding this interplay is essential for developing strategies to control deposition morphology.

Moving forward, achieving precise control over metal deposition requires comprehensive consideration of these mass transport effects. This includes optimizing electrolyte properties, controlling local concentration gradients, and managing interface phenomena. Future research directions may focus on developing novel approaches to regulate mass transport behavior for improved deposition control. This additional understanding of mass transport-deposition relationships provides valuable insights for the development of next-generation energy storage devices, particularly those utilizing metal anodes. The challenge lies in translating these fundamental insights into practical strategies for controlling metal deposition in real battery systems.

1.5 Measurement of the metal ion concentration

1.5.1 Conventional measurement methods

Table 3. Metal ion transport measurement techniques.

TECHNIQUE	PRINCIPLE	FEATURES
SCANNING ELECTROCHEMICAL MICROSCOPY	Electrochemical detection using microelectrode probe	High spatial resolution Direct measurement of reactions
RAMAN SPECTROSCOPY	Light scattering analysis of molecular vibrations	Chemical specificity
REFRACTIVE INDEX MEASUREMENT	Light refraction based on ion concentration	Non-contact Real-time analysis
NIMERICAL SIMULATION	Mathematical modeling	Predictive capability Cost-effective

Understanding metal ion transport phenomena near electrodes is crucial for elucidating the nature of electrochemical reactions. Table. 3 shows the various metal ion transport measurement techniques. There have been a variety of measurement techniques developed, each with distinct characteristics and limitations.

Scanning Electrochemical Microscopy (SECM) detects local electrochemical reactions using a microelectrode probe.[39] Ion concentration spatial distribution can be measured by scanning the probe while applying a specific potential difference between electrodes. However, the physical presence of the probe inherently interferes with ion movement, compromising measurement accuracy.

Raman spectroscopy is a non-contact measurement method utilizing Raman scattering phenomena for material identification.[40] It is suitable for electrolyte solutions

and enables analysis with minimal sample volumes. However, high-energy incident light can damage samples.

Refractive index measurement calculates ion concentration from laser light refraction angles based on Snell's law.[41] This method exploits the dependence of electrolyte refractive index on ion concentration. While enabling non-contact measurement, it has limited spatial resolution.

In addition to these experimental approaches, theoretical analysis through numerical simulation,[42] plays an important role in interpreting and predicting experimental results.

1.5.2 Laser interference microscopy measurements

Laser interference microscopy is a non-destructive measurement technique utilizing light interference phenomena.[43–45] Using low-energy lasers minimizes sample impact while enabling in-situ observation of concentration distributions with high temporal resolution (0.1 seconds). The underlying holographic technology was proposed by Dennis Gabor in 1948.[46] Unlike conventional optical microscopes that detect only light amplitude, laser interference microscopes can acquire phase information. This technique was established in electrochemistry by McLarnon and Muller in the 1970s. [47,48] Subsequently, Fukunaka et al.[49] applied it to aqueous solutions, while Nishikawa et al.[50] and Miki et al.[51] extended its application to non-aqueous electrolytes.

Three main optical systems are used for interference measurements in electrochemistry.

Fizeau interferometers have the most basic configuration, interfering reflected light from the front and back surfaces of samples.[52] While their simple optical system is

easy to adjust and relatively stable against vibration, they are susceptible to multiple reflections from samples and limited by sample thickness.

Mach-Zehnder interferometers achieve high measurement accuracy and wide measurement range by completely separating reference and sample light paths.[53] They enable quantitative phase difference measurements without sample thickness limitations but require precise optical path adjustment and are sensitive to environmental changes and vibration.

Michelson interferometers enable highly sensitive measurements through folded structures that effectively utilize optical path length.[54] While compact and relatively easy to adjust, they are sensitive to polarization effects and have certain sample shape restrictions. Their vibration stability characteristics fall between those of Fizeau and Mach-Zehnder interferometers.

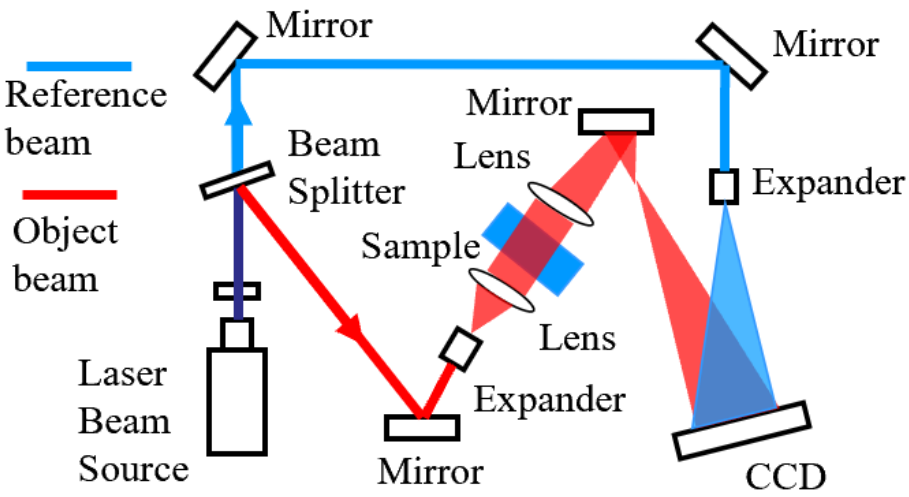

Figure 4. Schematic of interferometry. Reproduced with permissions from [55].

We employed a holographic interference microscope based on a Mach-Zehnder interferometer design. Figure 4 illustrates the measurement principle of the interference

method. The laser beam is split into reference and object beams. While the reference beam maintains constant phase, the object beam undergoes phase changes upon passing through the sample. By superimposing these beams on a screen, interference fringes are formed. From these fringes, phase difference information can be extracted to quantify ion concentration distributions near the electrode.

1.6 Concept and purpose of this study

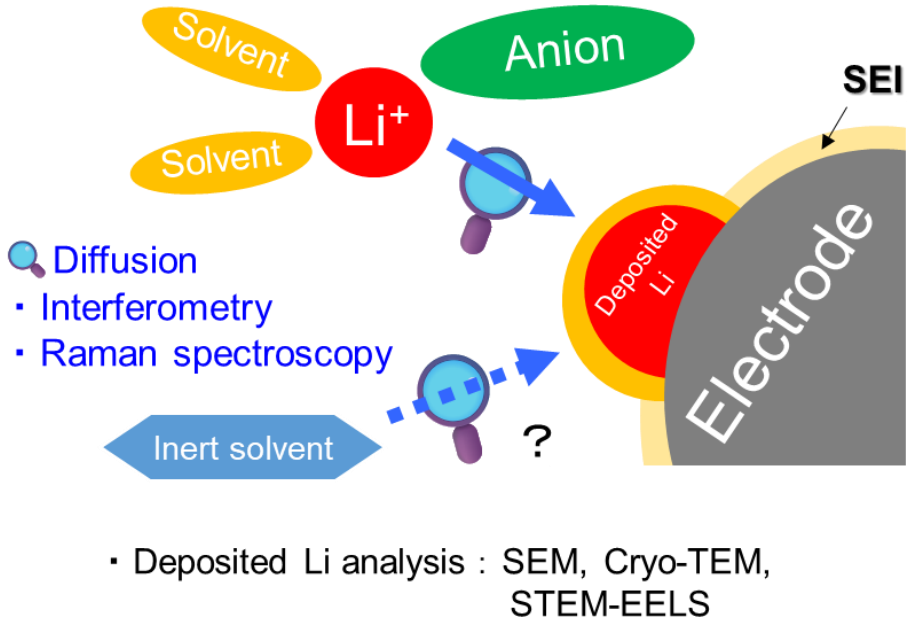

Figure 5. Schematic of this study.

This research aims to elucidate lithium metal electrodeposition phenomena from a multi-scale perspective, spanning from ion transport to crystal growth. As shown in Figure 5, we focus particularly on diffusion phenomena and ion coordination structures, systematically investigating their influences on dendrite growth and SEI formation.

The nucleation process in metal electrodeposition proceeds through several sequential elementary steps. It begins with metal ion diffusion in solution, followed by electron transfer reactions at the electrode surface and surface diffusion of adsorbed atoms. This process continues through nucleation at step and kink sites, ultimately leading to crystal growth and dendrite formation. To comprehensively understand these interconnected electrodeposition phenomena, we have designed an experimental plan utilizing multiple complementary-advanced analytical technique.

For observing Li^+ diffusion behavior in electrolytes, we implement in-situ laser interference microscopy. This technique enables non-destructive concentration distribution measurements with high temporal resolution. Additionally, we analyze Li^+ concentration changes and coordination states near the electrode surface using Raman spectroscopy. This application of Raman spectroscopy allows us to track local chemical environment changes accompanying electrochemical reactions on the surface of electrodes.

For lithium electrodeposition processes on electrode surfaces, we conduct real-time observations using optical microscopy. Furthermore, we apply electron microscopy techniques hierarchically for detailed deposit structure analysis. This multi-faceted structural evaluation combines surface morphology observations by scanning electron microscopy (SEM), atomic-level structural analysis by transmission electron microscopy (TEM), and local composition analysis by scanning transmission electron microscopy (STEM). For SEI layers formed on deposit surfaces, we perform chemical state analysis using electron energy loss spectroscopy (EELS).

Through integrated analysis of insights obtained from these multiple analytical approaches, we aim to achieve fundamental understanding of lithium electrodeposition mechanisms. Particular emphasis is placed on examining the influence of diffusion phenomena on dendrite growth and the role of solvation structures in SEI formation processes. This systematic approach is expected to yield fundamental insights contributing to the development of next-generation secondary batteries.

Chapter 2 investigates mass transport phenomena during lithium deposition and dissolution in highly concentrated electrolytes. The findings demonstrate that deposition morphology is strongly dependent on current density, with SEI film formation at the

electrode surface playing a crucial role in morphology control. Detailed analysis of concentration variations near the electrode and their correlation with deposition morphology revealed that local concentration gradients promote dendrite growth. Additionally, at high current densities, dissolution reactions were found to cause potential divergence due to supersaturation at the electrode surface.

Chapter 3 examines the formation and relaxation processes of concentration gradients in solvate ionic liquids composed of lithium salts and tetraglyme. The research revealed asymmetric diffusion coefficients between anodic and cathodic regions, leading to asymmetric concentration distributions. This asymmetry was demonstrated to originate from electrolyte viscosity variations.

Chapter 4 analyzes mass transport phenomena during current reversal. The concentration profiles obtained through interferometry were validated through finite difference method simulations. Raman spectroscopy investigations elucidated the correlation between lithium ion solvation structures and transport numbers. The study discovered that distinctive concentration distributions form near the electrode during current reversal, significantly influencing deposition morphology.

Chapter 5 investigates the correlation between electrolyte concentration and lithium deposition morphology. Optical microscopy observations revealed that the salt-to-solvent molar ratio substantially influences deposition layer thickness. Low concentrations were found to result in thickening of the deposition layer through repeated reactions, while high concentrations led to thinning. Furthermore, based on detailed structural analysis of deposits, three concentration-dependent growth models were proposed.

Chapter 6 examines the effects of dilution with low-permittivity solvents on mass

transport and lithium electrodeposition in highly concentrated electrolytes. The apparent diffusion coefficients of lithium ions were quantitatively compared between highly concentrated and locally concentrated electrolytes, demonstrating enhanced diffusivity through dilution. The study revealed that reduced electrolyte viscosity through dilution suppresses side reactions at deposit surfaces, enabling more uniform deposition morphology.

Chapter 7 presents a comprehensive summary of the research findings.

References

[1] O. no Yasumaro, *Kojiki*, Enigma Edizioni, **2023**.

[2] N. L. Panwar, S. C. Kaushik, S. Kothari, *Renewable and sustainable energy reviews* **2011**, *15*, 1513–1524.

[3] A. Qazi, F. Hussain, N. A. Rahim, G. Hardaker, D. Alghazzawi, K. Shaban, K. Haruna, *IEEE access* **2019**, *7*, 63837–63851.

[4] A. Yoshino, *Angew Chem Int Ed* **2012**, *51*, 5798–5800.

[5] F. Wu, J. Maier, Y. Yu, *Chemical Society Reviews* **2020**, *49*, 1569–1614.

[6] R. Wang, W. Cui, F. Chu, F. Wu, *Journal of Energy Chemistry* **2020**, *48*, 145–159.

[7] Y. Zhang, T.-T. Zuo, J. Popovic, K. Lim, Y.-X. Yin, J. Maier, Y.-G. Guo, *Materials Today* **2020**, *33*, 56–74.

[8] Q. Wang, B. Liu, Y. Shen, J. Wu, Z. Zhao, C. Zhong, W. Hu, *Advanced Science* **2021**, *8*, 2101111.

[9] T. Kennedy, M. Brandon, F. Laffir, K. M. Ryan, *Journal of Power Sources* **2017**, *359*, 601–610.

[10] W. Liu, P. Liu, D. Mitlin, *Advanced Energy Materials* **2020**, *10*, 2002297.

[11] Z. Liu, X. Yuan, S. Zhang, J. Wang, Q. Huang, N. Yu, Y. Zhu, L. Fu, F. Wang, Y. Chen, *NPG Asia Materials* **2019**, *11*, 12.

[12] C. Fang, B. Lu, G. Pawar, M. Zhang, D. Cheng, S. Chen, M. Ceja, J.-M. Doux, H. Musrock, M. Cai, *Nature Energy* **2021**, *6*, 987–994.

[13] H. Yang, E. O. Fey, B. D. Trimm, N. Dimitrov, M. S. Whittingham, *Journal of Power Sources* **2014**, *272*, 900–908.

[14] Q. Wang, L. Jiang, Y. Yu, J. Sun, *Nano Energy* **2019**, *55*, 93–114.

[15] Y. Yamada, J. Wang, S. Ko, E. Watanabe, A. Yamada, *Nature Energy* **2019**, *4*, 269–

280.

[16] E. R. Logan, J. R. Dahn, *Trends in Chemistry* **2020**, *2*, 354–366.

[17] J. Kalhoff, G. G. Eshetu, D. Bresser, S. Passerini, *ChemSusChem* **2015**, *8*, 2154–2175.

[18] Y. Yamada, K. Furukawa, K. Sodeyama, K. Kikuchi, M. Yaegashi, Y. Tateyama, A. Yamada, *Journal of the American Chemical Society* **2014**, *136*, 5039–5046.

[19] K. Sodeyama, Y. Yamada, K. Aikawa, A. Yamada, Y. Tateyama, *The Journal of Physical Chemistry C* **2014**, *118*, 14091–14097.

[20] L. Chen, X. Fan, E. Hu, X. Ji, J. Chen, S. Hou, T. Deng, J. Li, D. Su, X. Yang, *Chem* **2019**, *5*, 896–912.

[21] S. Ko, Y. Yamada, A. Yamada, *Batteries & Supercaps* **2020**, *3*, 910–916.

[22] S. Ko, Y. Yamada, A. Yamada, *Joule* **2021**, *5*, 998–1009.

[23] X. Cao, H. Jia, W. Xu, J.-G. Zhang, *Journal of The Electrochemical Society* **2021**, *168*, 010522.

[24] A. Manthiram, S. Chung, C. Zu, *Advanced Materials* **2015**, *27*, 1980–2006.

[25] G. Zhou, H. Chen, Y. Cui, *Nature Energy* **2022**, *7*, 312–319.

[26] Z. Wan, D. Lei, W. Yang, C. Liu, K. Shi, X. Hao, L. Shen, W. Lv, B. Li, Q. Yang, F. Kang, Y. He, *Adv Funct Materials* **2019**, *29*, 1805301.

[27] J. Wu, S. Liu, F. Han, X. Yao, C. Wang, *Advanced Materials* **2021**, *33*, 2000751.

[28] G. Girishkumar, B. McCloskey, A. C. Luntz, S. Swanson, W. Wilcke, *J. Phys. Chem. Lett.* **2010**, *1*, 2193–2203.

[29] J. Newman, K. E. Thomas-Alyea, *Electrochemical Systems*, John Wiley & Sons, **2012**.

[30] K. B. Prater, A. J. Bard, *Journal of the Electrochemical Society* **1970**, *117*, 207.

[31] A. Fick, *The London, Edinburgh, and Dublin Philosophical Magazine and Journal of Science* **1855**, *10*, 30–39.

[32] J. Evans, C. A. Vincent, P. G. Bruce, *Polymer* **1987**, *28*, 2324–2328.

[33] A. J. Bard, L. R. Faulkner, H. S. White, *Electrochemical Methods: Fundamentals and Applications*, John Wiley & Sons, **2022**.

[34] K. Nishikawa, T. Mori, T. Nishida, Y. Fukunaka, M. Rosso, *Journal of Electroanalytical Chemistry* **2011**, *661*, 84–89.

[35] X. Xu, X. Jiao, O. O. Kapitanova, J. Wang, V. S. Volkov, Y. Liu, S. Xiong, *Advanced Energy Materials* **2022**, *12*, 2200244.

[36] P. Bai, J. Li, F. R. Brushett, M. Z. Bazant, *Energy Environ. Sci.* **2016**, *9*, 3221–3229.

[37] Y. Liu, X. Xu, M. Sadd, O. O. Kapitanova, V. A. Krivchenko, J. Ban, J. Wang, X. Jiao, Z. Song, J. Song, S. Xiong, A. Matic, *Advanced Science* **2021**, *8*, 2003301.

[38] G. Li, *Advanced Energy Materials* **2021**, *11*, 2002891.

[39] P. Bertoncello, *Energy & Environmental Science* **2010**, *3*, 1620–1633.

[40] L. F. Olbrich, B. Jagger, J. Ihli, M. Pasta, *ACS Energy Lett.* **2024**, *9*, 3636–3642.

[41] R. J. Schechter, *Survey of Ophthalmology* **1977**, *21*, 464–466.

[42] S. Kawai, K. Nishikawa, Y. Fukunaka, S. Kida, *Electrochemistry* **2009**, *77*, 601–603.

[43] Y. Konishi, Y. Nakamura, Y. Fukunaka, K. Tsukada, K. Hanasaki, *Electrochimica acta* **2003**, *48*, 2615–2624.

[44] B. Yuan, J. Zhang, G. Gao, L. Li, C. Wang, *Electrochemistry communications* **2013**, *27*, 116–119.

[45] Y. Hu, X. Li, Z. Jiao, G. Gao, B. Yuan, L. Li, C. Wang, *Electrochemistry* **2016**, *84*, 378–382.

[46] D. Gabor, *Science* **1972**, *177*, 299–313.

[47] F. R. McLarnon, R. H. Muller, C. W. Tobias, *JOSA* **1975**, *65*, 1011–1018.

[48] F. R. McLarnon, R. H. Muller, C. W. Tobias, *Electrochimica Acta* **1976**, *21*, 101–105.

[49] Y. Fukunaka, T. Yamamoto, Y. Kondo, *Journal of the Electrochemical Society* **1989**, *136*, 3630.

[50] K. Nishikawa, T. Mori, T. Nishida, Y. Fukunaka, M. Rosso, *Journal of electroanalytical chemistry* **2011**, *661*, 84–89.

[51] A. Miki, K. Nishikawa, G. Kamesui, H. Matsushima, M. Ueda, M. Rosso, *Journal of Materials Chemistry A* **2021**, *9*, 14700–14709.

[52] H. S. White, D. J. Earl, J. D. Norton, H. J. Kragt, *Anal. Chem.* **1990**, *62*, 1130–1134.

[53] K. Kim, T. E. Murphy, *Optics express* **2013**, *21*, 19488–19497.

[54] D. Mayorga-Cruz, P. A. Márquez-Aguilar, O. Sarmiento-Martinez, J. Uruchurtu-Chavarín, *Optics and lasers in engineering* **2007**, *45*, 140–144.

[55] A. Miki, K. Nishikawa, T. Ozawa, H. Matsushima, M. Ueda, *Journal of The Electrochemical Society* **2020**, *167*, 062501.

Chapter 2: Mass Transfer During Electrodeposition and Dissolution of Li Metal within Highly Concentrated Electrolytes

2.1 Introduction

Metallic Li is an ideal anode material for rechargeable batteries because it exhibits the lowest standard electrode potential (–3.04 V vs. the standard hydrogen electrode) and density (0.534 g cm^{-3}), as well as large capacity (3860 mA h g^{-1}). Therefore, recent studies have been focused on using metallic Li as an anode to increase energy density.[1–3] However, Li easily forms dendrites upon charging (electrodeposition), which poses significant problems regarding degradation and safety. For the stable operation of Li metal electrodes, maintaining the uniformity of the electrode surface morphology is critical. Numerous studies have been conducted on the correlation between the electrode surface morphology and solid electrolyte interphase (SEI) layer composition using X-ray photoelectron spectroscopy, scanning electron microscopy (SEM), and transmission electron microscopy (TEM).[4–6] However, only a few studies have involved analyses of the morphology of Li deposits with respect to the ionic mass transfer close to the electrode.[7–9] Generally, metal electrodeposition is considerably influenced by ionic mass transfer within the electrolyte.[10–12] As the electrochemical reaction is initiated, a concentration gradient forms close to the electrode, and the diffusion of ionic species is enhanced. Uniform deposition morphology can be obtained with sufficient mass transfer of metal cations to the electrode surface. Conversely, if the ionic are depleted at the electrode surface, nonuniform deposits like dendrites and products of other unexpected side reactions, such as the decomposition of solvents and anions, including the chemical reaction between deposited Li metal and solvents and anions, may be induced.[5,13] The Sand's time is sometimes utilized to discuss the ionic mass transfer in the electrodeposition system. Therefore, elucidating the relationship between the ionic mass

transfer and morphological variation in Li metal is essential to understand the dendrite formation mechanism of Li metal.

Recently, highly concentrated electrolytes (HCEs) have attracted attention for use in next-generation batteries.[14,15] The interactions between Li^+, anions, and solvent molecules within HCEs differ significantly from those within conventional electrolytes with concentrations of 1.0–1.2 M used in Li-ion batteries.[16,17] Increasing the electrolyte concentration increases the interaction between the solvent molecules and Li^+. This typical coordination state provides high decomposition durability (less decomposition) and low vapor pressure. These features lead to a high coulombic efficiency for the charging and discharging of Li metal, and 5 V HCEs have been proposed.[18–20] The ionic mass transfer during the electrochemical reaction within an HCE is critical in analyzing the morphological variation in the Li metal electrode. Wang et al. and Mistry et al. reported in situ measurements of the concentration profiles obtained using nuclear magnetic resonance imaging (MRI)[21,22] and proposed a theoretical approach to analyze the mass transfer within an HCE based on Onsager–Stefan–Maxwell theory. However, they did not mention the relationship between the surface morphology of the electrodeposited Li metal and mass transfer. Our group reported the development of concentration profiles close to the electrodes within an equimolar lithium bis(trifluoromethanesulfonyl)amide (LiTFSA)-tetraglyme electrolyte by laser holographic interferometry.[9] McLarnon and Muller applied this technique in the 1970s to analyze the ionic mass transfer accompanied with the electrodeposition of Cu in aqueous solution. The authors used an interferometer to observe the concentration change of the electrolyte with respect to changes in the refractive index. The concentration profile in the electrolyte was then determined from the obtained interference fringes. This

technique has been very instrumental thus far.[23–28] MRI techniques only measure magnetically active elements, whereas interferometry reveals refractive index changes. In general, the refractive indices of electrolyte solutions change with the concentration; thus, almost all electrolytes can be studied by interferometry. In this study, we investigated the transient concentration profile and solution structure close to the electrode during Li electrodeposition and dissolution in a 1:2 LiTFSA:sulfolane (SL) HCE by in situ laser holographic interferometry and Raman spectroscopy.[29] The correlations between the mass transfer parameters, such as electrode surface concentration and electrodeposition morphology, were measured by in situ digital microscopy[13] and ex-situ SEM, TEM, and scanning TEM (STEM)-electron energy-loss spectroscopy (EELS).[30,31] Furthermore, the Li electrochemical dissolution (the discharge reaction of the Li anode) was measured, and specific features of the HCE were verified.

2.2 Experimental

The electrochemical cell was configured as described in a previous study.[1] When observing the cathode side, a Cu plate (99.99%, Nilaco, Tokyo, Japan) was used as the cathode and a Li plate (99.9%, Honjo Metal, Osaka, Japan) was used as the anode. When observing the anode side, an electrochemical cell with Li metal plates as the anode and cathode was used. The electrode thickness was 0.20 mm. When a Li plate was used as an electrode, the electrochemical cell was assembled by contacting a Cu current collector (5 μm) to the Li plate. The Cu electrode was polished with emery paper step-by-step (#800 → #1200 → #3000). The oxide film on the electrode surface was then removed using 0.10 M aqueous HNO_3. The electrodes were subsequently washed with acetone, ethanol, and distilled water. Finally, the upper and lower parts of the Cu plate were coated with silicone (FC-112 RTV, Fine Chemical Japan, Tokyo, Japan) for insulation. The electrochemical reaction could occur only on the cross-section of the Cu plate. The cathode and anode were facing parallel to each other, and a quasi-2D cell arrangement was adopted to minimize the effects of natural convection. The reaction areas of both electrodes were 0.20 mm (vertical) × 15 mm (horizontal). For the anodic and cathodic potential measurements, Li was used as the pseudo reference electrode; it was inserted between both the electrodes, as shown in Fig. S3c, and the potential was measured.

The electrolyte was prepared by mixing LiTFSA (99.9%, Kishida Chemical, Osaka, Japan) and SL (99.9%, Kishida Chemical) in a molar ratio of 1:2, and this mixture was placed on a hot plate (50 °C) overnight to ensure complete dissolution. Electrochemical studies were conducted at constant current densities (1.0, 2.5, or 5.0 mA cm^{-2}) using a potentiostat (SP-150, Bio-Logic Science Instruments, Seyssinet-Pariset, France). The electrochemical cell and electrolyte were prepared in a dry room

with a dew point of –50 °C or lower. The refractive index of the electrolyte was measured using a digital refractometer (RX-7000α, ATAGO, Tokyo, Japan), and the viscosity and density were measured using a falling ball viscometer (Lovis 2000 ME, Anton Paar, Graz, Austria). All measurements were conducted in a dry room at room temperature.

The electrodeposited Li was observed using SEM (JSM-7800F, JEOL, Tokyo, Japan) and TEM (JEM-ARM200F, JEOL). After disassembling the electrochemical cell, the electrodes were carefully rinsed with 1,2-dimethoxyethane (Kishida Chemical) and transferred to the SEM or TEM using an air-tight holder. The SEI layer on the electrodeposited Li surface was analyzed using STEM-EELS. The TEM and STEM-EELS were performed at –170 °C using a double tilt LN2 Atmos Defend Holder (Mel-Build, Fukuoka, Japan).

Digital holographic interferometry (DHM T1000, Lyncée Tec, Lausanne, Switzerland) was used to measure the concentration profile of the electrolyte during Li electrodeposition or electrochemical dissolution. The wavelength of the laser beam was 683.6 nm and the optical path length was 0.20 mm, which was the thickness of the electrochemical cell. The obtained hologram was analyzed using Koala software (Lyncée Tec), and the concentration profile was acquired from the concentration dependence of the refractive index. The refractive index is proportional to the concentration (Eq. S1):

$$\Delta n = \left(\frac{\partial n}{\partial C}\right) \Delta C \tag{S1}$$

The interference equation (Eq. S2) is as follows:

$$d\Delta n = \left(\frac{\Delta\theta}{2\pi}\right)\lambda \quad \text{(S2)}$$

where Δn represents the change in refractive index, ΔC is the change in Li^+ concentration, d is the optical path length, $\Delta\theta$ is the phase change, and λ is the wavelength of the laser beam. The concentration profile of Li^+ can be obtained using Eq. S3, which can be derived from Eqs. S1 and S2 as follows:

$$\Delta C = \left(\frac{\partial C}{\partial n}\right)\left(\frac{\Delta\theta}{2\pi}\right)\frac{\lambda}{d} \quad \text{(S3)}$$

A digital microscope (VHX-1000, Keyence, Osaka, Japan) was used to observe the dendrite growth of electrodeposited Li on the Cu cathode surface. The microscope image was divided into four equal parts, and the longest dendrite length in each region was measured. Their average values were then plotted, with the standard deviations shown as error bars. The concentration profile close to the cathode was calculated at the distance corresponding to the tip of the average dendrite length (plot).

The Raman spectra of the electrolytes were measured in a dry room using a laser micro-Raman spectrometer (LabRAM 1B, HORIBA, Kyoto, Japan). Prior to measurement, the spectrometer was calibrated using a Si single crystal. The wavelength of the excitation laser was 632.7 nm, and the resolution of the spectrometer was ~1 cm^{-1}. The exposure time and cumulative frequency were 15 s and 4 times (reference data); and 5 s and 5 times (in situ measurement), respectively. The interference studies and Raman spectroscopy were performed at room temperature. The obtained Raman spectra were

analyzed using GRAMS-AI software (Thermo Fisher Scientific, Waltham, MA, USA). The Gaussian–Lorentz function was employed for peak separation.

2.3 Results and Discussion

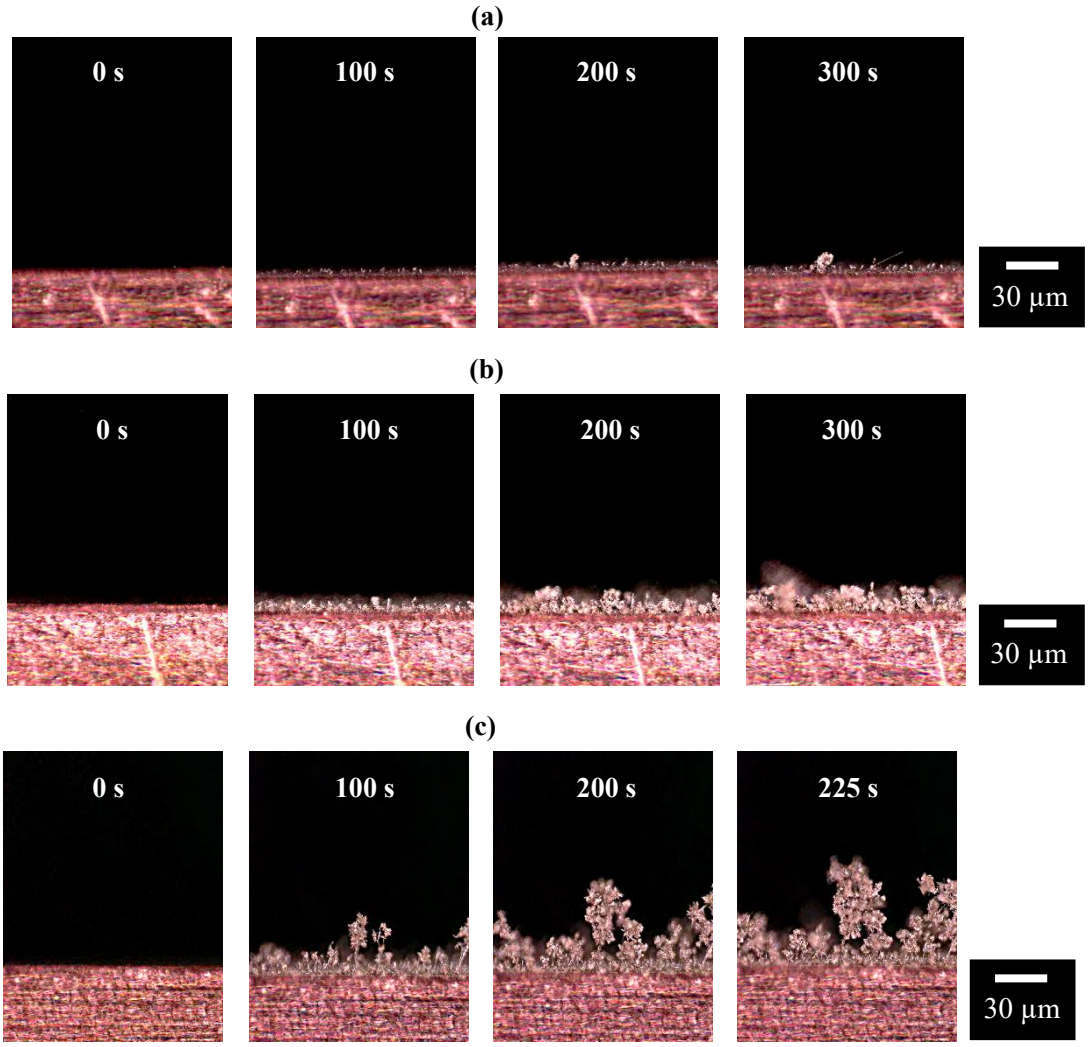

Figure 1. In-situ digital microscopy observations of Li electrodeposition at current densities of (a) 1.0, (b) 2.5 and (c) 5.0 mA cm^{-2}.

Figure 1(a)-1(c) show the snapshots of in-situ digital microscopy observations of Li electrodeposition at current densities of 1.0, 2.5, and 5.0 mA cm^{-2}, respectively. The observation region was divided into four equal parts, and the maximum length of the electrodeposited Li in each region and its standard deviation are shown in Figure 2(a).[13] Li deposition is not observed for the first few seconds after the onset of electrolysis, potentially due to the reduction of the oxide film formed on the Cu cathode surface and

some side reactions like decomposition of solvents. In addition, the nucleation of electrodeposited Li should have been initiated but was extremely small for observation using an optical microscope. As electrodeposition proceeds, the deposited Li metal forms dendrites that grow. The larger the current density, the longer the dendrites that simultaneously form. This finding is consistent with a larger current density increasing the amount of electricity used for electrodeposition. Assuming that the electrodeposited Li metal was perfectly dense, the thickness was calculated to be 0.4, 1.0, and 2.0 μm at 1.0, 2.5, and 5.0 mA cm^{-2} for 300 s, respectively. The large discrepancies between the theoretically calculated and measured values are due to dendritic, nonuniform Li deposition. Moreover, the SEM images show that the cathode surface is covered with numerous whisker-like Li dendrites (Figures S1(a)–S1(f)). These Li dendrites combine with the surrounding dendrites to form more complex morphologies, resulting in longer, larger, irregularly shaped deposits.[32,33] Remarkably, needle-shaped Li dendrites are also formed at a current density of 5.0 mA cm^{-2}. The same applied electricity shows similar length of Li dendrites, but growth rate behavior is more drastically in higher current density. The morphology of the electrodeposited Li metal is strongly affected by the applied current density within the electrolyte.

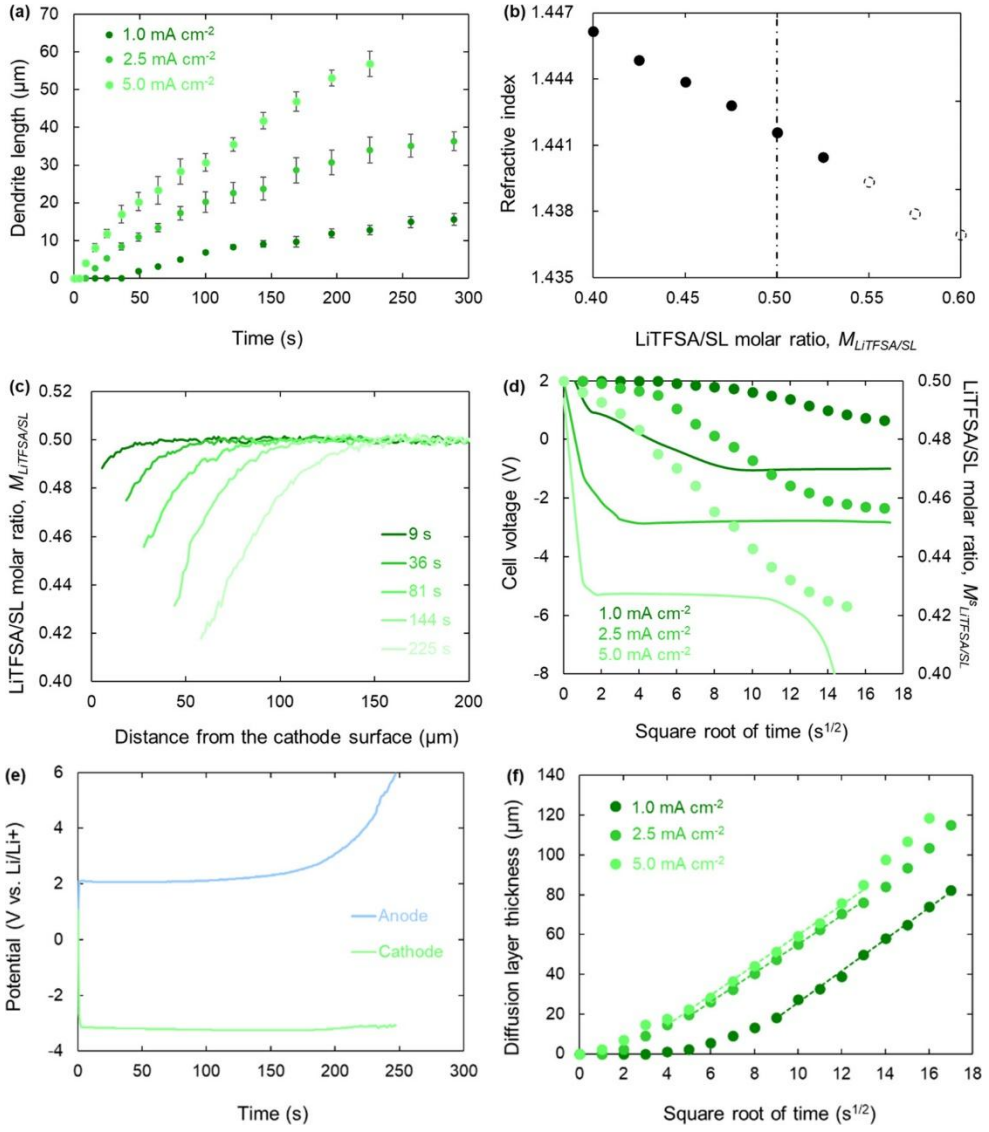

Figure 2. Dendrite growth and development of LiTFSA concentration profile during the electrodeposition in HCEs. (a) Variation in Li dendrite length with time. (b) Refractive indices of electrolytes containing LiTFSA and SL in different ratio. (c) Concentration profiles close to cathode during Li electrodeposition. (d) Change in the cell voltage (lines) and LiTFSA/SL molar ratios at the cathode surface (plots) with respect to the square root of time. (e) Variation of the Cu cathode and Li anode potential vs. Li foil reference electrode with time. (f) Diffusion layer thickness close to the cathode with respect to the square root of time.

Figure 2(b) shows the concentration dependence of the refractive index of the LiTFSA-SL electrolyte, with the refractive index decreasing with increasing the molar ratio of LiTFSA/SL, $M_{LiTFSA/SL}$. The slope of the approximate straight line, $\partial n/\partial C$, varies slightly at $M_{LiTFSA/SL}$ = 0.50 (1 : 2): it is –0.0448 and –0.0474 at $M_{LiTFSA/SL}$ values of 0.40–0.50 and 0.50–0.60, respectively. The concentration profile close to the electrode during Li electrodeposition was calculated using these values and Eq. S3.

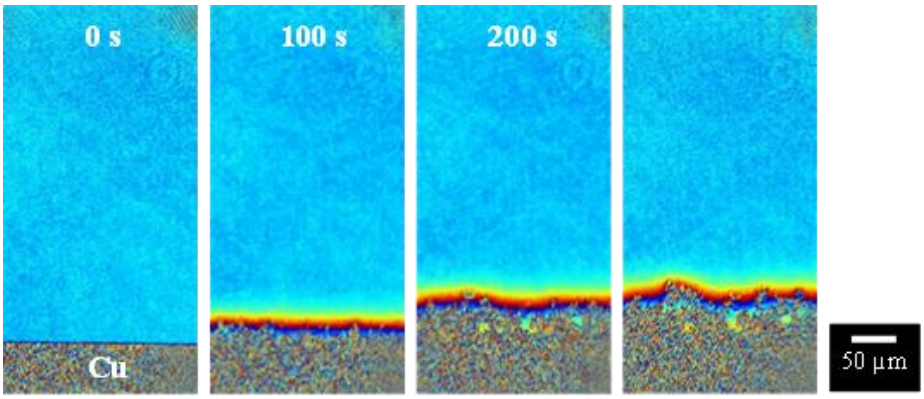

Figure 3. Phase shift near the cathode during Li electrodeposition at 5.0 mA cm^{-2}.

Figure 3 shows the phase changes close to the electrode during electrodeposition at 5.0 mA cm^{-2}. The gray mosaic area on the left is the electrode, and the blue area on the right is the electrolyte. The color near the electrode changes after the electrochemical reaction commences. Here, the color changes indicate the optical phase changes of the electrolyte that correspond to changes in $M_{LiTFSA/SL}$.[9] The interferometry images also reveal the dendrite growth of the electrodeposited Li metal.

Figure 2(c) shows the variations with time of the concentration profiles close to the electrode during electrodeposition. As electrodeposition proceeds, $M_{LiTFSA/SL}$ close to the cathode decreases, whereas the surface of the electrode migrates toward the bulk electrolyte, owing to the accumulation of the electrodeposited Li. The growth of diffusion layers is observed, and after 225 s, the diffusion layer thickness, δ, reaches 110 μm. Here, δ is the distance from the electrode surface to the concentration boundary, which is where a 1% change in phase difference between the bulk and electrode surface occurs.[28] Notably, as shown in Figure 3, the diffusion layer of the cathode grows nonuniformly, with a shape corresponding to the contours of the dendrites.

Figure 2(d) depicts the changes in the cell voltage and cathode surface concentrations as a function of the square root of the electrodeposition time, $t^{1/2}$. It is worth noting that the cathode surface concentration refers to the surface concentration at the deposit surface, which is composed of many clustered dendrites, and not to that at the tip of a single growing dendrite. The cell voltage is positive for several seconds after the current is applied at 1.0 or 2.5 mA cm^{-2}. The applied current may be consumed in the reduction of the oxide film and decomposition of electrolyte on the Cu cathode surface, not in the electrodeposition of Li metal. When the voltage is negative, the electrode surface concentration, $M^s_{LiTFSA/SL}$, begins to change at all current densities. As the voltage plateaus, the $M^s_{LiTFSA/SL}$ values begin to change in proportion to $t^{1/2}$. Eq. 1 is satisfied, expressing the relationship between the molar concentration of LiTFSA at the electrode surface, C^s, and t:

$$C^s = C^0 + \frac{2i(1-t^*)}{zF\sqrt{D\pi}}\sqrt{t} \quad (1)$$

where C^0 is the bulk concentration (mol L^{-1}), i is the current density (mA cm^{-2}), t^* is the transport number of cations, z is the valence number, F is the Faraday constant, and D is the diffusion coefficient (cm^2 s^{-1}).

According to Eq. 1, C^s is proportional to $t^{1/2}$. However, the change in C^s becomes moderate after 169 s for 2.5 and 5.0 mA cm^{-2} as shown in Figure 2 (d). There are two possible reasons for this accommodation behavior with respect to the cathode side. The first is the effect of natural convection generated within the cell. As electrolysis proceeds, Li deposition causes a density difference between the bulk electrolyte and electrolyte close to the electrodes. Convection promotes the supply of Li^+. Another reason may be an increase in the electrode surface area owing to the progress of dendrite growth. The increase in the electrode area decreases the applied current density per unit surface area, resulting in decreases in the electrodeposition reaction rate and, consequently, the progress of the electrodeposition reaction. A Li pseudo reference electrode was used to examine the potential changes of both electrodes. The schematic of the cell is shown in Figure S2. Figure 2(e) shows the potentials of the electrodes when the three electrodes cell was used. The anode potential increased at ~100 s. Previous studies using SL have suggested that the hopping mechanism enhances the mass transfer of Li^+.[34] Consequently, another research reported that the limiting current density in $LiBF_4$:SL = 1:2 electrolyte is higher than that in LiTFSA:G4 = 1:1 electrolyte by a factor of more than three (3.5 vs. 1.1 mA cm^{-2}).[35] For typical 1 mol L^{-1} concentration electrolytes, the

voltage overshoot is due to the concentration depletion at the cathode surface.[36] However, the depletion of LiTFSA on the cathode surface is suppressed at a scale of ~300 s because the electrolyte used in this experiment has a high concentration of ~3 mol L^{-1} and excellent mass transfer characteristics. Therefore, the divergence in voltage, observed in Figures 2(d) and 1(e), is attributed to the anode potential. Further, in this experiment, because the concentration of LiTFSA exceeds the solubility limit near the anode, the limiting current density is considered to be controlled by the mass transport on the anode side, as discussed in the latter of this research.

Figure 2(f) shows the changes in δ as a function of $t^{1/2}$ during electrodeposition. The growth of the diffusion layer on the cathode side is observed several seconds after the initiation of electrodeposition at 1.0 or 2.5 mA cm^{-2}. The time lag of diffusion layer formation is consistent with that of the cathode $M^s_{LiTFSA/SL}$. Once the diffusion layer formation commences, the δ values increase in proportion to $t^{1/2}$ at all current densities. The growth rates of δ accelerate at 169 s at 2.5 and 5.0 mA cm^{-2} due to the fluid motion of natural convection.

The apparent D was estimated from the growth rate of δ using the following equation derived from the Nernst–Planck equation and Fick's diffusion law:

$$D = \frac{\pi}{4} \times \left(\frac{\delta}{\sqrt{t}}\right)^2 \quad (2)$$

where $\delta/\sqrt{t}$ corresponds to the slopes of the plots in Figures 2(f). In calculating D, to minimize the influence of natural convection, the values at which δ increases in proportion to $t^{1/2}$ were used, D on the cathode side, $D_{cathode}$, is 4.1–4.6 × 10^{-7} cm^2 s^{-1}.

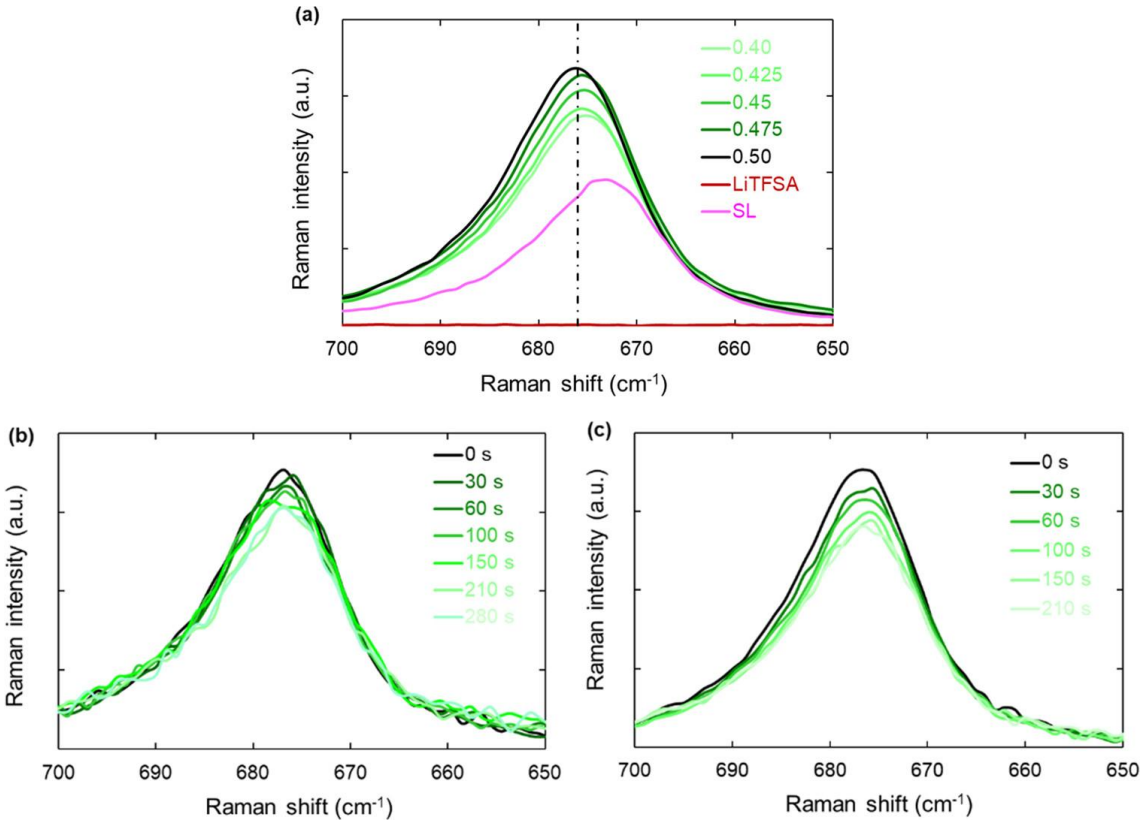

Figure 4. Raman spectra during the electrodeposition of Li metal. (a) Raman spectra in the range 650–700 cm^{-1} of the electrolytes containing LiTFSA and SL in different ratios. In situ Raman spectra in the range 650–700 cm^{-1} of the electrolyte close to the cathode at current densities of (b) 2.5 and (c) 5.0 mA cm^{-2} during Li electrodeposition.

The interferometry results demonstrate that the region near cathode surface change the molar ratio of LiTFSA and SL. The interaction between the LiTFSA and SL was investigated by Raman spectroscopy. Figure 4(a) shows the Raman spectra of various compositions of the electrolyte, LiTFSA powder, and SL in the range of 650–700 cm^{-1}. Xuan et al. observed C–S–C stretching of SL at 670–680 cm^{-1}, and as SL coordinates to metal ions, the peak intensity increases and the peak shifts toward higher

wavenumbers.[37] A peak at 676 cm^{-1} is observed when $M_{LiTFSA/SL}$ is 0.50, and as $M_{LiTFSA/SL}$ decreases from 0.50, the peak intensity decreases and the peak shifts toward a lower wavenumber. Therefore, as $M_{LiTFSA/SL}$ decreases, the free SL increases.

Figures 4(b) and 4(c) present the time-step Raman spectra of the electrolyte at approximately 10 μm from the cathode surface during Li electrodeposition at current densities of 2.5 and 5.0 mA cm^{-2}, respectively. As electrodeposition proceeds, the peak gradually shifts toward lower wavenumbers, and the peak intensity decreases because $M_{LiTFSA/SL}$ decreases close to the cathode. Li^+ ion is desolvated with SL molecules, and SL molecules are released to the electrolyte when the Li^+ ion is reduced to be Li on the electrode surface. The peak intensity decreases more at 5.0 mA cm^{-2} than at 2.5 mA cm^{-2} because of the increase in the free SL close to the cathode as the current density increases. This behavior is consistent with the results of interferometry measurement as shown in Figure 4(d).

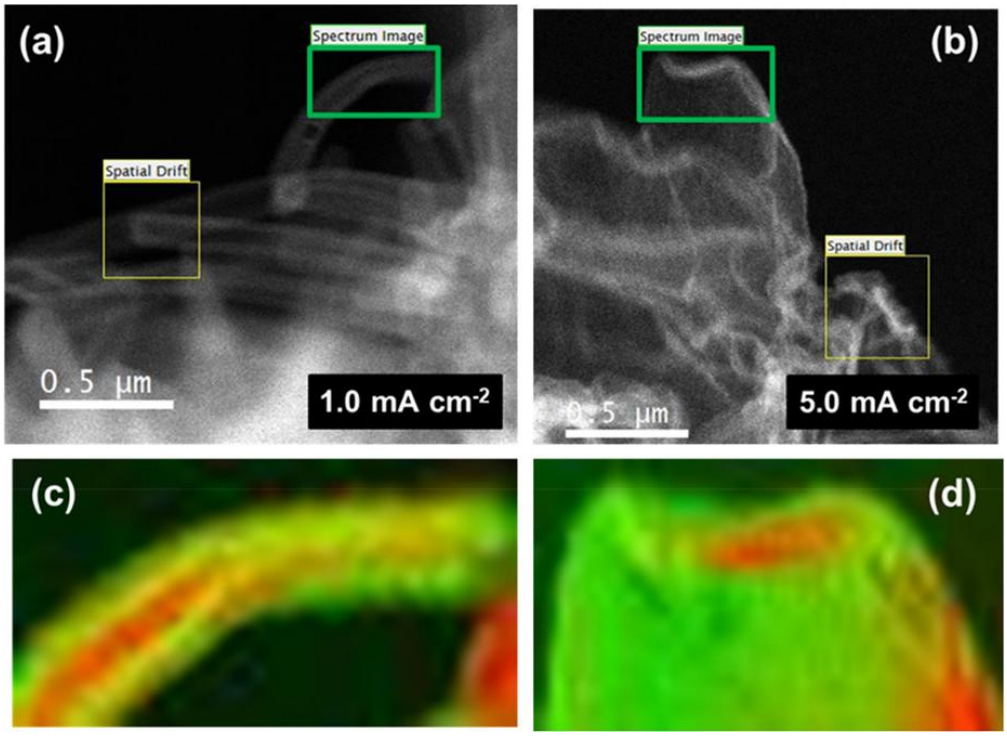

Figure 5. SEI characterization of electrodeposited Li metal in HCEs. (a, b) STEM and (c, d) EELS mapping images. The red and green areas indicate Li metal and Li_2O, respectively.

Figures 5(a) and 5(b) provide the STEM images of the electrodeposited Li metal at current densities of 1.0 and 5.0 mA cm^{-2}, respectively. Figures 5(c) and 5(d) show the EELS maps measured within the green frames indicated in Figures 5(a) and 5(b), respectively. The scan pitch of the EELS mapping is 10 nm, and the spectra at each point can be identified as Li (red) or Li_2O (green). The reference EELS spectra is utilized reported our previous study.[31] Here, only Li and Li_2O are analyzed for simplicity. The high-resolution TEM image (Figure S4(a)) displays the lattice pattern of the electrodeposited Li metal at 1.0 mA cm^{-2}. The selected area electron diffraction pattern

is shown in Figure S4(b), which displays the typical diffraction spot of Li metal corresponding to the (110) lattice spacing of 0.25 nm.[38]

The positions and directions of the EELS line measurements are indicated in the STEM images shown in Figures S4(c) and S4(d), where the scan pitch of the EELS mapping is 5 nm. The obtained transitions of the spectra are shown in Figures S4(e) and S4(f) and are consistent with the results of the mapping measurements. The thickness of the Li_2O layer is approximately 17.5 and 37.5 nm at 1.0 and 5.0 mA cm^{-2}, respectively. Such difference in layer thickness with current density is also confirmed when measuring other parts of electrodeposits. Here, the oxide layer thickness is defined as the distance between the position at which the Li_2O peak is no longer observed and the position at which the Li metal peak is no longer observed. With the same electrodeposition time, when electrodeposition was performed at 1.0 mA cm^{-2}, the amount of Li electrodeposited on the cathode surface was smaller than that at 5.0 mA cm^{-2}, and the amount of free SL molecules desolvated from Li^+ on the cathode surface was also lower, because only Li^+ ion is reduced on the electrode surface. This behavior was demonstrated by in-situ interferometry and Raman spectroscopy measurement. Therefore, as the current density increases, the electrodeposition reaction proceeds faster, and the amount of desolvated SL increases, leading to more side reactions. The thickness of the Li_2O-rich SEI layer on the deposited Li surface may vary with the number of side reactions. Other decomposition products may form at the electrode surface, however, the EELS spectra indicates that Li_2O is main species in the SEI layer. The progress of the electrodeposition causes the amount of free SL molecules near the electrode surface to increase. One of the reasons for the presence of Li_2O on the electrodeposited Li surface may be the dissociation of the S=O bonds within SL on the electrodeposited Li surface.[39] Because the electrodeposits

were uneven, the Li_2O-based SEI film was also considered to be nonuniform. This nonuniformity was one of the reasons behind the nonuniform current distribution. Therefore, the thicker the SEI film, the more uneven the progress of electrodeposition, leading to variations in morphology due to the current density.[40,41]

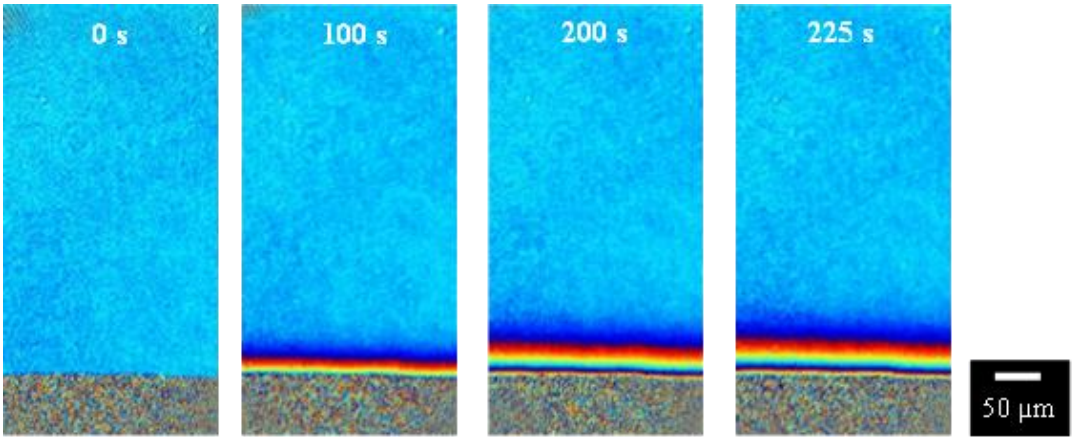

Figure 6. Phase shift profiles near the anode during Li electrochemical dissolution at 5.0 mA cm^{-2}.

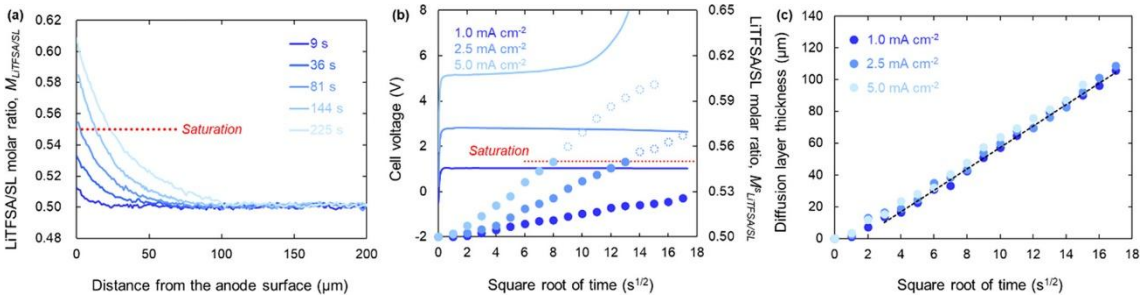

Figure 7. Development of LiTFSA concentration profile during the electrochemical dissolution of Li metal in HCEs. (a) Concentration profiles close to the anode during Li electrochemical dissolution. (b) Changes in the cell voltages (lines) and LiTFSA/SL molar ratios at the anode surface with respect to the square root of electrolysis time. (c) Diffusion layer thickness close to the anode with respect to the square root of electrolysis time.

Figure 6 demonstrates the phase changes close to the electrode during electrochemical dissolution at 5.0 mA cm^{-2}. As well as Figure 3, the color changes are corresponding to the development of concentration profile. Figure 7(a) shows the time variations of the concentration profiles close to the electrode during electrochemical dissolution. As electrochemical dissolution progresses, $M_{LiTFSA/SL}$ close to the anode increases. The growth of diffusion layers is also observed as well as the electrodeposition, and after 225 s, $M_{LiTFSA/SL}$ on the anode surface and the diffusion layer thickness, δ, reach 0.61 and 100 μm, respectively.

Figure 7(b) depict the changes in the cell voltage and anode surface concentrations as a function of $t^{1/2}$. The constant cell voltage immediately after the current application in the case of electrochemical dissolution. The $M^s_{LiTFSA/SL}$ values of anode begin to change in proportion to $t^{1/2}$. The saturation concentration of LiTFSA at room temperature (298 K) is approximately $M_{LiTFSA/SL}$ = 0.55 (Figures S5(a) and S5(b)); thus, supersaturation occurs on the anode surface. In the figures, the saturation concentration is indicated by a red horizontal dotted line ($M_{LiTFSA/SL}$ = 0.55), and the plots exceeding the saturation concentration are shown as open circles. The anode surface concentration also follows Eq. 1 as in the case of electrodeposition. The stagnation of increase of $M^s_{LiTFSA/SL}$ at anode is observed at about 100 seconds for 5.0 mA cm^{-2}. This stagnation can be explained by that anode surface concentration reaches the saturation. After 100 seconds, LiTFSA may have become supersaturated in SL and could not be completely dissolved. The cell voltage rapidly changed from 100 s at 5.0 mA cm^{-2}. This cell voltage divergence behavior is consistent with the three electrodes experimental result as shown as Fig. 2 (e). In addition, the viscosity of the electrolyte increases as the concentration increases, as shown in Figure S3. Therefore, the cause of the rapid increase in anode potential is the

inhibition of Li^+ transport close to the anode due to the increase in the viscosity of the electrolyte close to the anode and the supersaturation of LiTFSA at the anode surface.[42] The anode surface concentration exceeds the saturation concentration at current densities of 2.5 and 5.0 mA cm^{-2}. No overshoot of the anode potential is observed at 2.5 mA cm^{-2}. However, a voltage overshoot is evident at 5.0 mA cm^{-2}, when $M^s_{LiTFSA/SL}$ on the anode is close to the critical value of 0.57–0.58. Therefore, even at 2.5 mA cm^{-2}, if the anode surface concentration exceeds the critical value, voltage overshoot may occur owing to the influence of the high viscosity of the electrolyte near the anode. When $M^s_{LiTFSA/SL}$ on the anode has a concentration between the solubility and critical value, the supersaturation of LiTFSA may provide some conductivity to the electrolyte. Further, in this experiment, because the concentration of LiTFSA exceeds the solubility limit near the anode, the limiting current density is considered to be controlled by the mass transport on the anode side. Hence, the concentration increase close to the anode as electrochemical dissolution is more dominant than the stirring effect due to natural convection on a brief time scale of up to ~100 s.

Figure 7(c) shows the changes in δ as a function of $t^{1/2}$ during electrochemical dissolution. Once the diffusion layer formation commences, the δ increases in proportion to $t^{1/2}$ at all current densities. The apparent D is also calculated by Eq. 2, as well as the case of electrodeposition. The results are shown in Table 1 (a). D on the anode side, D_{anode} is 3.2–3.6 × 10^{-7} cm^2 s^{-1}; thus, D_{anode} is slightly smaller than $D_{cathode}$. This finding is consistent with the results of our previous study.[9] The difference in D between the two electrodes may be ascribed to the difference in the concentration close to the electrodes. Generally, D decrease with increasing concentration. When the anode and cathode are compared, the concentration boundary was defined as 1 % of the concentration difference.

Therefore, as the threshold value was larger for the anode, D was estimated to be small, which may have influenced the difference in D.

Figures S6(a) and S6(b) show the molar concentrations of LiTFSA at the electrode surface converted from the cathode or anode $M^s_{LiTFSA/SL}$, respectively. Here, the coefficient $t^{1/2}$ in Eq. 1 corresponds to the slope of the approximate straight line plotted in the range in which C^s changes in proportion to $t^{1/2}$. Therefore, t^* may also be estimated using D as shown in Table 1(a). t^* on the cathode or anode side, $t^*_{cathode}$ or t^*_{anode}, is 0.69–0.74 or 0.72–0.74 (Table 1(b)), respectively, and is constant regardless of the electrode or current density. Additionally, these values are similar to those obtained in previous studies by nuclear magnetic resonance (NMR) and impedance spectroscopy, as shown in Table 1(c).[43]

Table 1. (a) Apparent diffusion coefficients D and (b) apparent transport numbers t^* of Li^+ at 1.0, 2.5, and 5.0 mA cm^{-2}, respectively. (c) Comparison of t^* obtained by NMR and impedance spectroscopies.

(a)

current density [mA cm^{-2}]	1.0	2.5	5.0
$D_{cathode}$[cm^2 s^{-1}]	4.6×10^{-7}	4.1×10^{-7}	4.2×10^{-7}
D_{anode}[cm^2 s^{-1}]	3.5×10^{-7}	3.2×10^{-7}	3.6×10^{-7}

(b)

current density [mA cm^{-2}]	1.0	2.5	5.0
$t^*_{cathode}$	0.71	0.69	0.74
t^*_{anode}	0.73	0.72	0.74

(c)

	NMR spectroscopy	impedance spectroscopy	interferometry
t^*	0.61	0.68	0.69–0.74

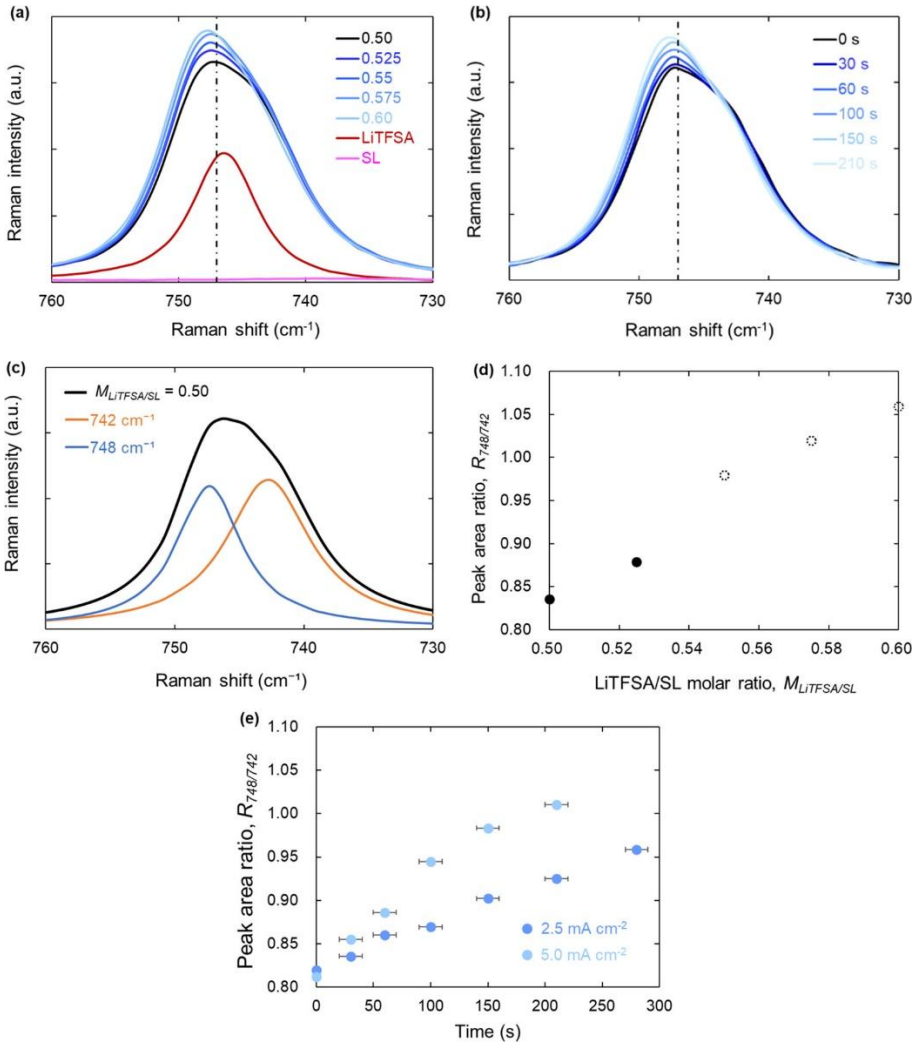

Figure 8. Time transition of solvation structure of Li^+ during the electrochemical dissolution of Li metal in HCEs. (a) Raman spectra in the range 730–760 cm^{-1} of the electrolytes containing LiTFSA and SL in different ratios. (b) In situ Raman spectra in the range 730–760 cm^{-1} of the electrolyte close to the cathode during Li electrodeposition at a current density of 5.0 mA cm^{-2}. (c) Peak deconvolution of the Raman spectrum in the range 730–760 cm^{-1} of the electrolyte containing an LiTFSA/SL molar ratio of 0.50. (d) Ratios of the areas of the peaks at 742 and 748 cm^{-1} obtained via peak deconvolution of Figure 6(a). (e) Ratios of the areas of the peaks at 742 and 748 cm^{-1} obtained via peak deconvolution of the in situ Raman spectra in the range 730–760 cm^{-1}.

Figure 8(a) shows the concentration dependences of the Raman spectra of the electrolyte, LiTFSA powder, and SL at 730–760 cm^{-1} in higher concentration region than 0.50 of $M_{LiTFSA/SL}$. Herstedt et al. observed CF_3 bending coupled with the S–N stretching vibration of TFSA at 740–750 cm^{-1}, with the spectrum changing sensitively depending on Li^+ coordination.[44] Typical peaks corresponding to TFSA were observed at 739–742 and 745–755 cm^{-1}, corresponding to uncoordinated and electrostatically coordinated $TFSA^-$ with Li^+, respectively. A peak representing LiTFSA was observed at ~746 cm^{-1}. As $M_{LiTFSA/SL}$ increased from 0.50, this peak shifted to a higher wavenumber, and its intensity increased, suggesting that as $M_{LiTFSA/SL}$ increased, $TFSA^-$ coordination with Li^+ increased.

Figure 8(b) shows the changes in the Raman spectrum of the electrolyte with time in the range 730–760 cm^{-1} at ~10 μm from the electrode surface during Li electrochemical dissolution at a current density of 5.0 mA cm^{-2}. The peak intensity is the lowest prior to the experiment. As electrochemical dissolution proceeds, the peak intensity increases, and the peak position shifts toward a higher wavenumber because the concentration of $TFSA^-$ coordinated with Li^+ close to the anode increases. This increase in concentration indicated by the changes in the Raman spectrum is consistent with the interferometry results.

Figure 8(c) shows the deconvolution of the Raman spectrum at $M_{LiTFSA/SL} = 0.50$ into two peaks at 742 and 748 cm^{-1}. The Raman spectra of other $M_{LiTFSA/SL}$ electrolytes were also peak-fitted, and the ratios of the areas of the peaks at 748/742 cm^{-1}, $R_{748/742}$, were calculated. $R_{748/742}$ represents the difference in the coordination states of Li^+ and

$TFSA^-$. The calculated $R_{748/742}$ values are shown in Figure 8(d), with $R_{748/742}$ increasing with increasing $M_{LiTFSA/SL}$. Figure 8(e) shows the $R_{748/742}$ values obtained using in situ Raman spectroscopy during Li electrochemical dissolution at 2.5 and 5.0 mA cm^{-2}. The $R_{748/742}$ values at both current densities increase with time, with $R_{748/742}$ increasing faster at 5.0 mA cm^{-2} than at 2.5 mA cm^{-2}. Close to the electrode surface, the concentration increases as the electrochemical dissolution of Li metal proceeds, and the coordination structure around Li^+ changes, accompanied by the development of the concentration profile. This interface behavior is critical in analyzing the characteristics of Li metal electrodes, particularly in HCEs.

2.4 Conclusions

In this study, the ionic mass transfer and deposition morphology associated with Li electrodeposition/electrochemical dissolution in a 1:2 LiTFSA:SL HCE were investigated using several techniques, including digital microscopy, laser interferometry, Raman spectroscopy, SEM, and TEM. The electrodeposition of Li metal induced an increase in the number of uncoordinated solvent molecules close to the electrode surface. This discrepancy in the bulk electrolyte structure enhanced the SL-decomposition reaction, forming an SEI layer on the electrodeposited Li metal. Therefore, lower current density is desirable in this electrolyte. Electrochemical dissolution induced a LiTFSA concentration increase close to the electrode surface, yielding a supersaturated state, which caused an increase in viscosity and decreased the conductivities, to result in the divergence of cell voltage. This behavior suggested that a large current is a critical problem for HCEs, even though the battery cells had very small electrode distances, corresponding to the separator thickness. Both the electrodeposition and electrochemical dissolution behaviors suggest that a low current density of 1.0 mA cm^{-2} is optimal for HCE systems. Some diluents may have the ability to help overcome this difficulty. Actually, Wu et al. reported that proper selection of diluent solvent enhance the Li metal anode characteristics,[45] hence, the effect of diluents on HCEs is our next research target. Furthermore, interferometry was used to estimate the apparent diffusion coefficient and transport number, based on the concentration profile close to the electrode surface. This technique should provide insight into ionic mass transfer within battery electrolytes and the relationship between morphological variations in electrodeposited metal and ionic mass transfer, which will facilitate the design of the interface between the metal electrode and electrolyte for next-generation batteries.

2.5 Additional experiments

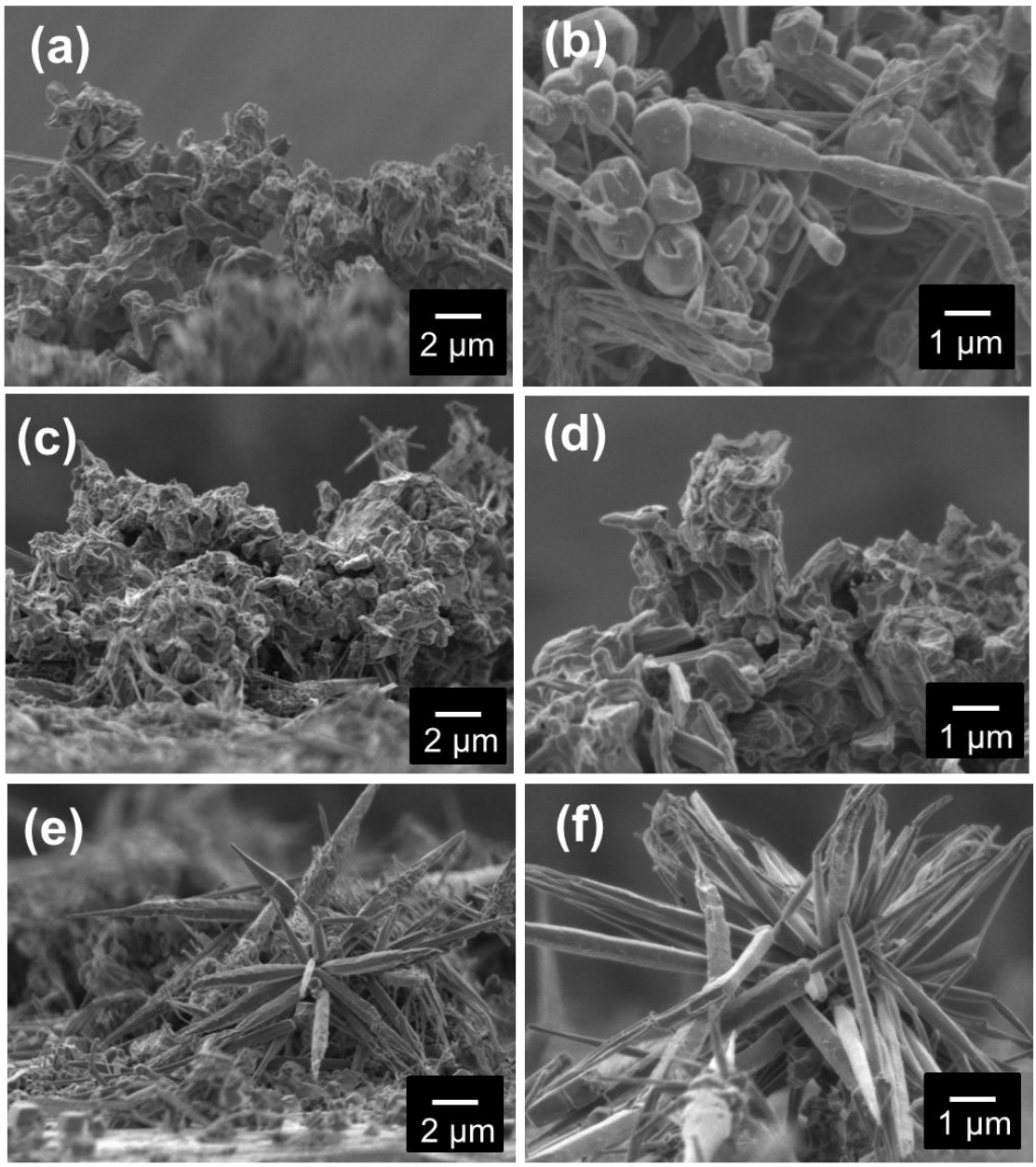

Figure S1. SEM images of the cathode surface after electrodeposition at (a, b) 1.0, (c, d) 2.5, and (e, f) 5.0 mA cm^{-2}.

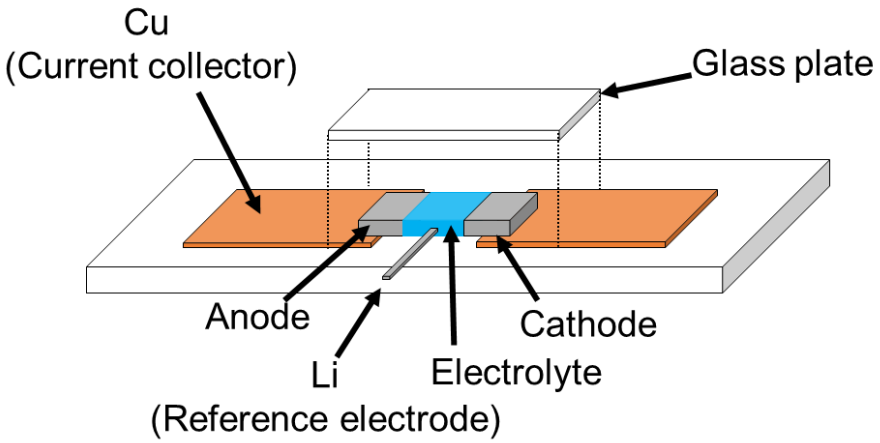

Figure S2. Schematic of the three-electrode electrochemical cell.

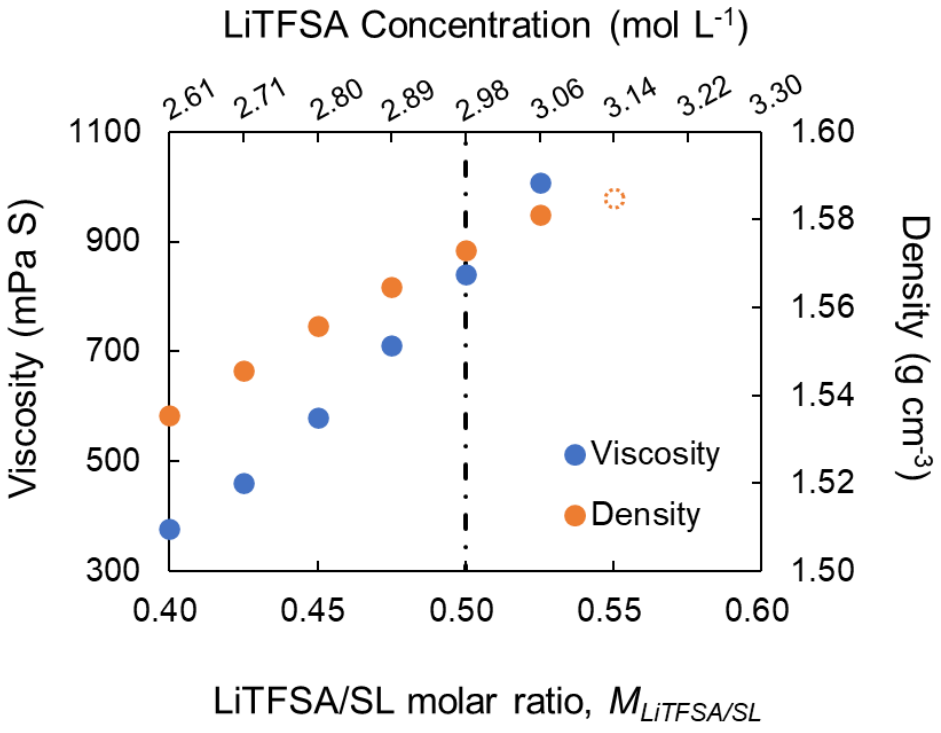

Figure S3. Viscosities and densities of the LiTFSA-SL solutions with various compositions.

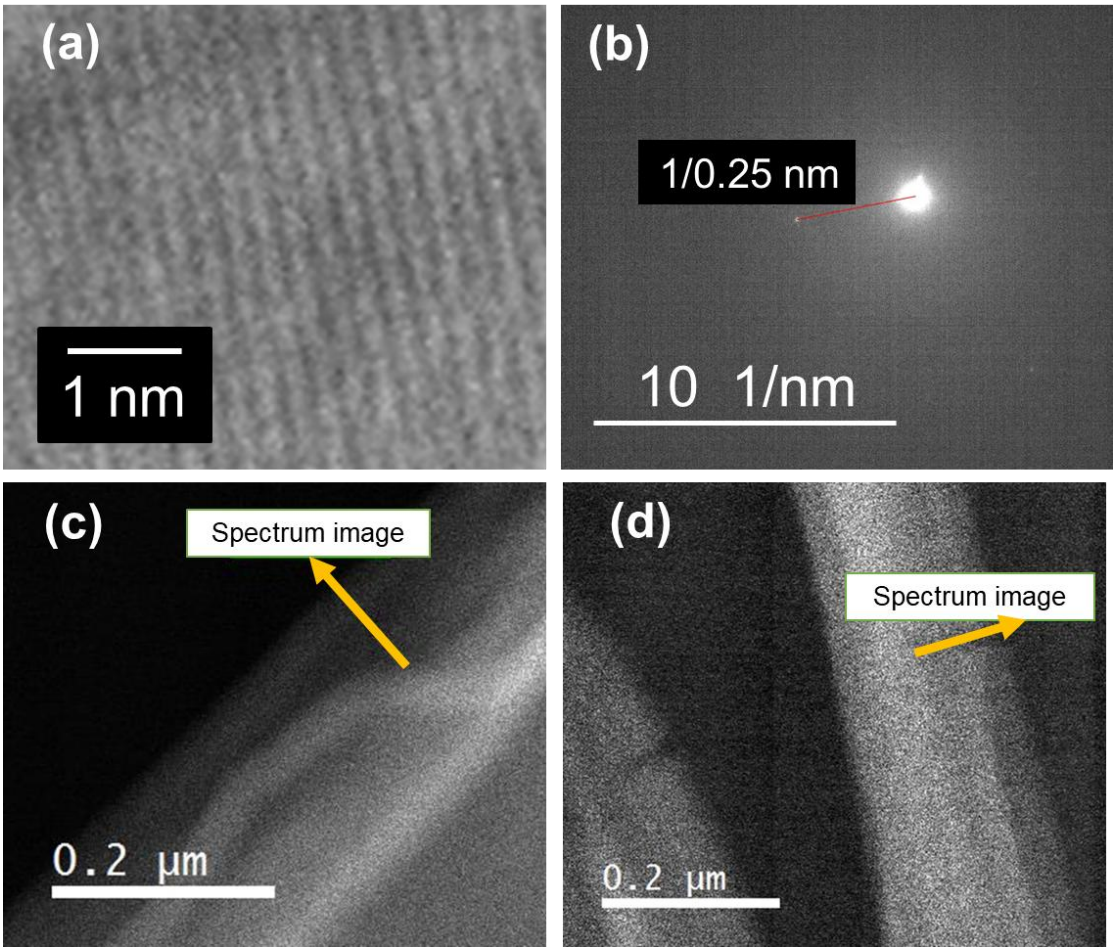
(a)
1 nm
(b)
1/0.25 nm
10 1/nm
(c)
Spectrum image
0.2 µm
(d)
Spectrum image
0.2 µm

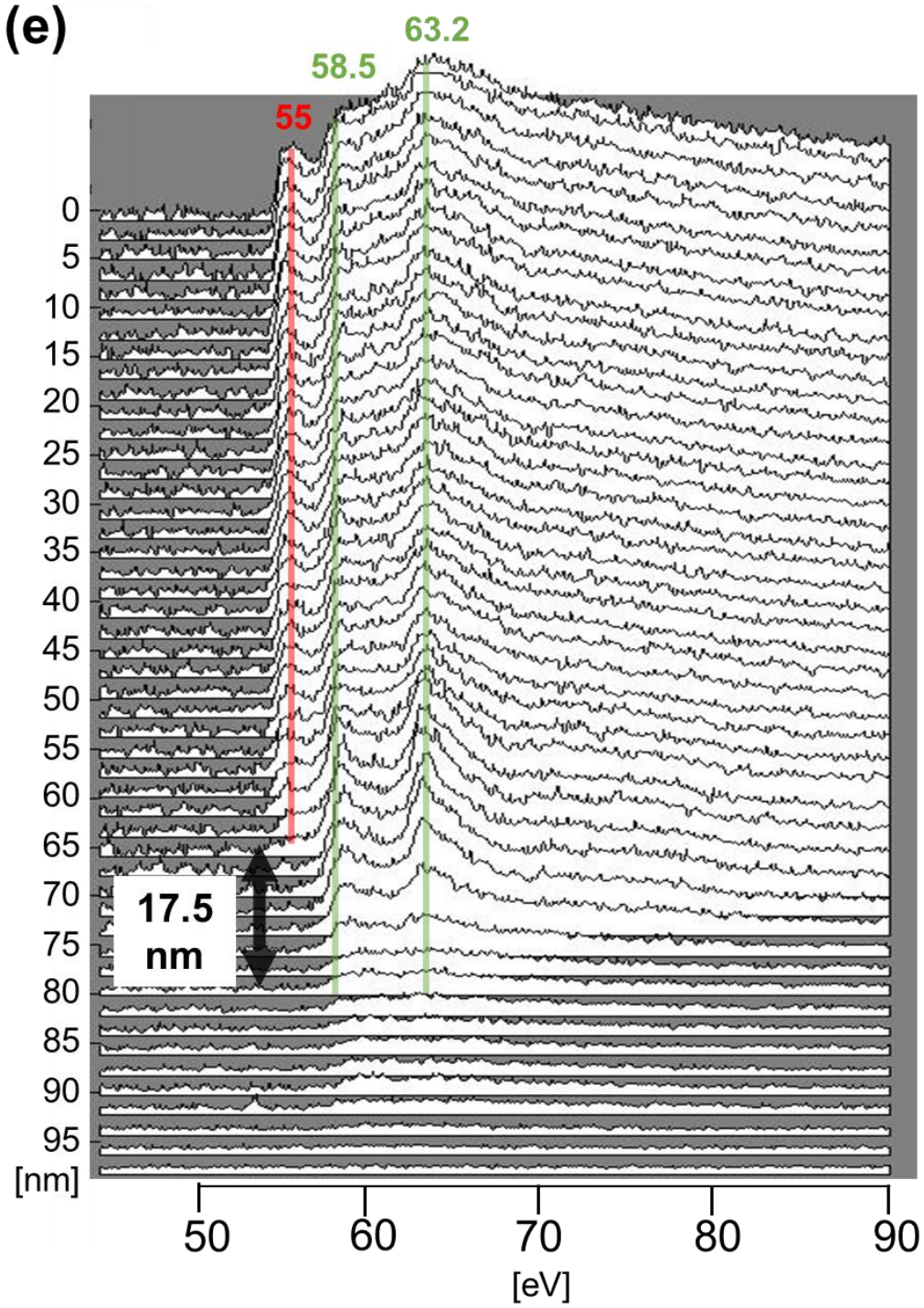
(e)
63.2
58.5
55
0
5
10
15
20
25
30
35
40
45
50
55
60
65
70
75
80
85
90
95
[nm]
17.5
nm
50
60
70
80
90
[eV]

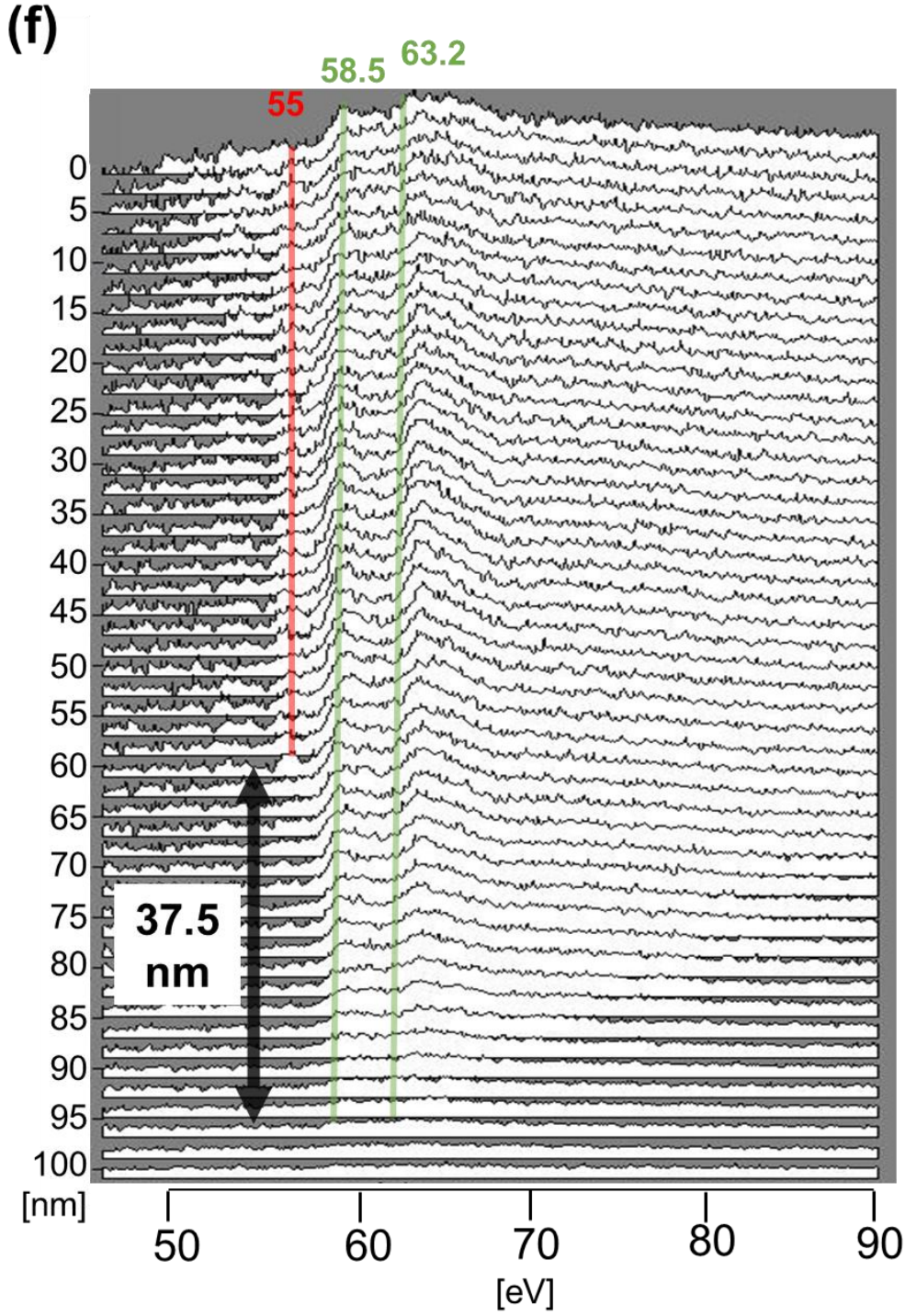

Figure S4. (a) TEM and (b) TEM diffraction images of the electrodeposited Li surface at a current density of 1.0 mA cm^{-2}. STEM images of the electrodeposited Li surface at (c) 1.0 and (d) 5.0 mA cm^{-2} for STEM-EELS line measurement (e), (f).

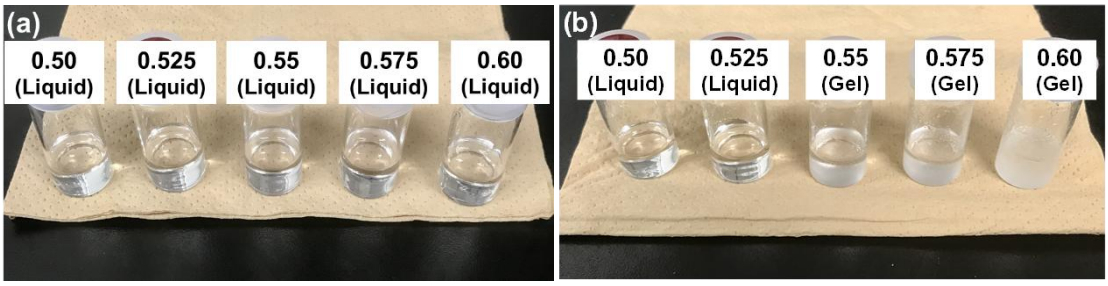

Figure S5. LiTFSA-SL solutions allowed to stand at room temperature for (a) 1 d and (b) 1 wk after preparation. The solutions from left to right contain LiTFSA/SL molar ratios of 0.50, 0.525, 0.55, 0.575, and 0.60, respectively.

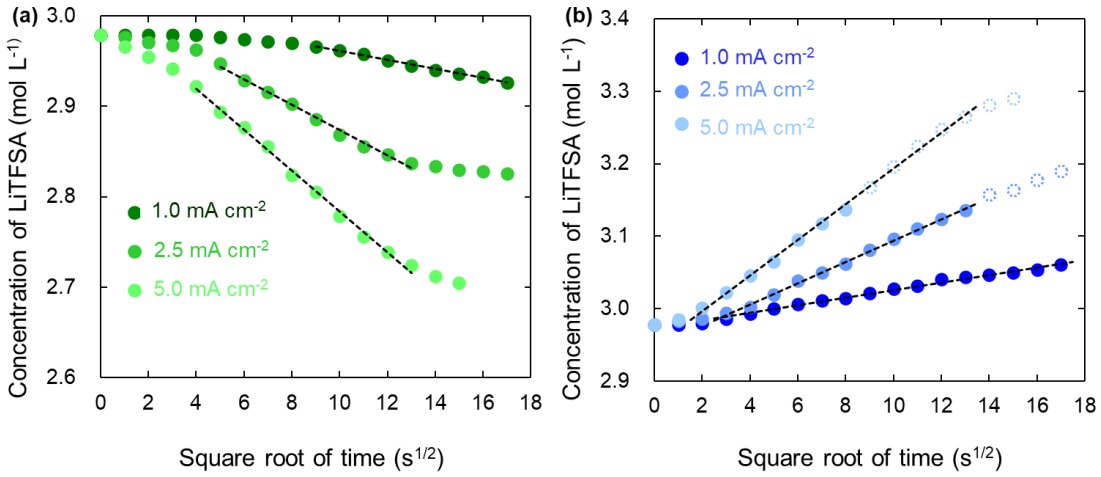

Figure S6. Molar concentration changes at the (a) cathode and (b) anode surfaces. These plots are based on Figure 1(d) and Figure 4 (b), respectively.

References

[1] F. Wu, J. Maier, Y. Yu, *Chemical Society Reviews* **2020**, *49*, 1569–1614.

[2] R. Wang, W. Cui, F. Chu, F. Wu, *Journal of Energy Chemistry* **2020**, *48*, 145–159.

[3] Y. Zhang, T.-T. Zuo, J. Popovic, K. Lim, Y.-X. Yin, J. Maier, Y.-G. Guo, *Materials Today* **2020**, *33*, 56–74.

[4] P. Verma, P. Maire, P. Novák, *Electrochimica Acta* **2010**, *55*, 6332–6341.

[5] P. Bai, J. Li, F. R. Brushett, M. Z. Bazant, *Energy & Environmental Science* **2016**, *9*, 3221–3229.

[6] Y. Li, W. Huang, Y. Li, A. Pei, D. T. Boyle, Y. Cui, *Joule* **2018**, *2*, 2167–2177.

[7] K. Nishikawa, Y. Fukunaka, T. Sakka, Y. H. Ogata, J. R. Selman, *Journal of The Electrochemical Society* **2007**, *154*, A943.

[8] K. Nishikawa, T. Mori, T. Nishida, Y. Fukunaka, M. Rosso, *Journal of electroanalytical chemistry* **2011**, *661*, 84–89.

[9] A. Miki, K. Nishikawa, G. Kamesui, H. Matsushima, M. Ueda, M. Rosso, *Journal of Materials Chemistry A* **2021**, *9*, 14700–14709.

[10] S. Kawai, K. Nishikawa, Y. Fukunaka, S. Kida, *Electrochimica Acta* **2007**, *53*, 257–264.

[11] S. Kawai, K. Nishikawa, Y. Fukunaka, S. Kida, *Electrochemistry* **2009**, *77*, 601–603.

[12] M. C. Ribeiro, L. G. C. Rego, P. C. T. D'Ajello, *Journal of Electroanalytical Chemistry* **2009**, *628*, 21–26.

[13] T. Nishida, K. Nishikawa, M. Rosso, Y. Fukunaka, *Electrochimica acta* **2013**, *100*, 333–341.

[14] Y. Yamada, A. Yamada, *Journal of The Electrochemical Society* **2015**, *162*, A2406.

[15] D. J. Eyckens, L. C. Henderson, *Frontiers in chemistry* **2019**, *7*, 263.

[16] Y. Yamada, K. Furukawa, K. Sodeyama, K. Kikuchi, M. Yaegashi, Y. Tateyama, A. Yamada, *Journal of the American Chemical Society* **2014**, *136*, 5039–5046.

[17] K. Sodeyama, Y. Yamada, K. Aikawa, A. Yamada, Y. Tateyama, *The Journal of Physical Chemistry C* **2014**, *118*, 14091–14097.

[18] L. Chen, X. Fan, E. Hu, X. Ji, J. Chen, S. Hou, T. Deng, J. Li, D. Su, X. Yang, *Chem* **2019**, *5*, 896–912.

[19] S. Ko, Y. Yamada, A. Yamada, *Batteries & Supercaps* **2020**, *3*, 910–916.

[20] S. Ko, Y. Yamada, A. Yamada, *Joule* **2021**, *5*, 998–1009.

[21] A. Mistry, V. Srinivasan, *Joule* **2021**, *5*, 2773–2776.

[22] A. A. Wang, A. B. Gunnarsdóttir, J. Fawdon, M. Pasta, C. P. Grey, C. W. Monroe, *ACS energy letters* **2021**, *6*, 3086–3095.

[23] F. R. McLarnon, R. H. Muller, C. W. Tobias, *JOSA* **1975**, *65*, 1011–1018.

[24] F. R. McLarnon, R. H. Muller, C. W. Tobias, *Electrochimica Acta* **1976**, *21*, 101–105.

[25] Y. Konishi, Y. Nakamura, Y. Fukunaka, K. Tsukada, K. Hanasaki, *Electrochimica acta* **2003**, *48*, 2615–2624.

[26] K. Nishikawa, T. Saito, H. Matsushima, M. Ueda, *Electrochimica Acta* **2019**, *297*, 1104–1108.

[27] A. Miki, K. Nishikawa, T. Ozawa, H. Matsushima, M. Ueda, *Journal of The Electrochemical Society* **2020**, *167*, 062501.

[28] G. Kamesui, K. Nishikawa, H. Matsushima, M. Ueda, *Journal of The Electrochemical Society* **2021**, *168*, 031507.

[29] E.-S. M. Sherif, R. M. Erasmus, J. D. Comins, *Electrochimica Acta* **2010**, *55*, 3657–

3663.

[30] F. Wang, J. Graetz, M. S. Moreno, C. Ma, L. Wu, V. Volkov, Y. Zhu, *ACS nano* **2011**, *5*, 1190–1197.

[31] K. Nishikawa, K. Shinoda, *The Journal of Physical Chemistry Letters* **2021**, *12*, 3922–3927.

[32] K. Kanamura, S. Shiraishi, Z. Takehara, *Journal of the Electrochemical Society* **1996**, *143*, 2187.

[33] K. Nishikawa, T. Mori, T. Nishida, Y. Fukunaka, M. Rosso, T. Homma, *Journal of The Electrochemical Society* **2010**, *157*, A1212.

[34] K. Dokko, D. Watanabe, Y. Ugata, M. L. Thomas, S. Tsuzuki, W. Shinoda, K. Hashimoto, K. Ueno, Y. Umebayashi, M. Watanabe, *The Journal of Physical Chemistry B* **2018**, *122*, 10736–10745.

[35] A. Nakanishi, K. Ueno, D. Watanabe, Y. Ugata, Y. Matsumae, J. Liu, M. L. Thomas, K. Dokko, M. Watanabe, *The Journal of Physical Chemistry C* **2019**, *123*, 14229–14238.

[36] A. Mistry, C. Fear, R. Carter, C. T. Love, P. P. Mukherjee, *ACS Energy Letters* **2018**, *4*, 156–162.

[37] X. Xuan, J. Wang, J. Lu, N. Pei, Y. Mo, *Spectrochimica Acta Part A: Molecular and Biomolecular Spectroscopy* **2001**, *57*, 1555–1560.

[38] Y. Gao, Z. Yan, J. L. Gray, X. He, D. Wang, T. Chen, Q. Huang, Y. C. Li, H. Wang, S. H. Kim, *Nature materials* **2019**, *18*, 384–389.

[39] T. Kaneko, K. Sodeyama, *Chemical Physics Letters* **2021**, *762*, 138199.

[40] M. Xu, W. Li, B. L. Lucht, *Journal of Power Sources* **2009**, *193*, 804–809.

[41] Y. Ugata, R. Tatara, T. Mandai, K. Ueno, M. Watanabe, K. Dokko, *ACS Applied*

Energy Materials **2021**, *4*, 1851–1859.

[42] H. Hirayama, N. Tachikawa, K. Yoshii, M. Watanabe, Y. Katayama, *Electrochemistry* **2015**, *83*, 824–827.

[43] K. Shigenobu, K. Dokko, M. Watanabe, K. Ueno, *Physical Chemistry Chemical Physics* **2020**, *22*, 15214–15221.

[44] M. Herstedt, M. Smirnov, P. Johansson, M. Chami, J. Grondin, L. Servant, J. C. Lassègues, *Journal of Raman Spectroscopy: An International Journal for Original Work in all Aspects of Raman Spectroscopy, Including Higher Order Processes, and also Brillouin and Rayleigh Scattering* **2005**, *36*, 762–770.

[45] Z. Wu, H. Liu, J. Holoubek, C. Anderson, L. Shi, H. Khemchandani, D. Lu, D. Liu, C. Niu, J. Xiao, *ACS Energy Letters* **2022**, *7*, 2701–2710.

Chapter 3: In situ observation of the formation and relaxation processes of concentration gradients in a lithium bis(fluorosulfonyl) amide–tetraglyme solvate ionic liquid using digital holographic interference microscopy

3.1 Introduction

Lithium-ion batteries (LIBs) are widely used as power sources for portable devices owing to their high energy densities. In addition, their high capacity and reliability enable the use of LIBs in various applications, ranging from electric vehicles (EVs) to satellites. However, the theoretical capacity of LIBs has already been realized [1,2]; therefore, further improvements in the performance of LIBs will depend on improving their energy density. Accordingly, innovative approaches utilizing next-generation battery materials are required [3,4].

In 2010, Watanabe et al. developed a solvate ionic liquid (SIL), which consisted of an equimolar mixture of Li salts and tetraglyme (G4), for the first time [5]. In SILs, Li^+ and G4 form complexes via chelation. Similar to ionic liquids, SILs exhibit a high decomposition resistance and low vapor pressure [6,7], rendering them promising electrolyte candidates for application in Li–sulfur [8] and Li–metal batteries [9].

In an LIB with an SIL electrolyte, a concentration profile forms in the electrolyte near the electrode during electrolysis. The concentration gradient (CG) induces ionic mass transfer and has a significant effect on the Li deposition morphology [10], solid-electrolyte interphase formation [11,12], and cell voltage [13]. Simulations suggest that the concentration profile forms even at a short inter-electrode distance of 15 μm, which is a standard distance in existing batteries [14,15]. New storage batteries, particularly those used in EVs, require fast charge–discharge operations, which results in the formation of a steep CG. The start-up–shutdown protocol should be considered, and the spontaneous CG relaxation process, which occurs when no current is applied, is also an important issue [16,17].

Several studies have observed concentration profiles using magnetic resonance

imaging (MRI) [17], nuclear magnetic resonance (NMR) spectroscopy [18], and Raman spectroscopy [14]. Although these methods are suitable for noncontact measurements, the experimental cells used in NMR and MRI have long distances (approximately 8 mm) between the anode and cathode. In addition, these techniques require a high magnetic field strength, which may influence diffusion in the electrolyte. Raman spectroscopy employs scattered light, which may reduce the resolution of measurements. Takamatsu et al. obtained high-resolution measurements of a concentration profile during electrolysis using a synchrotron [19]; however, this method requires a large facility and cannot be performed rapidly.

Laser interferometry was first reported in the 1970s [20,21]. This technique is noncontact, nondestructive, and capable of detecting small changes in concentration using the interference (phase shift) of two types of light. In addition, the transition in the concentration profile can be visualized by recording the refractive index corresponding to the concentration as a hologram. Previous studies directly calculated ion diffusion coefficients at the open circuit potential (OCP) from the slope of the OCP–time relationship and the interelectrode distance [14,17]. A tabletop digital holographic interference microscopy (DHM) system was used to observe the concentration profile near the anode and cathode. Previously, only one side of the electrode was used [11,12,22,23]. Here, the short inter-electrode distance of 600 μm allowed the simultaneous observation of the vicinities of both electrodes. Simultaneous observation of CG in the electrolyte at both electrodes revealed that the concentration distribution near both electrodes was asymmetric and that the diffusivity of ions was different. Furthermore, the diffusion layers formed around the anode and cathode overlapped during the relaxation of the concentration profile.

We used an SIL consisting of equimolar amounts of lithium bis(fluorosulfonyl) amide (LiFSA) and G4 as the electrolyte and observed the concentration profile in situ during and after electrolysis. The profile was calculated from the holograms obtained using interferometry. The Li^+ diffusion coefficients were then calculated from the electrode surface concentration. Directly observing the concentration profile during and after electrolysis in a pseudo-battery environment will significantly improve our understanding of ionic mass transfer in the battery electrolyte.

3.2 Experimental

Mixtures of LiFSA (99.9%, Nippon Shokubai Co., Ltd.) and G4 (98%, Kishida Chemical Co., Ltd.) were used as electrolytes. The LiFSA/G4 molar ratio of the electrolytes, $M_{\mathrm{LiFSA/G4}}$, was 0.7, 0.8, 0.9, 1.0, 1.1, 1.2 and 1.3. A schematic of the experimental cell is shown in Figure 1. The electrochemical cell was fabricated as follows. First, Cu current collectors with a thickness of 5 μm were laid on a glass plate. Thereafter, 200 μm-thick Li plates (99.9%, Honjo Metal Co., Ltd.) were placed on the Cu current collectors as the anode and cathode. The electrodes were connected in parallel with an inter-electrode distance of 600 μm in a quasi-two-dimensional cell configuration to minimize the influence of natural convection. The reaction area of each electrode measured 200 μm × 15 mm. Another glass plate was placed over both electrodes and fixed with epoxy resin. Finally, the electrolyte was injected between the two electrodes, and the Cu current collectors were connected to a potentiostat (SP150, Bio-Logic) for the electrochemical experiments. All electrolytes and experimental cells were prepared in a dry room with a dew point below -50 °C.

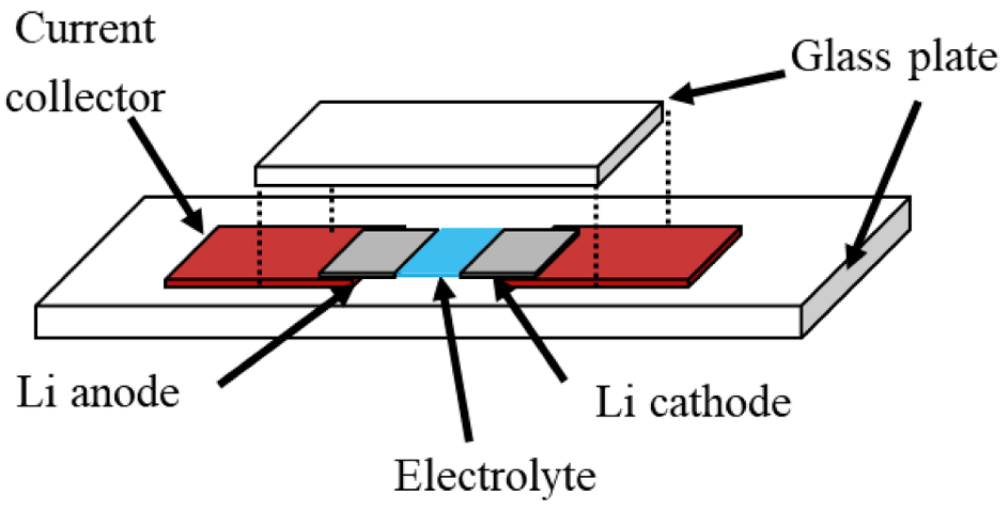

Figure 1. Schematic of the electrochemical cell.

The viscosity and density of the electrolyte were measured using a rolling-ball viscometer (Lovis 2000ME, Anton Paar), and the refractive indices were determined using a digital refractometer (RX-7000α, ATAGO). Electrochemical experiments were performed for 100 s using an electrolyte with $M_{\mathrm{LiFSA/G4}} = 1.0$ at a constant current density of 3.0 mA cm^{-2}. After stopping the current, the CG near the anode and cathode was relaxed for 1700 s.

The in-situ observation of the LiFSA concentration profile was conducted during and after electrolysis using DHM (Lyncee Tec), following an established procedure [22]. The wavelength of the laser beam was 683.6 nm, and the optical path length was set to 200 µm. The magnification of the objective lens was five times. The obtained holograms were converted to a concentration profile based on the relationship between the refractive index and concentration (Eqs. (1) to (3)) using the Koala software (Lyncee Tec).

$$\Delta n = \left(\frac{\partial n}{\partial C}\right)\Delta C \tag{1}$$

$$d\Delta n = \left(\frac{\Delta\theta}{2\pi}\right)\lambda \tag{2}$$

Here, Δn is the change in the refractive index; ΔC is the change in the LiFSA concentration; d is the optical path length (0.20 mm); $\Delta\theta$ is the phase change of the electrolyte refractive index; and λ is the laser wavelength (683.6 nm.). Combining Eq. (1) and Eq. (2) yields Eq. (3):

$$\Delta C = \left(\frac{\partial C}{\partial n}\right)\left(\frac{\Delta\theta}{2\pi}\right)\frac{\lambda}{d} \tag{3}$$

$\Delta\theta$ was measured via DHM and substituted into Eq. 3 to yield the concentration profile.

3.3 Results and Discussion

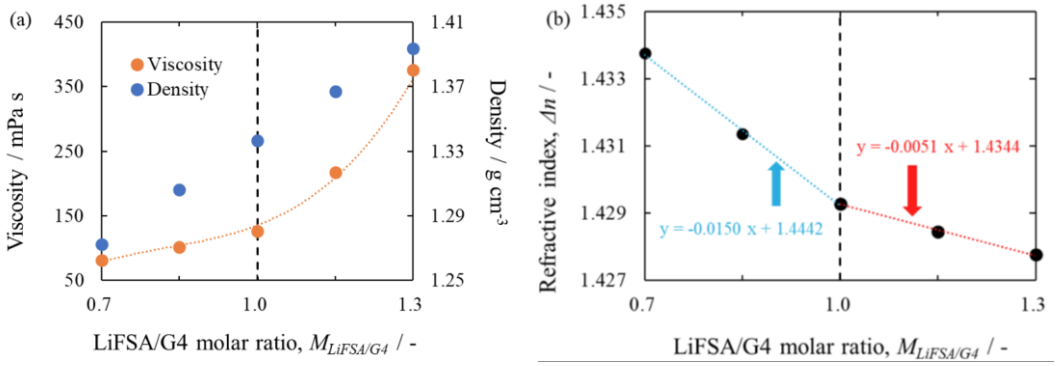

Figure 2. (a) Viscosity and density; (b) refractive index of the electrolytes.

The viscosities and densities of the electrolytes are shown in Figure 2(a). The viscosity increased only slightly at $M_{\mathrm{LiFSA/G4}} \leq 1.0$; however, it increased exponentially at $M_{\mathrm{LiFSA/G4}} \geq 1.0$. The density increased proportionally with $M_{\mathrm{LiFSA/G4}}$. The slope changed slightly at approximately $M_{\mathrm{LiFSA/G4}} = 1.0$. Similar to our previous results for LiTFSA–G4 mixtures [11], the physicochemical properties of the electrolyte containing equimolar amounts of Li salts and G4 differed from those of electrolytes containing non equimolar mixtures. The refractive indices of the electrolytes are shown in Figure 2(b). The slope of the approximate straight line, $\Delta n/\Delta C$, was -0.0150 at $0.7 \leq M_{\mathrm{LiFSA/G4}} \leq 1.0$ and -0.0051 at $1.0 \leq M_{\mathrm{LiFSA/G4}} \leq 1.3$. The concentration changes during and after electrolysis were calculated from these gradients using Eq. 3.

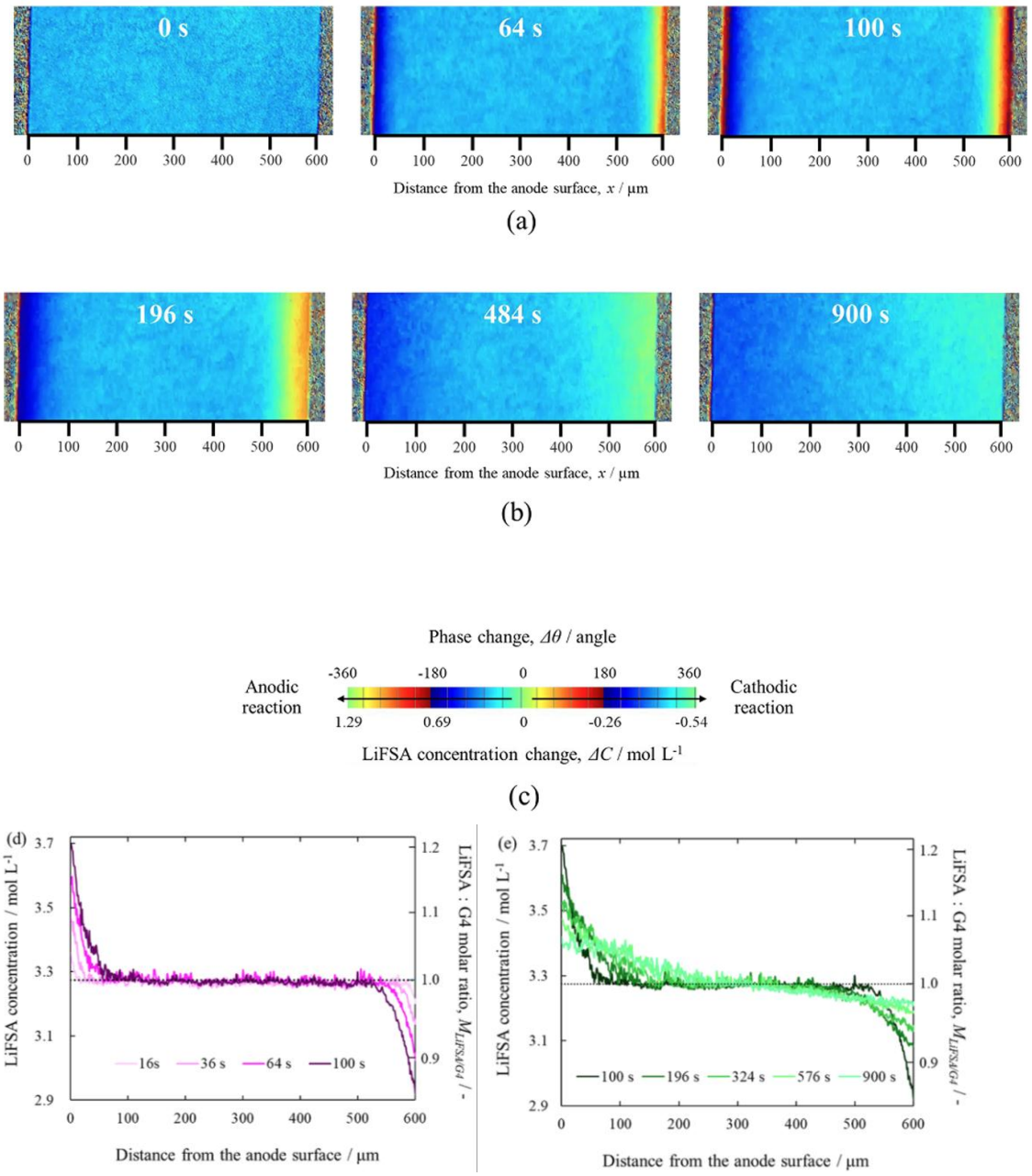

Figure 3. Holograms of the electrolyte (a) during and (b) after electrolysis. (c) Relationship between the LiFSA concentration and color change with the phase change. Speckled areas on the left and right represent the anode and cathode, respectively, and the light blue area in the center represents the electrolyte. Time variation of concentration profiles (d) during and (e) after electrolysis.

DHM snapshots (Figure 3) and a short video (Supplementary Video) reveal the phase change that occurs in the electrolyte (a) during and (b) after electrolysis. The relationship between the color change of the hologram and the LiFSA concentration is shown in Figure 3(c). During electrolysis (0–100 s), diffusion layers were formed on the surfaces of the electrodes and grew into the bulk electrolyte. The thickness of these layers increased with the electrolysis time. The electrolyte concentration increased near the anode and decreased near the cathode. After electrolysis (100–1800 s), the diffusion layers grew further in the bulk direction, whereas the CGs were reduced.

Figure 3(d) shows the temporal variation of the concentration profile during electrolysis. The molar concentration of LiFSA was calculated from the electrolyte density and $M_{\mathrm{LiFSA/G4}}$. In this study, the electrolyte's Li^+ and FSA^- concentrations are always assumed to be equal in the observation area. Therefore, the Li^+ concentration change in the electrolyte coincides with the change in LiFSA concentration. Li^+ concentration increased near the anode. Li^+ diffused toward the bulk in a solvated state with G4, driven mainly by the concentration gradient of electrolysis. As a result, the diffusion layer thickness, δ, also increased. We herein define the concentration boundary as the point at which a difference of 1% is observed between the concentration of LiFSA at the electrode surface and that in the bulk. At 100 s, the electrode surface concentration (Cs) and δ were 3.69 mol L^{-1} and 84 μm, respectively. The Li^+ concentration decreased near the cathode. Li^+, supplied from the bulk side was desolvated by G4 and deposited on the cathode surface. This led to the increase of δ near the cathode. At 100 s, Cs and δ were 2.91 mol L^{-1} and 92 μm, respectively. After electrolysis, Cs on the anode and cathode changed by +0.43 and -0.35 mol L^{-1}, respectively, resulting in an asymmetric concentration profile.

The time transition of the relaxation of the concentration profile is shown in Figure 3(e). The legend in the figure indicates the time after starting the electrolysis. On the anode side, the CG was gradually relaxed while maintaining $M_{\mathrm{LiFSA/G4}} \geq 1.0$. Cs slowly decreased with increasing relaxation time, whereas δ steadily increased; at 900 s, Cs and δ were 3.44 mol L^{-1} and 282 μm, respectively. On the cathode side, the electrolyte maintained a molar ratio $M_{\mathrm{LiFSA/G4}} \leq 1.0$ during the CG relaxation process. Cs gradually increased, and δ constantly increased with time; Cs and δ were 3.22 mol L^{-1} and 297 μm, respectively, at 900 s. The concentration profile was initially asymmetric during electrolysis, and the degree of asymmetry increased with increasing relaxation time. The reason for this phenomenon will be discussed later. The supplementary video shows that the diffusion layers near the electrodes overlap after approximately 1000 s. The concentration profile continues to relax over the entire electrolyte until the end of the observation period. In the interferometry used in this study, ΔC was calculated from $\Delta\theta$ by the bulk solution. The region where $\Delta\theta = 0$ existed until the diffusion layers overlapped, so ΔC could be calculated. However, as soon as the diffusion layers overlapped at 1000 s, ΔC could not be determined because it was unclear where the bulk region was.

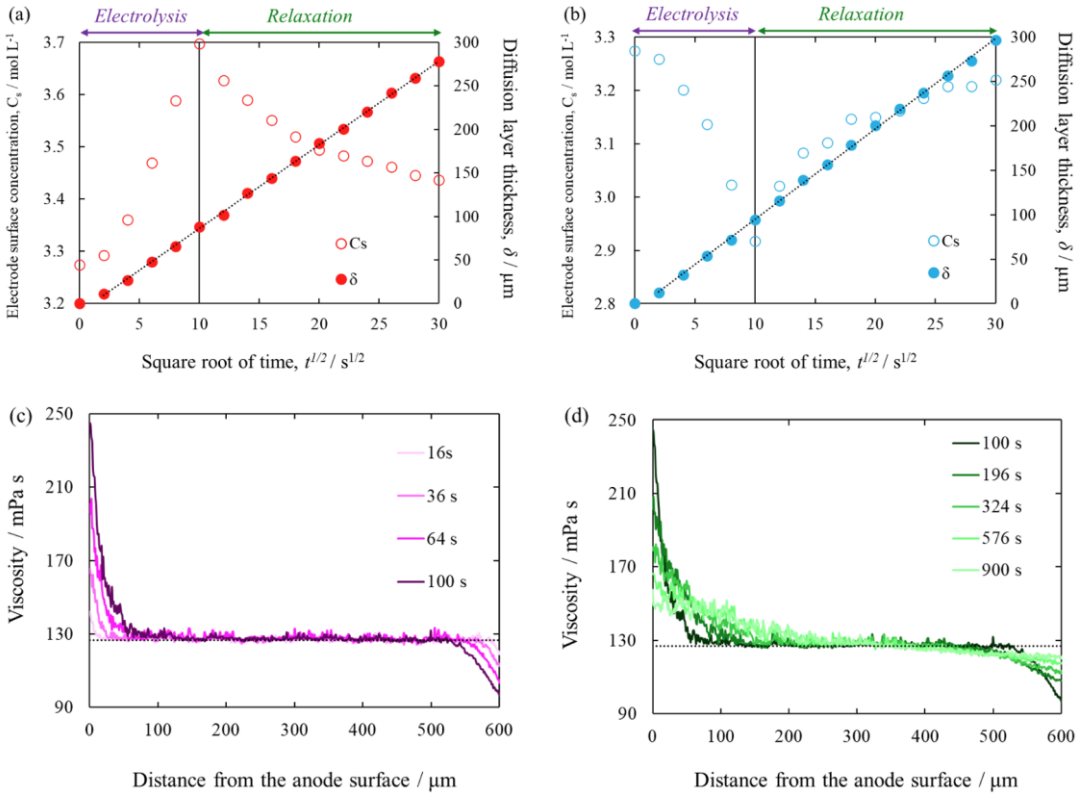

Figure 4. Temporal variations in the electrode surface concentration (open circle) and diffusion layer thickness (closed circle) on (a) anode and (b) cathode sides. Viscosity profiles (c) during and (d) after electrolysis. Electrolyte viscosity was calculated from the curve in Figure 2(a).

Figure 4(a) shows the variation in *C*s and δ near the anode as a function of the square root of time ($t^{1/2}$). The changes in *C*s and δ were slow in the first 4 s after starting electrolysis. At this time, surface films and impurities that covered the anode surface before the experiment may have been removed [24]. Subsequently, *C*s and δ changed proportionally with $t^{1/2}$. The current was stopped at 100 s, after which *C*s gradually decreased, reaching 3.44 mol L^{-1} at 900 s. Conversely, δ continued to increase at the same rate as that during electrolysis. Figure 4(b) shows changes in *C*s and δ near the cathode as a function of $t^{1/2}$. *C*s decreased, and δ increased proportionally with $t^{1/2}$ after the

completion of initial side reactions at the cathode surface. Upon stopping the current, *C*s gradually increased to the bulk concentration, reaching 3.22 mol L^{-1} at 900 s. In this manner, *C*s on the anode and cathode changed by -0.25 and +0.31 mol L^{-1}, respectively, after electrolysis. The relaxation of the asymmetric CG near both electrodes can also be observed from the changes in *C*s. In addition, δ increased during electrolysis on the cathode side at the same rate as that on the anode side. Therefore, diffusion dominates the mass transfer of Li^+ near both electrodes during and after electrolysis.

Eq. (4) was used to estimate the Li^+ diffusion coefficients near the anode and cathode:

$$C_s = C_0 \pm \frac{2i(1-t^*)}{z\mathrm{F}\sqrt{D}}\sqrt{\frac{t}{\pi}} \quad (4)$$

where *C*s is the concentration at the electrode surface at 100 s; C_0 is the bulk concentration; *z* is the valence; F is the Faradaic constant; *D* is the diffusion coefficient; *i* is the current density; *t** is the transference number of Li^+ (0.44 [25]); and *t* is the time (100 s). Although t^+ is a concentration-dependent parameter, we assumed it was constant for simple calculation. The anode and cathode sides exhibit a diffusion coefficient, *D*, of 2.2 × 10^{-7} and 3.0 × 10^{-7} cm^2 s^{-1}, respectively. Therefore, *D* on the cathode side was more significant than that on the anode side during electrolysis. A similar trend was observed in previous studies [11,12]. The difference in the *D* values of the two electrodes was attributed to the viscosity of the electrolyte, which may influence the asymmetry of the concentration profile. Figure 4 shows the distribution of the electrolyte viscosity (c) during and (d) after electrolysis. The viscosity was estimated from the plot of viscosity as

a function of the LiFSA/G4 molar ratio in Figure 2(a). The electrolyte exhibited a higher viscosity in the vicinity of the anode than near the cathode. An inversely proportional relationship is typically observed between the diffusion coefficient of ions and electrolyte concentration [26,27]. Accordingly, a significant difference was observed in the diffusivity of the ions near the anode and cathode. This viscosity effect induces an asymmetric concentration profile, which becomes increasingly asymmetric with increasing electrolysis time. Mass transport is dominated by diffusion both during and after electrolysis. Hence, the difference in diffusivity arising from the viscosity may have affected the CG relaxation process, further increasing the asymmetry of the concentration profile. A similar phenomenon was observed by Wang et al. using a highly concentrated $LiPF_6$–EMC electrolyte [17]. This is in good agreement with our experimental results and explains the observed differences in the diffusion phenomena resulting from the differences in viscosity.

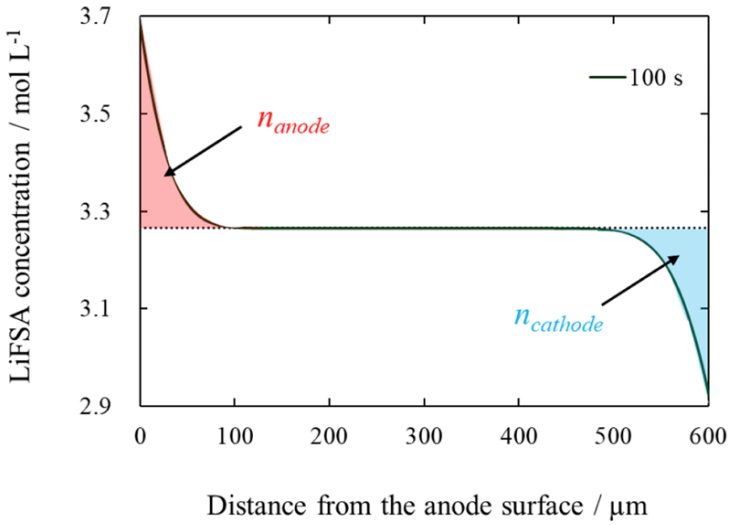

Figure 5. Profile in the molar amount of LiFSA near the anode (red) and cathode (blue) after 100 s electrolysis. (For interpretation of the references to color in this figure legend, the reader is referred to the web version of this article.)

The molar amount of LiFSA change near the anode (0-200 μm) and cathode (400-600 μm) was calculated using the concentration profile at 100 s. First, the change in the molar amount of LiFSA from the initial concentration was calculated near the anode (n_{anode}, red) and the cathode ($n_{cathode}$, light blue), respectively. Then, the concentration change on the anode side (Δn_{anode}) and cathode one ($\Delta n_{cathode}$) was obtained by multiplying the cross-sectional area of the experimental cell (200 μm × 15 mm). Consequently, Δn_{anode} and $\Delta n_{cathode}$ were 3.07×10^{-8} and 3.17×10^{-8} mol, which were almost the same. This calculation indicates that the mass balance in the electrolyte was maintained during electrolysis.

3.4 Conclusions

In this study, the concentration profile between an anode and cathode with an interelectrode distance of 600 μm was observed in situ during and after electrolysis in a LiFSA–G4 SIL using DHM. The estimation of the diffusion coefficients near the anode and cathode revealed differences in diffusivity, which were attributed to the significant changes in the viscosity of the electrolyte between the electrodes, which may have resulted in a difference in the degree of relaxation of the CG. In future studies, the correlation between Li^+ diffusion phenomena and Li deposition morphology in SILs can be elucidated using the microscale interelectrode experimental cell demonstrated in this study, and the mechanisms of deposition on the cathode surface and mass transport near the anode can be determined. An understanding of these mechanisms will facilitate the application of Li metal electrodes in next-generation rechargeable batteries.

References

[1] G. E. Blomgren, *J. Electrochem. Soc.* **2017**, *164*, A5019–A5025.

[2] H. Wang, C.-J. Yao, H.-J. Nie, K.-Z. Wang, Y.-W. Zhong, P. Chen, S. Mei, Q. Zhang, *Journal of Materials Chemistry A* **2020**, *8*, 11906–11922.

[3] F. Wu, J. Maier, Y. Yu, *Chemical Society Reviews* **2020**, *49*, 1569–1614.

[4] H. Kim, W. Choi, J. Yoon, J. H. Um, W. Lee, J. Kim, J. Cabana, W.-S. Yoon, *Chemical Reviews* **2020**, *120*, 6934–6976.

[5] T. Tamura, K. Yoshida, T. Hachida, M. Tsuchiya, M. Nakamura, Y. Kazue, N. Tachikawa, K. Dokko, M. Watanabe, *Chemistry letters* **2010**, *39*, 753–755.

[6] T. Mandai, K. Yoshida, K. Ueno, K. Dokko, M. Watanabe, *Physical chemistry chemical physics* **2014**, *16*, 8761–8772.

[7] N. N. Rajput, T. J. Seguin, B. M. Wood, X. Qu, K. A. Persson, *Modeling Electrochemical Energy Storage at the Atomic Scale* **2018**, 79–124.

[8] L. Cheng, L. A. Curtiss, K. R. Zavadil, A. A. Gewirth, Y. Shao, K. G. Gallagher, *ACS Energy Letters* **2016**, *1*, 503–509.

[9] H. Wang, M. Matsui, H. Kuwata, H. Sonoki, Y. Matsuda, X. Shang, Y. Takeda, O. Yamamoto, N. Imanishi, *Nature communications* **2017**, *8*, 1–9.

[10] K. Nishikawa, T. Mori, T. Nishida, Y. Fukunaka, M. Rosso, *Journal of electroanalytical chemistry* **2011**, *661*, 84–89.

[11] A. Miki, K. Nishikawa, G. Kamesui, H. Matsushima, M. Ueda, M. Rosso, *Journal of Materials Chemistry A* **2021**, *9*, 14700–14709.

[12] G. Kamesui, K. Nishikawa, M. Ueda, H. Matsushima, *ACS Energy Letters* **2022**, *7*, 4089–4097.

[13] Z. Chen, D. L. Danilov, R.-A. Eichel, P. H. Notten, *Energy Storage Materials* **2022**,

48, 475–486.

[14] J. Fawdon, J. Ihli, F. L. Mantia, M. Pasta, *Nature Communications* **2021**, *12*, 1–9.

[15] J. K. Utterback, A. J. King, L. Belman-Wells, D. M. Larson, L. M. Hamerlynck, A. Z. Weber, N. S. Ginsberg, *ACS Energy Lett.* **2023**, 1785–1792.

[16] T. F. Fuller, M. Doyle, J. Newman, *Journal of the Electrochemical Society* **1994**, *141*, 982.

[17] A. A. Wang, A. B. Gunnarsdóttir, J. Fawdon, M. Pasta, C. P. Grey, C. W. Monroe, *ACS energy letters* **2021**, *6*, 3086–3095.

[18] M. Klett, M. Giesecke, A. Nyman, F. Hallberg, R. W. Lindström, G. Lindbergh, I. Furó, *Journal of the American Chemical Society* **2012**, *134*, 14654–14657.

[19] D. Takamatsu, A. Yoneyama, Y. Asari, T. Hirano, *Journal of the American Chemical Society* **2018**, *140*, 1608–1611.

[20] F. R. McLarnon, R. H. Muller, C. W. Tobias, *JOSA* **1975**, *65*, 1011–1018.

[21] F. R. McLarnon, R. H. Muller, C. W. Tobias, *Electrochimica Acta* **1976**, *21*, 101–105.

[22] A. Miki, K. Nishikawa, T. Ozawa, H. Matsushima, M. Ueda, *Journal of The Electrochemical Society* **2020**, *167*, 062501.

[23] G. Kamesui, K. Nishikawa, H. Matsushima, M. Ueda, *Journal of The Electrochemical Society* **2021**, *168*, 031507.

[24] K. Nishikawa, Y. Fukunaka, T. Sakka, Y. H. Ogata, J. R. Selman, *Journal of The Electrochemical Society* **2007**, *154*, A943.

[25] K. Ueno, K. Yoshida, M. Tsuchiya, N. Tachikawa, K. Dokko, M. Watanabe, *J. Phys. Chem. B* **2012**, *116*, 11323–11331.

[26] K. Yoshida, M. Tsuchiya, N. Tachikawa, K. Dokko, M. Watanabe, *The Journal of*

Physical Chemistry C **2011**, *115*, 18384–18394.

[27] J. Newman, K. E. Thomas-Alyea, *Electrochemical Systems*, John Wiley & Sons, **2012**.

Chapter 4: Elucidation of Mass Transport Phenomena in Highly Concentrated Electrolytes during Current Cycling Using In-Situ Interferometry and Finite Difference Method

4.1 Introduction

Lithium-ion batteries (LIBs) exhibit high energy densities, owing to which they are widely utilized in various devices, such as smartphones and laptops. As the demand for smart grids powered by renewable energy and electric vehicles (EVs) continues to grow, developing suitable storage batteries has become crucial. Previous studies have shown that LIBs have nearly reached their theoretical capacity.[1–4] Hence, LIBs with higher energy densities should be developed. Moreover, the development of high-speed charge–discharge properties is necessary for the efficient operation of EVs. A key factor influencing the charge–discharge rate of storage batteries is the cation transference number of the electrolyte (t^+).[5] The higher t^+ is, the lower the concentration polarization of the electrolyte becomes, which enables faster charge–discharge reactions. Therefore, it is crucial to explore and identify electrolytes with high t^+.

One approach to increasing the energy density involves increasing the electrolyte concentration. In 2010, Watanabe et al. discovered that an equimolar mixture of Li salt and glyme solvent showcased a wide potential window and strong resistance to thermal decomposition, which was attributed to the chelating effect.[6] This solution exhibited similar properties to those of ionic liquids and was named a solvate ionic liquid (SIL).[7] In 2014, Yamada et al. and Sodeyama et al. observed that ultra-high-concentration acetonitrile electrolytes over 4 mol L^{-1} exhibited significantly higher resistance to reductive decomposition than commercial electrolytes of approximately 1 mol L^{-1}.[8,9] Highly concentrated electrolytes (HCEs), including SIL, have a unique solvation structure in which almost all solvent molecules are coordinated to cations. This structure enables the HCE to achieve operating voltages in the 4–5 V range,[10] thereby increasing the battery's energy density. Notably, HCEs also exhibit high t^+.[11,12] Typically, a tradeoff

exists between the t^+ value and the ionic conductivity of the electrolyte. However, the cations in a HCE are transported via a hopping mechanism between salt-solvent clusters, resulting in high ionic conductivity despite their high viscosity.[13]

Metallic Li has the lowest density (0.534 g cm^{-3}) and the most negative electrode potential (-3.04 V vs. standard hydrogen electrode) among all metals.[14] Additionally, it exhibits a significantly high theoretical capacity of 3860 mAh g^{-1}, making it an ideal candidate for enhancing the energy density of batteries.[15] Li-sulfur batteries[16] and Li-air batteries[17] have also been developed with metallic Li as the negative electrode. However, whisker- or dendrite-like Li deposits appeared on the electrodes during the charge (electrodeposition) and discharge (electrochemical dissolution) reactions. These sharp Li deposits may pierce the separator within the battery, resulting in potential short circuits and ignition accidents. Therefore, the practical application of Li metal as a negative electrode has not yet been achieved.

Mass transport in electrolytes during electrochemical reactions relies on three mechanisms: diffusion, migration, and convection.[18] When an electrochemical reaction is initiated, the concentration of metal ions near the electrode changes, creating a concentration gradient that drives the diffusion of the ionic species.[19] Electrolysis forms a potential gradient between the electrodes in the electrolyte, causing anions to migrate toward the anode and cations toward the cathode.[20] Additionally, the density difference between the bulk and electrolyte close to the electrode triggers natural convection, further enhancing mass transport.[21] Transporting metal ions from the bulk to the cathode surface is vital for understanding metal electrodeposition.[22] The rate of Li electrolysis in organic electrolytes is significantly influenced by Li^+ transport near the cathode.[23,24] An inadequate Li^+ supply to the cathode surface leads to Li^+ depletion, resulting in an uneven

morphology of Li deposition. Hence, understanding the Li^+ transport mechanism in the electrolyte is vital for controlling the morphology of Li deposition. Furthermore, we previously reported that the Li^+ diffusion from the anode surface to the bulk in sulfolane-based HCE governs the electrolysis speed at 5 mA cm^{-2}.[25] Consequently, a thorough understanding of the Li^+ mass transfer in electrolytes near both electrodes is essential for applying Li electrodes and HCE in storage batteries.[26,27] However, thus far, such investigations have focused on charging processes, specifically related to Li electrodeposition.[25,28–34] In actual rechargeable batteries, discharging occurs after charging. During discharging, Li^+ ions move in the opposite direction to that during charging, potentially affecting the Li deposition-dissolution mechanism. Therefore, understanding electrolyte mass transfer during current cycling is crucial to controlling Li deposition's morphology.

We previously used in situ laser interferometry to observe the concentration distribution near an electrode during electrochemical reactions using lithium bis(trifluoromethanesulfonyl)amide or lithium bis(fluorosulfonyl)amide (LiFSA) and tetraglyme (G4) SILs.[19,31] Laser interferometry, a technique first employed by McLarnon et al. in the 1970s,[35,36] has been widely adopted in numerous studies.[25,31,37–41] Interferometers can detect changes in the refractive indices of the electrolytes. In the case of a solute-solvent binary electrolyte, the refractive index directly corresponds to the concentration of the solute. Hence, information regarding the change in electrolyte concentration can be obtained by detecting changes in the refractive index.

In this study, the concentration changes in a highly concentrated electrolyte (an equimolar mixture of LiFSA and G4) between the Li electrodes were observed using in situ laser interferometry under current reversal and re-reversal. The Li^+ transference

number and LiFSA diffusion coefficient were obtained from the concentration profiles using the pseudo-Hittorf method. Raman spectroscopy determined the relationship between the Li^+ solvation structure and the transference number. The concentration distribution during electrolysis was simulated using a one-dimensional unsteady diffusion equation to validate the concentration profiles obtained using interferometry. Furthermore, the approximate concentration profiles during current reversal and re-reversal were estimated using the finite difference method (FDM)[42,43] to verify the results obtained by interferometry.

4.2 Experimental

Schematics of an overview and cross-sectional view of the experimental cell are presented in Figures 1(a) and 1(b), respectively. Note that the electrode that was the anode during electrolysis is denoted as Electrode A and the one that was the cathode as Electrode B. The entire setup, including the experimental cell and electrolyte, was prepared in a dry room with a dew point below -50 ºC. The anode and cathode were Li foil (99.9%, Honjo Metal, Japan). The reaction area of both electrodes was 200 μm (length) × 15 mm (width). To create the electrolyte, a mixture of LiFSA (99.9%, Nippon Shokubai Co., Ltd.) and G4 (98%, Kishida Chemical Co., Ltd.) in varying molar ratios was used. This mixture was placed on a hot plate at 50 °C overnight to ensure complete dissolution. The relationship between the LiFSA: G4 molar ratio and LiFSA concentration is shown in Table 1. For the current collector, a 5 μm thick Cu foil was employed. During the assembly of the experimental cell, the current collector was placed on a glass slide, and the Li electrode was positioned on top of it. The electrode surfaces were arranged in a quasi-two-dimensional configuration with parallel orientation to minimize the effect of natural convection. The inter-electrode distance between the two electrodes was maintained at 600 μm. Subsequently, a 15 mm wide glass slide was placed over both electrodes and secured with epoxy resin along its edges. The electrolyte was injected between both electrodes. The electrochemical experiment was started after sealing the inlet to prevent contact with air.

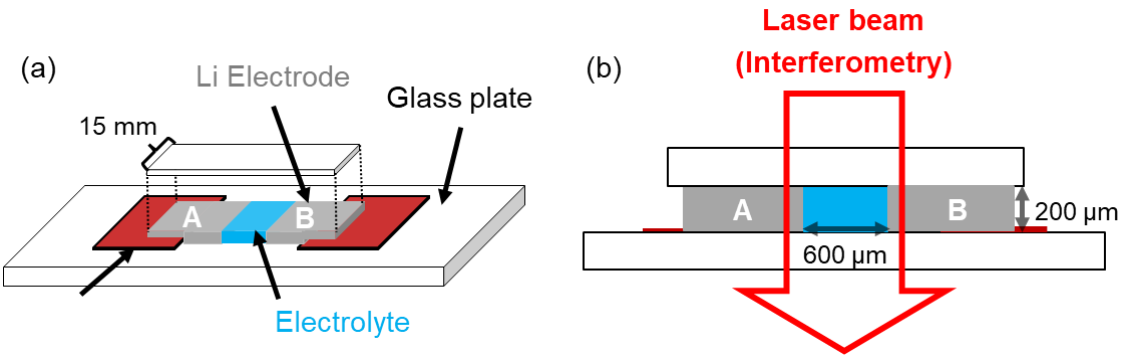

Figure 1. Schematic of the (a) overview and (b) cross-sectional view of the experimental cell.

Table 1. Relationship between LiFSA : G4 molar ratio and LiFSA concentration in the electrolyte.

LiFSA: G4 molar ratio, $M_{LiFSA/G4}$/mol mol^{-1}	LiFSA concentration, C_e/mol l^{-1}
0.6: 1	2.23
0.7: 1	2.52
0.8: 1	2.78
0.85: 1	2.91
0.9: 1	3.03
1.0: 1	3.27
1.1: 1	3.48
1.15: 1	3.59
1.2: 1	3.69
1.3: 1	3.89
1.4: 1	4.08
1.5: 1	4.26

All experiments were conducted at room temperature (23 °C). The refractive index and density of the electrolyte were obtained from a previous study [19]. Current application was performed using a potentiostat (HZ-Pro S12, Hokuto Denko, Japan). The current density was set to 3 mA cm^{-2} and was applied to the experimental cell in different directions every 100 s. The correspondence between the current application's direction

and the electrode type is shown in Table 2.

Table 2. Relationship between the direction of current application and the type of electrodes.

	Electrolysis (0–100 s)	Current reversal (100–200 s)	Current re-reversal (200–300 s)
Electrode A	Anode	Cathode	Anode
Electrode B	Cathode	Anode	Cathode

A digital holographic interferometer (DHM T1000, Lyncée Tec, Switzerland) was employed to monitor the change in the concentration distribution of LiFSA in the electrolyte between the two electrodes during current application. The laser light had a wavelength of 683.6 nm. The optical path length was 200 μm, which was consistent with the electrode thickness. Holograms obtained by DHM were analyzed using Koala software (Lyncée Tec) to calculate concentration profiles [25,31,41]. The refractive index of the electrolyte is proportional to the concentration;

$$\Delta n = \left(\frac{\partial n}{\partial C}\right)\Delta C \tag{1}$$

where Δn is the change in refractive index, and ΔC is the change in LiFSA concentration. The interference equation can be expressed as in Eq. 2;

$$d\Delta n = \left(\frac{\Delta\theta}{2\pi}\right)\lambda \tag{2}$$

where d is the optical path length, $\Delta\theta$ is the phase change of the electrolyte, and λ is the wavelength of the laser light. From Eqs. 1 and 2, we obtain Eq. 3;

$$\Delta C = \left(\frac{\partial C}{\partial n}\right)\left(\frac{\Delta\theta}{2\pi}\right)\left(\frac{\lambda}{d}\right) \tag{3}$$

If the interferometer observes the electrolyte and detects $\Delta\theta$ during electrolysis, the ΔC associated with Li electrodeposition/-chemical dissolution can be calculated.

The Raman spectra of the electrolyte were measured with a laser micro-Raman spectrometer (LabRAM 1B, HORIBA, Japan). The wavelength of the excitation laser was 632.7 nm. The resolution of the spectrometer was about 1 cm^{-1}. The exposure time and cumulative exposures were 15 s and 4 times, respectively.

4.3 Results and Discussions

Electrolysis

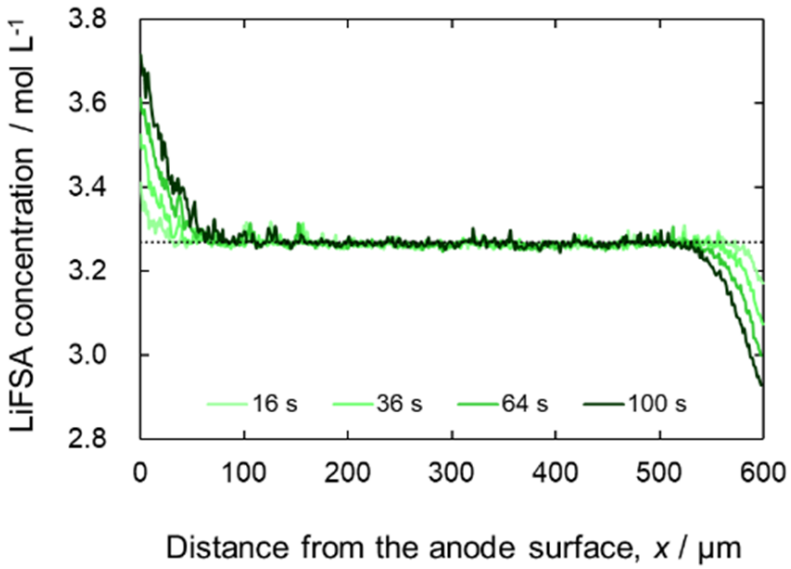

Figure 2. Concentration profile of lithium bis(fluorosulfonyl)amide (LiFSA) during electrolysis in an equimolar mixture of LiFSA and tetraglyme (LiFSA-G4) electrolytes.

Figure 2 shows the changes in the concentration of LiFSA in the LiFSA-G4 equimolar electrolyte during electrolysis. The horizontal dotted line represents the initial LiFSA concentration in the electrolyte (C_e = 3.27 mol L^{-1}). During electrolysis, the LiFSA concentration at the anode surface increased and reached 3.69 mol L^{-1} after 100 s. This concentration increase formed a negative concentration gradient near the anodes. Consequently, the diffusion layer, which is more concentrated than the bulk, became thicker. In contrast, LiFSA concentration at the cathode surface decreased during electrolysis, reaching 2.90 mol L^{-1} after 100 s. This concentration change created a negative concentration gradient near the cathode, expanding the thickness of diffusion layer with a lower concentration than the bulk. Figure. S2 shows the concentration

profiles at (a) C_e = 2.52 and (b) 3.89 mol L^{-1}. In both cases, the LiFSA concentration near the anode increased, and that near the cathode decreased as the electrolysis proceeded over time.

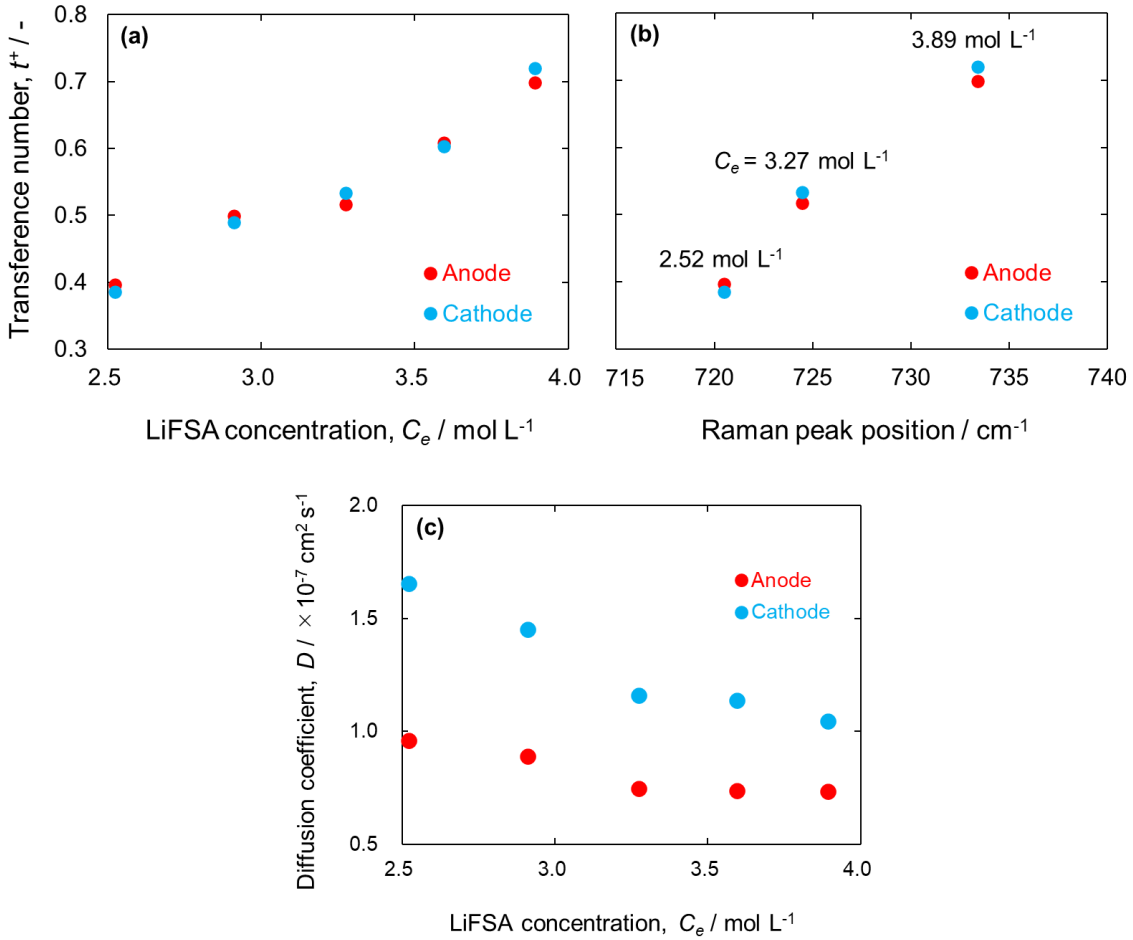

Figure 3. (a) Li^+ transference number near the anode and cathode; (b) relationship between Raman peak position and Li^+ transference number; and (c) diffusion coefficient near the anode and cathode at various electrolyte concentrations.

Figures. S3(a) and S3(b) show the Raman spectra of the LiFSA powder, G4, and solutions with various LiFSA concentrations at 700–800 cm^{-1}. Fujii et al. and Yoon et al. reported that S–N–S stretching vibrations of uncoordinated FSA^- appear at 720–730 cm^-

^{1}.[44,45] The peaks in the spectra shifted toward higher wavenumbers as C_e increased, suggesting the increase in the number of contact ion pairs (CIPs) and aggregates (AGGs) at Li^+ and FSA^-.[46] Figures S3(c) and S3(d) show the Raman spectra of the LiFSA powder, G4, and solutions with various LiFSA compositions at 800–900 cm^{-1}. Grondin et al. reported that the C–O stretching and CH_2 locking vibrations of G4 appear at 800–900 cm^{-1}.[47] The peak intensity at 870 cm^{-1} increased for $C_e \leq 3.27$ mol L^{-1}, reaching maximum intensity at $C_e = 3.27$ mol L^{-1}. This suggests that the proportion of G4 solvated with Li^+ in solution increases with increasing C_e. In contrast, the peak intensity decreased for $C_e \geq$ 3.27 mol L^{-1}. The differences in peak positions and peak intensities of the spectra across various C_es are consistent with the previous work by Terada et al.[48] Tsuzuki et al. reported that the energy level of the highest occupied molecular orbital of G4 was elevated in the cation-G4-TFSA complex compared to the cation-G4 complex.[49] Consequently, an excess of LiFSA can influence the formation of complexes between Li^+ and G4.[31]

The concentration profiles after 100 s were integrated against the x-axis to calculate the change in the LiFSA concentration from that before electrolysis (denoted by α) near each electrode. α was then used to determine t^+ using the pseudo-Hittorf method (see Supporting Information S2). Figure 3(a) shows t^+ values for electrolytes with different C_e. t^+ increased with increasing C_e. This tendency is consistent with the results of Fawdon et al., who measured the t^+ values of LiFSA-G4 solutions below 2 mol L^{-1}.[50] Li^+ was solvated by G4 at low C_e, thereby increasing the Stokes radius. However, FSA^- has weak interactions with Li^+, resulting in a smaller Stokes radius and higher mobility than Li^+. CIPs and AGGs were formed in the solution with increasing C_e (Figure 3(b)). These complexes decrease the mobility of FSA^- with Li^+,[51] thus increasing t^+ as C_e increases. Typically, the partial molar volume of the solute (V_e) increases with increasing

solute concentration in the electrolyte.[32,50] However, increased cation-G4-FSA complexation due to increasing C_e would compress LiFSA, thus decreasing V_e (Figure. S1(c)). Terada and Ueno et al. have previously measured t^+ of Li^+ in an equimolar mixture of LiFSA-G4 using pulsed-gradient spin-echo nuclear magnetic resonance spectroscopy (PGSE-NMR), obtaining a value of 0.44.[48,52] This value does not significantly deviate from the range of 0.51-0.53 that we obtained through pseudo-Hittorf experiments.

Figure 3(c) shows the C_e dependency of the apparent LiFSA diffusion coefficient (D), as determined by Eqs. S9 and S10. D decreased with increasing C_e. Typically, an inversely proportional relationship exists between the electrolyte viscosity and the diffusion coefficient.[18] We observed that the viscosity of the electrolyte increased with increasing C_e,[19] which explains the decrease in D. Furthermore, D was more significant at the cathode than at the anode, which is the same as the results of our previous studies.[19,25,31] During electrolysis, the LiFSA concentration increases near the anode and decreases near the cathode. Consequently, the electrolyte near the anode exhibits a higher viscosity than that near the cathode, resulting in a difference in D between the two electrodes.

Terada et al. have previously reported the self-diffusion coefficient (D_{self}) of each species in electrolytes, comprising various ratios of LiFSA and G4, using pulsed field gradient-NMR.[48] They observed a decrease in D_{self} for all chemical species as C_e increased. The D_{self} for Li^+ and FSA^- were approximately close to the Ds we calculated. Furthermore, for $M_{LiFSA/G4} > 1$, the D_{self} of FSA^- becomes 2-5 times greater than that of Li^+. However, the single-wavelength interferometry method we used could only observe the transport phenomena of a single component, preventing us from discerning the differences in diffusion coefficients among ion species.

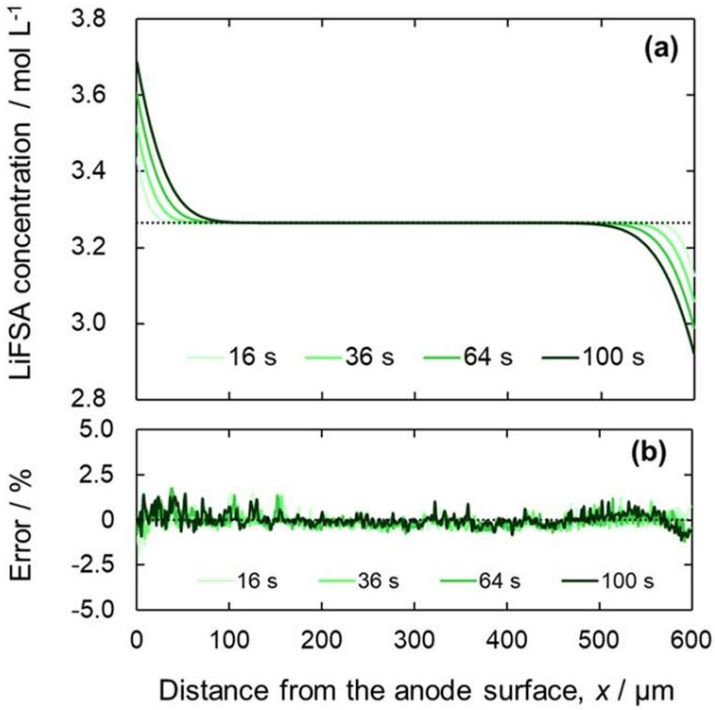

Figure 4. (a) Theoretically calculated concentration profile of LiFSA in LiFSA-G4 equimolar electrolyte during electrolysis and (b) error between the measured and theoretical concentration profiles.

Figure 4(a) shows the theoretically calculated concentration profile of LiFSA-G4 equimolar electrolytes during electrolysis. The changes in the concentration profile every 1 s are shown in Figure S5(a). Eqs. 4 (anode) and 5 (cathode), derived from the Laplace transform of Fick's second law, were employed to calculate the theoretical concentration profiles;

$$C(x,t) = C_e + \frac{i(1-t^+)}{zFD}(1 - C_e V_e)\left[2\sqrt{\frac{Dt}{\pi}}exp\left(-\frac{x^2}{4Dt}\right) - x\,erfc\left(\frac{x}{\sqrt{4Dt}}\right)\right] \quad (4)$$

$$C(x,t) = C_e - \frac{i(1-t^+)}{zFD}(1 - C_e V_e)\left[2\sqrt{\frac{Dt}{\pi}}\, exp\left(-\frac{(L-x)^2}{4Dt}\right) - x\, erfc\left(\frac{L-x}{\sqrt{4Dt}}\right)\right] \quad (5)$$

where C is the LiFSA concentration in the electrolyte, x is the distance from the anode surface, t is the time, z is the valence, F is the Faraday constant, i is the current density, V_e is the partial molar volume of LiFSA, and L is the inter-electrode distance (for the derivation of the equation, see Supporting Information S1). The error between the concentration profile obtained via interferometry and the theoretical value is shown in Figure 4(b). The maximum divergence is 1.8 %. These results validate the electrolyte concentration profiles measured using interferometry.

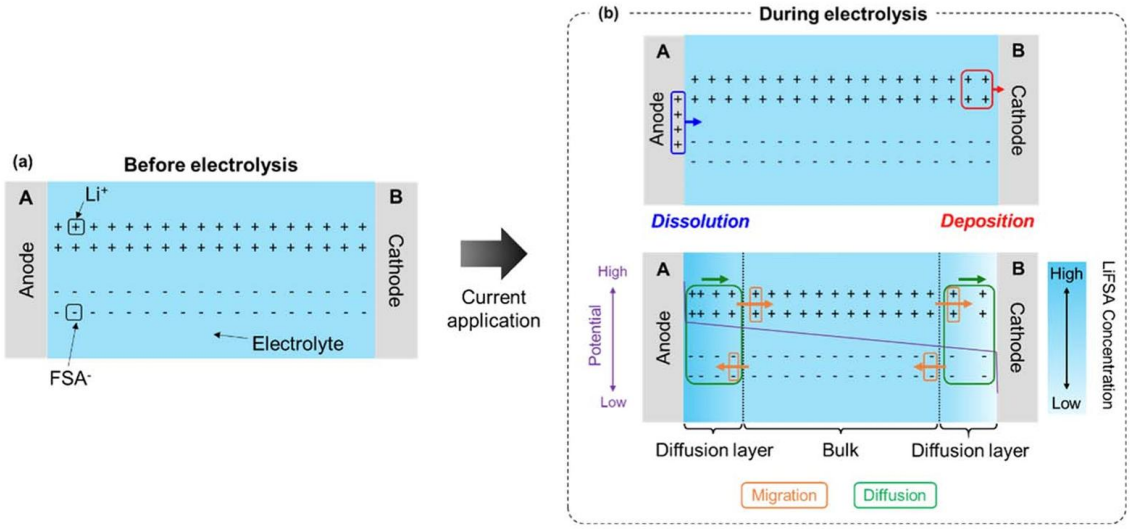

Figure 5. Schematics of the ion movement (a) before and (b) during electrolysis in LiFSA-G4 equimolar electrolyte.

Figure 5 shows the ion movement in LiFSA-G4 equimolar electrolytes before and during electrolysis. The dotted line represents the concentration boundary between

the diffusion layer and the bulk. Before the electrolysis, the ions are uniformly distributed in the electrolyte. However, Li^+ moves from the anode surface to the electrolyte during electrolysis and is consumed at the cathode surface. Moreover, Li^+ and FSA^- migrate in the presence of an excess positive charge near the cathode to maintain the macroscopic electroneutrality of the electrolyte. As $t^+ \approx 0.5$ at C_e = 3.27 mol L^{-1}, Li^+ and FSA^- migrate in equal numbers—similarly, excess negative charge at the cathode surface results in ion migration to maintain electrical neutrality. Hence, ion migration balances the charges at both electrodes, increasing or decreasing the ion concentration in the electrolyte at the anode and cathode compared to that in the bulk. Finally, LiFSA diffuses owing to the concentration difference between the two electrode surfaces and the bulk. Figures S2(c) and S2(d) show the ion movement in electrolytes during electrolysis at C_e < 3.27 and C_e > 3.27 mol L^{-1}. For C_e < 3.27 mol L^{-1}, FSA^- migrated more than Li^+ as t^+ < 0.5, whereas for C_e > 3.27 mol L^{-1}, Li^+ migrated more than FSA^- as t^+ > 0.5.

Current reversal

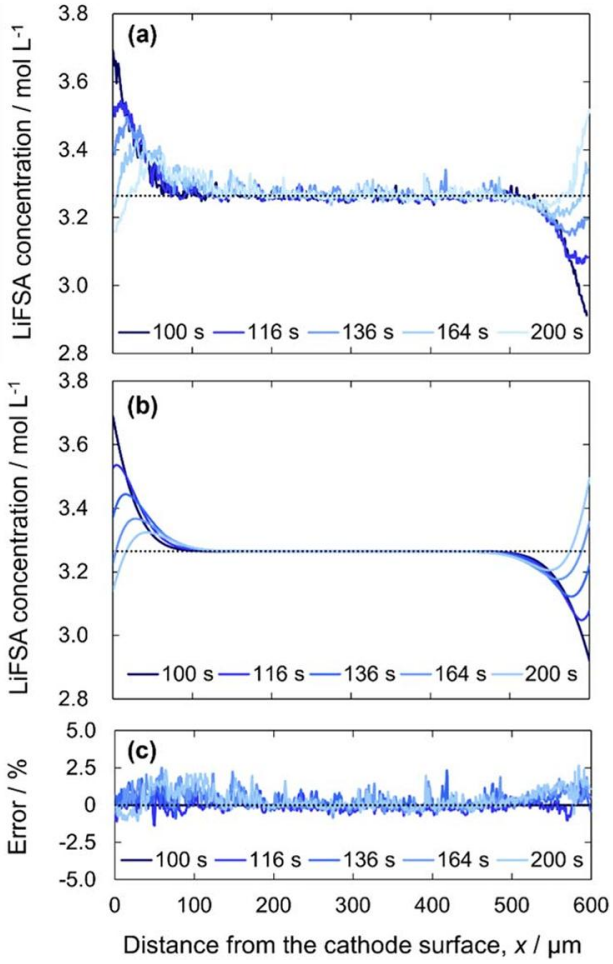

Figure 6. LiFSA concentration profile in LiFSA-G4 equimolar electrolyte during current reversal obtained by (a) interferometry and (b) finite difference method (FDM); (c) error between the concentration profiles of interferometry and FDM

Figure 6(a) shows the LiFSA concentration profiles in the LiFSA-G4 equimolar electrolyte at reversed applied current. The legends indicate the time elapsed since the beginning of electrolysis. The current reversal exchanged the anode and cathode for electrolysis. The Li concentration on the cathode surface, which had been higher than the bulk, decreased during electrodeposition, reaching 3.16 mol L^{-1} after 200 s. An upward

convex concentration gradient formed near the cathode owing to the change in the Li concentration at the cathode surface; after 200 s, a positive concentration gradient was observed at 0–50 μm from the cathode surface and a negative gradient at 50–120 μm. In contrast, at the anode, where the concentration had been lower than the bulk, the electrodeposition increased with Li dissolution, reaching 3.51 mol L^{-1} after 200 s. This change resulted in a downward convex concentration gradient at the anode, in contrast to that near the cathode. After 200 s, a negative concentration gradient was observed at 470–550 μm from the cathode surface and a positive gradient at 550–600 μm. Figure 6(b) shows the FDM Li concentration profiles in a LiFSA-G4 equimolar electrolyte during current reversal (see Supporting Information S4). The FDM-estimated concentration changes for every 1 s are shown in Figure S5(b). Almost symmetrical upward and downward convex profiles are observed. After 200 s, the inflection point of the concentration gradient was identified at nearly the same position as that obtained via interferometry. Figure 6(c) shows the error between the concentration profiles obtained by interferometry and FDM. The maximum deviation was 2.5 %, confirming the validity of the concentration profile obtained by interferometry during the current reversal. This also indicates the accuracy of the interferometric measurements.

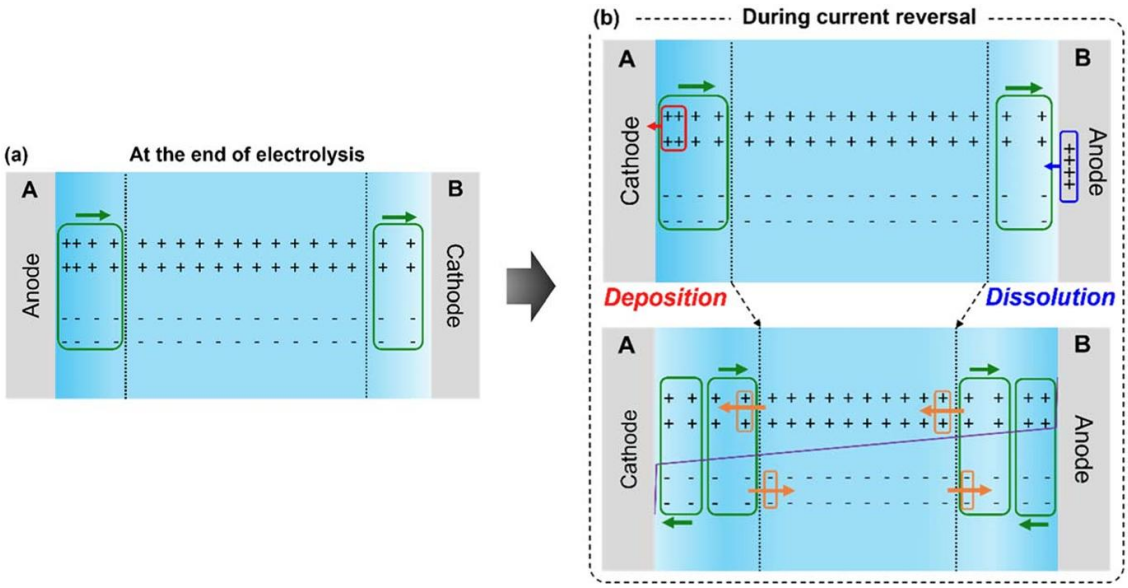

Figure 7. Schematics of ion movement in the electrolyte (d) before and (e) after current reversal.

Figures 7(a) and 7(b) show the ion movement in the LiFSA-G4 equimolar electrolyte before and after current reversal. We assumed that t^+ remained constant at approximately 0.5 during current cycling. The concentration gradient formed during electrolysis before current reversal was maintained until the end of the electrolysis. Therefore, Li^+ and FSA^- near both electrodes diffused from the anode to the cathode. The direction of the applied current was reversed immediately after electrolysis was complete. When an excess negative charge existed near the cathode owing to Li^+ consumption at the cathode surface, Li^+ and FSA^- migration maintained macroscopic electrical neutrality near the cathode. Subsequently, the LiFSA concentration at 0–50 μm from the cathode surface decreased, forming an upward convex concentration gradient near the cathode. In contrast, when an excess positive charge existed near the anode owing to the Li^+ supply at the anode surface, ion migration maintained electrical neutrality near the anode. Then,

the LiFSA concentration at 550–600 μm from the cathode surface increased, forming a downward convex concentration gradient near the anode.

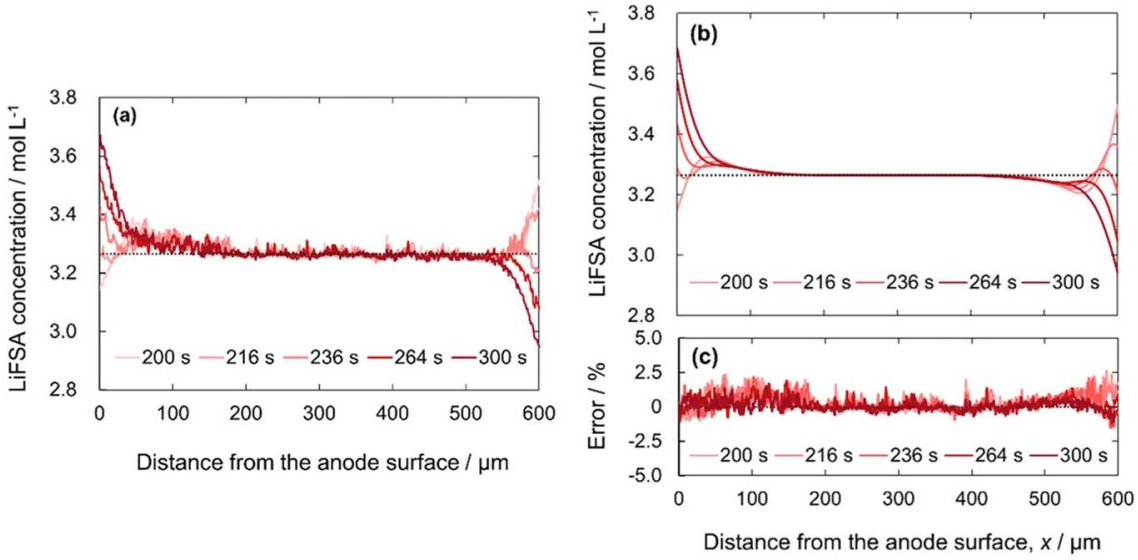

Figure 8. LiFSA concentration profile during re-reversal of the applied current in the LiFSA-G4 equimolar electrolyte obtained by (a) interferometry and (b) FDM; (c) error of concentration profiles between interferometry and FDM.

Figure 8(a) shows the concentration profile of the LiFSA-G4 equimolar electrolyte when the direction of the applied current was reversed again. The current re-reversal exchanges the anode and cathode again. The Li concentration increased at the anode and decreased at the cathode, reaching 3.67 and 2.95 mol L^{-1} after 300 s, respectively. With this change, the convex concentration gradient formed during the current reversal gradually transformed into a negative gradient. Compared to the first electrolysis step, the electrode surface concentration changed less from the bulk concentration at 300 s than at 100 s. This is because the electrode surface concentration approached the bulk concentration due to the reversal of the current before the current

reversal. Figure 8(b) shows the FDM estimate of the electrolyte concentration profile during current re-reversal. The concentration changes obtained at 1 s intervals are shown in Figure S5(c). The convex concentration gradients near both electrodes, formed by current reversal, were all unified downward, consistent with interferometry. Figure 8(c) shows the error between the concentration profiles obtained by interferometry and FDM. The maximum deviation was 2.6 %, confirming the validity of the concentration profile of the electrolyte during current re-reversal by interferometry.

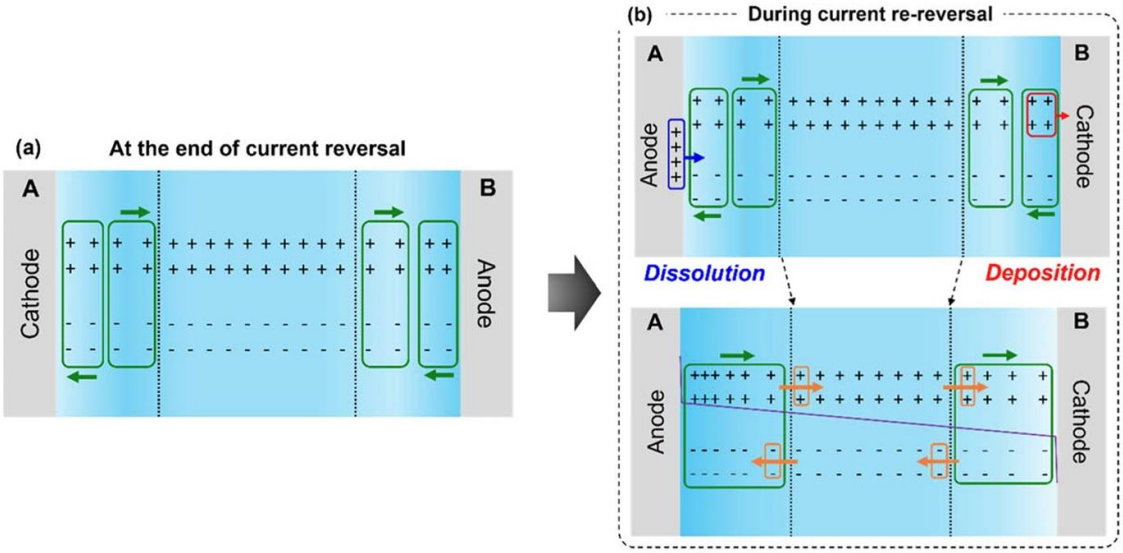

Figure 9. Schematics of ion movement in the electrolyte (a) before and (b) after current re-reversal.

Figures 9(a) and 9(b) show the ion movement in the LiFSA-G4 equimolar electrolyte before and after current re-reversal. Before the applied current direction was reversed again, the electrolyte maintained an upward and downward convex concentration gradient formed by the current reversal. Hence, two different directions of LiFSA diffusion existed near both electrodes—one approaching the anode and the other approaching the cathode. Upon reversing the direction of the applied current again, Li^+ is

supplied from the anode surface to the electrolyte because of Li dissolution. Simultaneously, Li^+ is consumed from the electrolyte on the cathode surface via Li deposition. When an excess positive charge exists near the anode and an excess negative charge exists near the cathode, the migration of ionic species maintains the electrical neutrality of the electrolyte. Hence, the LiFSA concentration increased near the anode and decreased near the cathode. Consequently, the upward and downward convex concentration gradients unified into a negative gradient during the current re-reversal.

4.4 Conclusions

In this study, we used in situ interferometry to observe the concentration profile of the electrolyte containing an equimolar mixture of lithium bis(fluorosulfonyl)amide and tetraglyme (LiFSA-G4) during current cycling. We investigated the mass transfer mechanism during electrochemical reactions. The Li^+ transference number increased with increasing electrolyte concentration because of the coordinated structure surrounding the Li^+. The LiFSA diffusion coefficient decreased with increasing electrolyte concentration due to increased viscosity. When the concentration profile was estimated using the finite difference method (FDM), the maximum percentage error between the measured and approximate values was 2.6 %. This indicates that FDM is a reliable tool for estimating the concentration profile during cycling. A thorough understanding of the mass transfer mechanism in electrolytes is crucial to enhancing the energy density of storage batteries with HCE and Li electrodes. This study represents a milestone toward realizing next-generation high-energy-density storage batteries.

4.5 Additional Experiment

S1 Simulation of concentration profiles during electrolysis

In this study, diffusion in the experimental cell during current application was assumed to be one-dimensional and non-stationary. The theoretical equation from Fick's second law was used to fit the concentration profiles acquired from interferometry. The expression for Fick's second law is given as follows [53];

$$\frac{\partial C(x,t)}{\partial t} = D\frac{\partial^2 C(x,t)}{\partial x^2} \tag{S1}$$

where C is the concentration, x is the position, t is time, and D is the diffusion coefficient. The boundary conditions were set as follows [50];

$$D(1 - C_e V_e)^{-1}\left[\frac{\partial C(x,t)}{\partial x}\right] = \frac{i(1-t^+)}{zF}\ at\ x = 0 \tag{S2}$$

$$C(x,t) = C_e\ at\ x = \infty \tag{S3}$$

$$C(x,t) = C_e\ \ at\ \ t = 0 \tag{S4}$$

where V_e is the partial molar volume of LiFSA, z is the valence, F is the Faraday constant, and i is the current density—solving Equation. S1 by Laplace transform and substituting the boundary conditions Eqs. S2-S4, the following equation gives the Li^+ concentration profile on the anode side;

$$C(x,t) = C_e + \frac{i(1-t^+)}{zFD}(1 - C_e V_e)\left[\frac{2\sqrt{Dt}}{\sqrt{\pi}} exp\left(-\frac{x^2}{4Dt}\right) - x\, erfc\left(\frac{x}{\sqrt{4Dt}}\right)\right] \quad (S5)$$

the concentration profile on the cathode side is as follows;

$$C(x,t) = C_e - \frac{i(1-t^+)}{zFD}(1 - C_e V_e)\left[\frac{2\sqrt{Dt}}{\sqrt{\pi}} exp\left(-\frac{(L-x)^2}{4Dt}\right) - x\, erfc\left(\frac{L-x}{\sqrt{4Dt}}\right)\right] (S6)$$

where L represents the inter-electrode distance of 600 μm. Eqs. S5 and S6 were used to fit the concentration profiles obtained by interferometry.

S2 Calculation of transference number and diffusion coefficient using Pseudo-Hittorf method

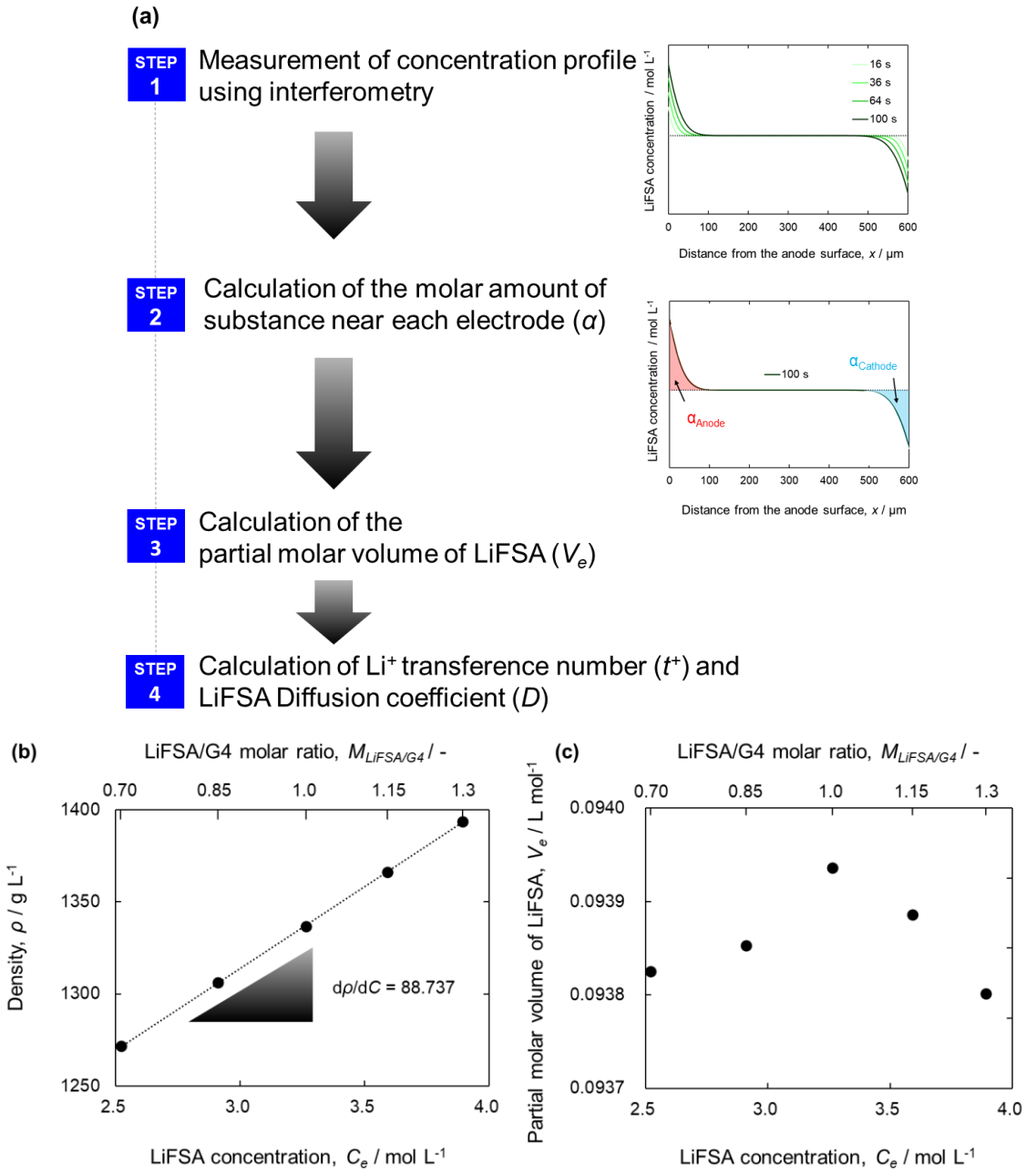

Figure S1. (a) Flow for calculating Li^+ transference number and LiFSA diffusion coefficient. Relationship between LiFSA concentration and (b) solution density or (c) partial molar volume of LiFSA.

Figure S1(a) illustrates a series of calculations for the Li^+ transference number, t^+, and the LiFSA apparent diffusion coefficient, D, based on the concentration profile. Following the approach by Fawdon et al. [50], the concentration profile after 100 s was integrated with respect to the horizontal axis, and the change in LiFSA molar amount of substance from the bulk concentration was determined near the anode (α_{anode}, depicted in red) and cathode ($\alpha_{cathode}$, shown in light blue), respectively. The concentration changes on the anode side ($\Delta\alpha_{anode}$) and the cathode side ($\Delta\alpha_{cathode}$) were then obtained by multiplying α by the cross-sectional area of the experimental cell. To obtain t^+, we employed the *Pseudo-Hittorf* method, which is a variation of the Hittorf method, widely used for determining the transference number[54]. Next, V_e was calculated using the following equation [18];

$$V_e = \frac{M_e - \frac{d\rho}{dC}}{\rho - C_e\frac{d\rho}{dC}} \quad (S7)$$

where ρ is the density, M_e is the molecular weight of LiFSA (187.07 g mol^{-1}), and $d\rho/dC$ is 88.737 g mol^{-1} (Figure S1(b)). The calculated V_e is shown in Figure. S1(c). Eq. S8 was used to calculate t^+ for various electrolyte concentrations [32];

$$t^+ = 1 - \frac{F\Delta\alpha}{Q(1 - C_eV_e)} \quad (S8)$$

where Q denotes the amount of applied electricity. Substituting $x = 0$ for Eqs. S5 and Eq. S6 yields Eqs. S9 and S10, respectively;

$$C(0,t) = C_e + \frac{2i(1-t^+)}{zF}(1 - C_e V_e)\sqrt{\frac{t}{D\pi}} \qquad (S9)$$

$$C(0,t) = C_e - \frac{2i(1-t^+)}{zF}(1 - C_e V_e)\sqrt{\frac{t}{D\pi}}\ exp\left(-\frac{L^2}{4Dt}\right) \qquad (S10)$$

In calculating D, t^+, C_e, and the electrode surface concentration at 100 s measured by interferometry were substituted into Eqs. S9 and S10.

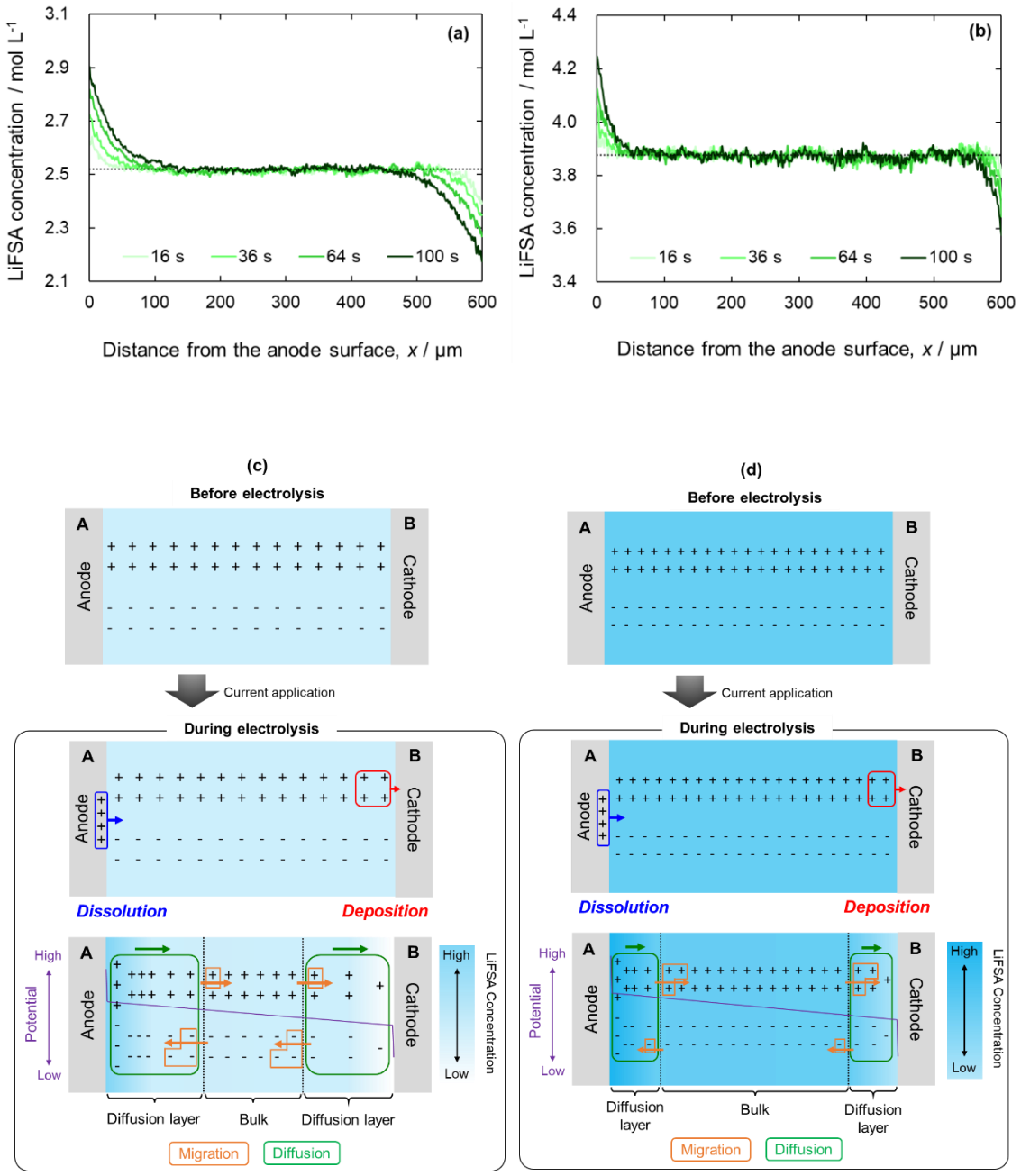

Figure S2. Transient of concentration profile during electrolysis in C_e = (a) 2.52 and (b) 3.89 mol L^{-1}, respectively. Schematics of movement on ions during electrolysis in (c) $C_e < 3.27$ and (d) $C_e > 3.27$ mol L^{-1}, respectively.

S3 Raman spectroscopy

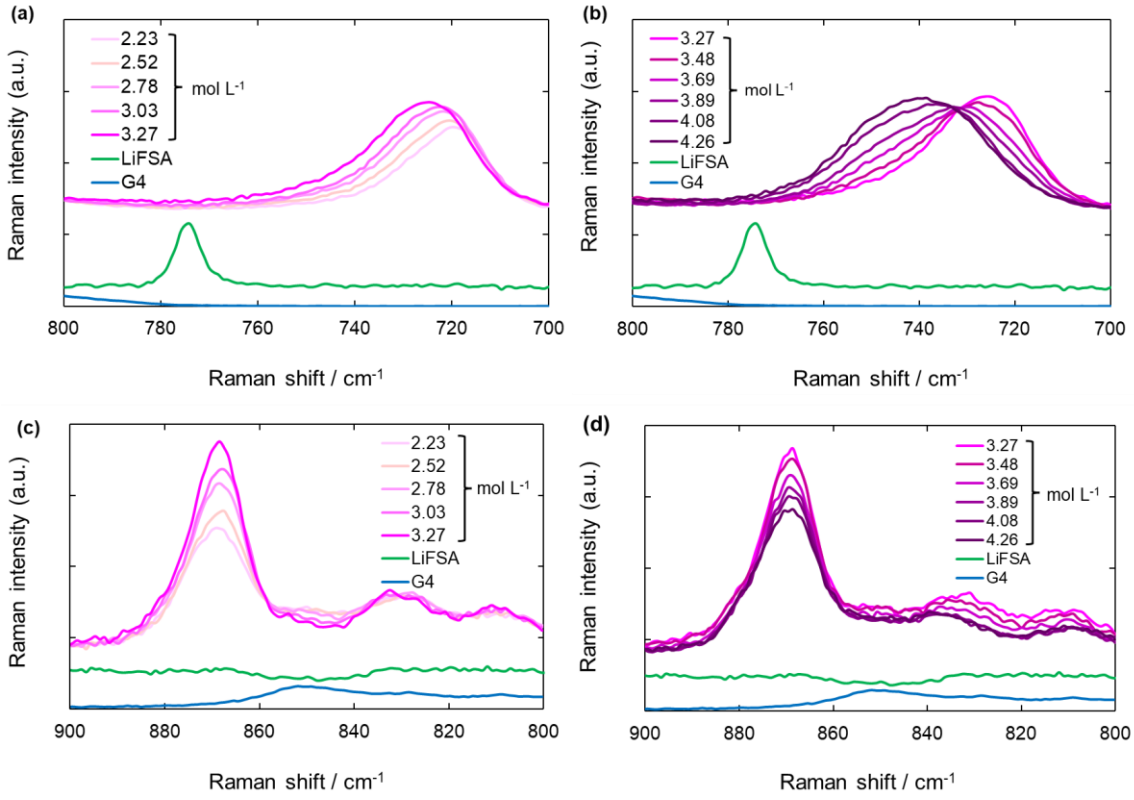

Figure S3. Raman spectra at 700- 800 cm^{-1} of LiFSA, G4 and (a) $2.23 \leq C_e \leq 3.27$ mol L^{-1} or (b) $3.27 \leq C_e \leq 4.26$ mol L^{-1}, respectively. Raman spectra at 800- 900 cm^{-1} of LiFSA, G4 and (c) $2.23 \leq C_e \leq 3.27$ mol L^{-1} or (d) $3.27 \leq C_e \leq 4.26$ mol L^{-1}, respectively.

S4 Simulation of concentration profiles for reversing and re-reversing of applied current using Finite Difference Method (FDM)

The change in the concentration profile upon reversing and re-reversing the direction of the applied current was estimated using Finite Difference Method (FDM) [55,42,43]. A schematic of the FDM calculation is presented in Figure. S4(a). The inter-electrode distance of 600 μm and the inversion current application time of 100 s were divided equally by Δx [μm] or Δt [s]. The number of divisions was determined as 600/Δx and 100/Δt, respectively. Subsequently, using integers g and p greater than 0, the concentration of LiFSA in the electrolyte at $(x, t) = (g\Delta x, p\Delta t)$ was denoted as C_g^P. The left-hand side of Equation. S1 can be expressed as follows:

$$\frac{\partial C}{\partial t} \approx \frac{C_g^{P+1} - C_g^P}{\Delta t} \tag{S11}$$

The right-hand side can be approximated as follows;

$$D\frac{\partial^2 C(x,t)}{\partial x^2} \approx \frac{\left.\frac{\partial C}{\partial x}\right|_{x+\Delta x} - \left.\frac{\partial C}{\partial x}\right|_x}{\Delta x} \tag{S12}$$

$$\approx D\left(\frac{C_{g+1}^P - C_g^P}{\Delta x} - \frac{C_g^P - C_{g-1}^P}{\Delta x}\right)\frac{1}{\Delta x} \tag{S13}$$

$$= D\frac{C_{g+1}^P + C_{g-1}^P - 2C_g^P}{(\Delta x)^2} \tag{S14}$$

from Eq. S1, Eqs. S11 and S14 are equal. Thus, the following relationship is satisfied;

$$\frac{C_g^{P+1} - C_g^P}{\Delta t} = D\frac{C_{g+1}^P + C_{g-1}^P - 2C_g^P}{(\Delta x)^2} \quad (S15)$$

When we express $D\Delta t/(\Delta x)^2 = \gamma$, Eq. S15 can be transformed as Eq. S16;

$$C_g^{P+1} = C_g^P + \gamma\left(C_{g-1}^P + C_{g+1}^P - 2C_g^p\right) \quad (S16)$$

The condition for obtaining C_g^{P+1} is $\gamma < 1/2$. For this paper, Δx and Δt were set to 1.15 μm and 0.01 s. Consequently, the range of *n* and *p* should be $0 \leq g \leq 518$ and $0 \leq p \leq 10000$.

When simulating the change in concentration profile using FDM, the following parameters need to be set: the initial condition with concentration profile at $p = 0$, the boundary condition as the electrode surface concentration, and the parameter *D*, as outlined in Table S1. The values of *D*s used were 0.75×10^{-7} and 1.16×10^{-7} $cm^2\ s^{-1}$, corresponding to *D* near the anode and cathode during electrolysis, respectively (Figure. 4(c)).

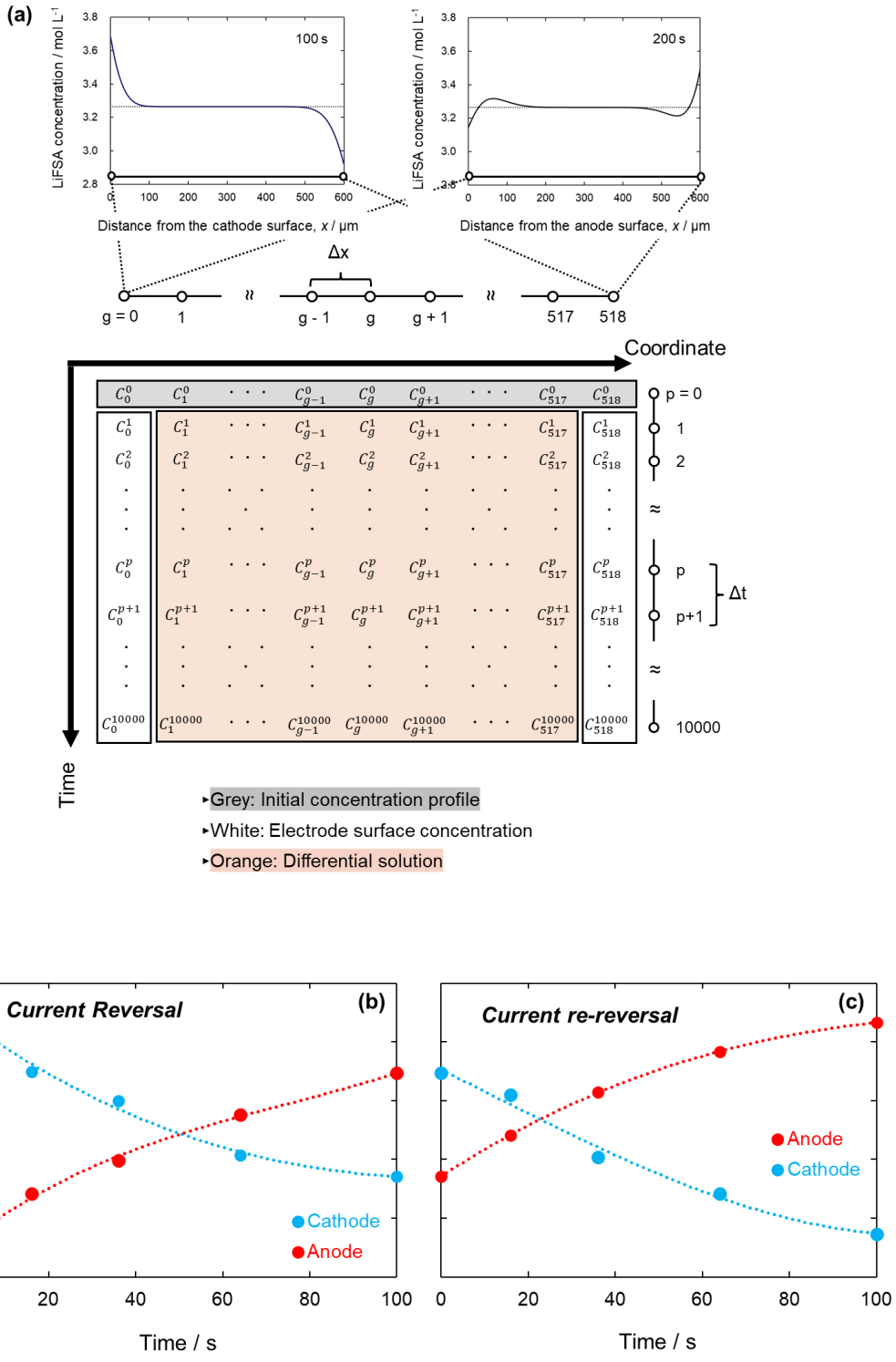

Figure S4. (a) Schematics of FDM. Changes in electrode surface concentration during (b) reversal and (c) re-reversal of the applied current direction.

Table S1. Settings for FDM simulation.

	Initial concentration profile	Electrode surface concentration	Diffusion coefficient $\times 10^{-7}$ cm^2 s^{-1}
During current reversal	Substituting t = 100 for Eqs. S5 and S6	Measured value (Fig. S4(b))	$C_g^p \geq C_{g+1}^p$: 0.75 $C_g^p < C_{g+1}^p$: 1.16
During current re-reversal	Estimated value in FDM at the end of current reversal	Measured value (Fig. S4(c))	$C_g^p \geq C_{g+1}^p$: 1.16 $C_g^p < C_{g+1}^p$: 0.75

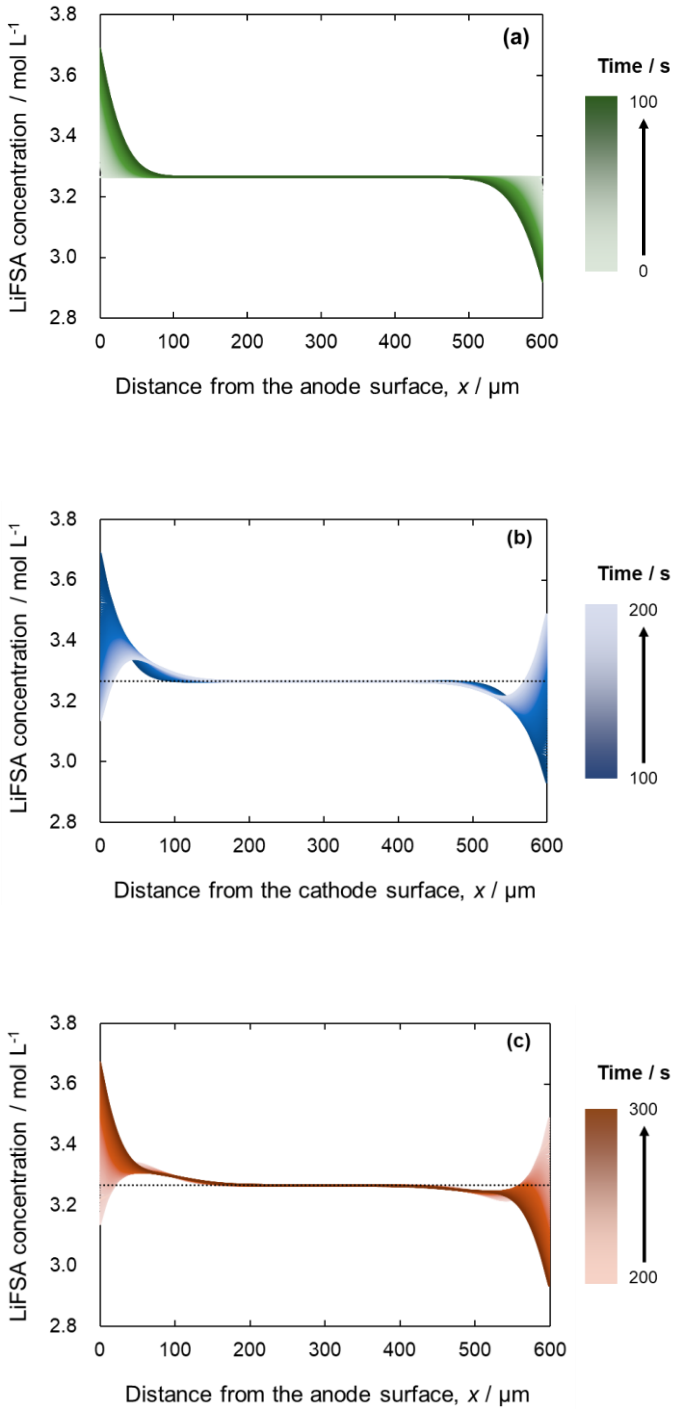

Figure S5. FDM-estimated concentration profiles during (a) electrolysis, (b) reversal and (c) re-reversal of the applied current direction.

References

[1] J. M. Tarascon, M. Armand, *Nature* **2001**, *414*, 359–367.

[2] J. B. Goodenough, Y. Kim, *Chem. Mat.* **2010**, *22*, 587–603.

[3] P. K. Nayak, L. Yang, W. Brehm, P. Adelhelm, *Angewandte Chemie International Edition* **2018**, *57*, 102–120.

[4] Y. Tian, G. Zeng, A. Rutt, T. Shi, H. Kim, J. Wang, J. Koettgen, Y. Sun, B. Ouyang, T. Chen, Z. Lun, Z. Rong, K. Persson, G. Ceder, *Chem. Rev.* **2021**, *121*, 1623–1669.

[5] E. R. Logan, J. R. Dahn, *Trends Chem.* **2020**, *2*, 354–366.

[6] T. Tamura, K. Yoshida, T. Hachida, M. Tsuchiya, M. Nakamura, Y. Kazue, N. Tachikawa, K. Dokko, M. Watanabe, *Chemistry letters* **2010**, *39*, 753–755.

[7] T. Mandai, K. Yoshida, K. Ueno, K. Dokko, M. Watanabe, *Physical chemistry chemical physics* **2014**, *16*, 8761–8772.

[8] Y. Yamada, K. Furukawa, K. Sodeyama, K. Kikuchi, M. Yaegashi, Y. Tateyama, A. Yamada, *Journal of the American Chemical Society* **2014**, *136*, 5039–5046.

[9] K. Sodeyama, Y. Yamada, K. Aikawa, A. Yamada, Y. Tateyama, *The Journal of Physical Chemistry C* **2014**, *118*, 14091–14097.

[10] S. Ko, Y. Yamada, A. Yamada, *Joule* **2021**, *5*, 998–1009.

[11] K. M. Diederichsen, E. J. McShane, B. D. McCloskey, *ACS Energy Letters* **2017**, *2*, 2563–2575.

[12] Y. Yamada, J. Wang, S. Ko, E. Watanabe, A. Yamada, *Nature Energy* **2019**, *4*, 269–280.

[13] K. Dokko, D. Watanabe, Y. Ugata, M. L. Thomas, S. Tsuzuki, W. Shinoda, K. Hashimoto, K. Ueno, Y. Umebayashi, M. Watanabe, *The Journal of Physical Chemistry B* **2018**, *122*, 10736–10745.

[14] Y. Zhang, T.-T. Zuo, J. Popovic, K. Lim, Y.-X. Yin, J. Maier, Y.-G. Guo, *Materials Today* **2020**, *33*, 56–74.

[15] S. Yang, X. Min, H. Fan, J. Xiao, Y. Liu, R. Mi, X. Wu, Z. Huang, K. Xi, M. Fang, *Journal of Materials Chemistry A* **2022**, *10*, 17917–17947.

[16] Y. Chen, T. Wang, H. Tian, D. Su, Q. Zhang, G. Wang, *Adv. Mater.* **2021**, *33*, 2003666.

[17] K. Chen, D.-Y. Yang, G. Huang, X.-B. Zhang, *Accounts Chem. Res.* **2021**, *54*, 632–641.

[18] J. Newman, K. E. Thomas-Alyea, *Electrochemical Systems*, John Wiley & Sons, **2012**.

[19] G. Kamesui, K. Nishikawa, M. Ueda, H. Matsushima, *Electrochemistry Communications* **2023**, 107506.

[20] Y. Choo, D. M. Halat, I. Villaluenga, K. Timachova, N. P. Balsara, *Progress in Polymer Science* **2020**, *103*, 101220.

[21] K. Obata, R. Van De Krol, M. Schwarze, R. Schomäcker, F. F. Abdi, *Energy & Environmental Science* **2020**, *13*, 5104–5116.

[22] M. Paunovic, M. Schlesinger, *Fundamentals of Electrochemical Deposition*, John Wiley & Sons, **2006**.

[23] P. Bai, J. Li, F. R. Brushett, M. Z. Bazant, *Energy & Environmental Science* **2016**, *9*, 3221–3229.

[24] B. Horstmann, J. Shi, R. Amine, M. Werres, X. He, H. Jia, F. Hausen, I. Cekic-Laskovic, S. Wiemers-Meyer, J. Lopez, *Energy & Environmental Science* **2021**, *14*, 5289–5314.

[25] G. Kamesui, K. Nishikawa, M. Ueda, H. Matsushima, *ACS Energy Letters* **2022**, *7*,

4089–4097.

[26] B. Boz, T. Dev, A. Salvadori, J. L. Schaefer, *Journal of The Electrochemical Society* **2021**, *168*, 090501.

[27] A. Mistry, V. Srinivasan, H.-G. Steinrück, *Advanced Energy Materials* **2023**, *13*, 2203690.

[28] K. Nishikawa, T. Mori, T. Nishida, Y. Fukunaka, M. Rosso, *Journal of electroanalytical chemistry* **2011**, *661*, 84–89.

[29] T. Nishida, K. Nishikawa, M. Rosso, Y. Fukunaka, *Electrochim. Acta* **2013**, *100*, 333–341.

[30] X. Xu, Y. Liu, J.-Y. Hwang, O. O. Kapitanova, Z. Song, Y.-K. Sun, A. Matic, S. Xiong, *Adv. Energy Mater.* **2020**, *10*, 2002390.

[31] A. Miki, K. Nishikawa, G. Kamesui, H. Matsushima, M. Ueda, M. Rosso, *Journal of Materials Chemistry A* **2021**, *9*, 14700–14709.

[32] A. A. Wang, A. B. Gunnarsdóttir, J. Fawdon, M. Pasta, C. P. Grey, C. W. Monroe, *ACS energy letters* **2021**, *6*, 3086–3095.

[33] A. Mistry, V. Srinivasan, *Joule* **2021**, *5*, 2773–2776.

[34] Y. Gao, F. Qiao, J. You, C. Shen, H. Zhao, J. Gu, Z. Ren, K. Xie, B. Wei, *J. Energy Chem.* **2021**, *55*, 580–587.

[35] F. R. McLarnon, R. H. Muller, C. W. Tobias, *JOSA* **1975**, *65*, 1011–1018.

[36] F. R. McLarnon, R. H. Muller, C. W. Tobias, *Electrochimica Acta* **1976**, *21*, 101–105.

[37] K. Nishikawa, Y. Fukunaka, T. Sakka, Y. H. Ogata, J. R. Selman, *Journal of Electroanalytical Chemistry* **2005**, *584*, 63–69.

[38] H. You, J. Fang, F. Chen, C. Zhu, X. Song, B. Ding, *Chemical Physics Letters* **2008**,

465, 131–135.

[39] A. Miki, K. Nishikawa, T. Ozawa, H. Matsushima, M. Ueda, *Journal of The Electrochemical Society* **2020**, *167*, 062501.

[40] K. Nishikawa, T. Saito, H. Matsushima, M. Ueda, *Electrochimica Acta* **2019**, *297*, 1104–1108.

[41] G. Kamesui, K. Nishikawa, H. Matsushima, M. Ueda, *Journal of The Electrochemical Society* **2021**, *168*, 031507.

[42] D. Anderson, J. C. Tannehill, R. H. Pletcher, *Computational Fluid Mechanics and Heat Transfer*, Taylor & Francis, **2016**.

[43] M. N. Özişik, H. R. Orlande, M. J. Colaço, R. M. Cotta, *Finite Difference Methods in Heat Transfer*, CRC Press, **2017**.

[44] K. Fujii, H. Hamano, H. Doi, X. Song, S. Tsuzuki, K. Hayamizu, S. Seki, Y. Kameda, K. Dokko, M. Watanabe, *The Journal of Physical Chemistry C* **2013**, *117*, 19314–19324.

[45] H. Yoon, A. S. Best, M. Forsyth, D. R. MacFarlane, P. C. Howlett, *Physical Chemistry Chemical Physics* **2015**, *17*, 4656–4663.

[46] Y. Yamada, A. Yamada, *J. Electrochem. Soc.* **2015**, *162*, A2406–A2423.

[47] J. Grondin, J.-C. Lassègues, M. Chami, L. Servant, D. Talaga, W. A. Henderson, *Physical Chemistry Chemical Physics* **2004**, *6*, 4260–4267.

[48] S. Terada, K. Ikeda, K. Ueno, K. Dokko, M. Watanabe, *Aust. J. Chem.* **2019**, *72*, 70.

[49] S. Tsuzuki, T. Mandai, S. Suzuki, W. Shinoda, T. Nakamura, T. Morishita, K. Ueno, S. Seki, Y. Umebayashi, K. Dokko, *Physical Chemistry Chemical Physics* **2017**, *19*, 18262–18272.

[50] J. Fawdon, J. Ihli, F. L. Mantia, M. Pasta, *Nature Communications* **2021**, *12*, 1–9.

[51] S. Pfeifer, F. Ackermann, F. Sälzer, M. Schönhoff, B. Roling, *Physical Chemistry Chemical Physics* **2021**, *23*, 628–640.

[52] K. Ueno, K. Yoshida, M. Tsuchiya, N. Tachikawa, K. Dokko, M. Watanabe, *J. Phys. Chem. B* **2012**, *116*, 11323–11331.

[53] A. Fick, *The London, Edinburgh, and Dublin Philosophical Magazine and Journal of Science* **1855**, *10*, 30–39.

[54] A. A. Wang, T. Hou, M. Karanjavala, C. W. Monroe, *Electrochimica Acta* **2020**, *358*, 136688.

[55] Akira Itoh, *[Transport Phenomena in Excel with ease] Excel de Kigaru ni Idogenshoron (in Japanese)*, Maruzen Publishing, **2014**.

Chapter 5: Correlation between Electrolyte Concentration and Lithium Morphology during Lithium Bis(fluorosulfonyl)amide–Tetraglyme Electrolyte Deposition–Dissolution Reactions

5.1 Introduction

High energy-density batteries have recently increased in importance because of more electric vehicles and renewable energy being produced.[1] However, Li ion battery capacity limits will soon be reached,[2] meaning there is an urgent need for new battery materials to be developed for use in next-generation batteries.[3]

In 2014, Yamada et al. discovered that high-concentration electrolytes (HCEs) have unique electrochemical properties. The electrolyte concentration is three times higher in a HCE battery than a conventional Li ion battery.[4] In a HCE, almost all of the solvent molecules are coordinated to cations. This unique structure increases the energy level of the lowest unoccupied molecular orbital of the solvent[5] and causes a stable anion-based solid–electrolyte interphase to form. HCEs used in Li batteries can give outputs of 4–5 V and high energy densities.[5,6] A solvate ionic liquid (a type of HCE) consists of ion pairs of solvated cations and anions at room temperature. Solvate ionic liquids have high ionic conductivities and are very thermally stable.[7]

An anode-free battery (AFB) is a type of next-generation battery in which the current collector is also the negative electrode, allowing a higher energy density to be achieved than in conventional batteries.[8] However, inactive Li can form on the negative electrode surface of an AFB. Inactive Li does not take part in charge–discharge reactions.[9] The formation of inactive Li therefore decreases the coulombic efficiency of a battery. Extensive deposits of inactive Li may cause short circuiting between the electrodes and therefore pose a fire hazard. The mechanisms involved in Li deposition need to be identified to allow safe AFBs with high coulombic efficiencies to be developed.

Li deposition reactions at the negative electrode cause the Li^+ concentration at the negative electrode surface to decrease. The concentration gradient between the

electrode surface and the bulk electrolyte drives Li^+ diffusion from the bulk electrolyte toward the electrode.[10] During electrochemical dissolution of Li, the Li^+ concentration at the negative electrode surface increases and the concentration gradient between the electrode surface and the bulk electrolyte drives Li^+ diffusion from the electrode toward the bulk electrolyte.[11] The morphology of a Li deposit will be affected by the Li^+ concentration at the electrode surface, C_s, which will depend on the initial Li^+ concentration in and Li^+ transport characteristics of the bulk electrolyte.[12] However, the relationship between Li^+ mass transfer and Li deposit morphology during charge–discharge cycles in a HCE battery is poorly understood.

The measurement of metal ion concentration distribution in electrolytes has been performed using techniques such as Scanning Electrochemical Microscopy (SECM) [13], Magnetic Resonance Imaging (MRI) [14], and Laser Interferometry[15,16]. SECM can visualize concentration distributions. However, the probe may interfere with the ion flow. MRI allows for non-contact and non-destructive measurements. On the other hand, it requires an electrode distance of more than 5 mm. Laser Interferometry can measure without contacting the sample. It allows observation at narrow electrode distances of less than 1 mm, enabling the acquisition of transport phenomenon data in cells that faithfully replicates the battery environment.

We have previously used laser interferometry to investigate changes in electrolyte concentrations near the electrodes of batteries.[10,17–19] Laser interferometry has been used to detect changes in electrolyte concentrations for more than half a century.[20–22] Laser interferometry allows the electrolyte concentration to be measured in situ without disturbing the electrolyte or decomposing the components of the electrolyte liquid. In previous studies, we successfully estimated diffusion coefficients and

transference numbers by performing non-steady-state diffusion mode analyses.[11] In the study described here, we used in situ interferometry to measure C_s. Li deposits during electrodeposition and chemical dissolution were observed in situ by digital microscopy (DM) and the morphologies of the deposits were assessed ex situ by scanning electron microscopy (SEM). Correlations between C_s and Li morphology were investigated.

5.2 Experimental

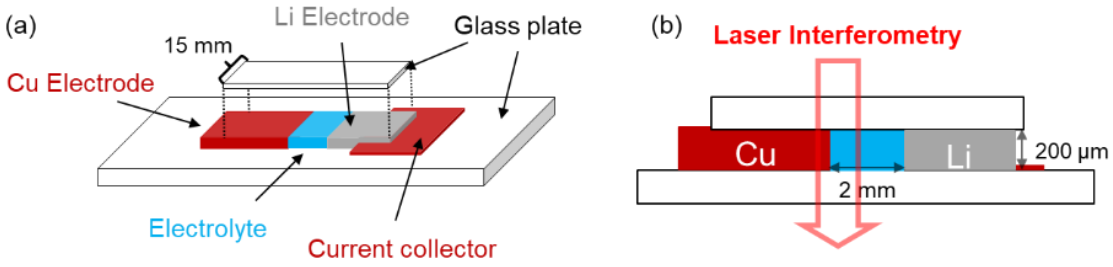

Figure 1. (a) Overview and (b) cross-sectional view of the electrochemical cell for interferometry and digital microscopy.

The electrochemical cell is shown schematically in Figure 1(a) and 1(b). A Cu plate (99.99% pure; Nilaco, Japan) and Li foil (99.9% pure; Honjo Metal, Japan) were used as the working and counter electrodes, respectively. Each electrode was 15 mm long and 200 μm wide. The inter-electrode distance was 2 mm. Cu foil 2 μm thick was placed under the Li electrode to act as a current collector. The surfaces of the electrodes were parallel to each other. A quasi-two-dimensional cell configuration was used to suppress natural convection in the electrolyte. Before use, the Cu plate was polished with waterproof abrasive paper of grades #800, #1200, and then #3000. The oxide film on the electrode surface was then removed using 0.1 mol L^{-1} nitric acid. The electrode surface was then washed with acetone, ethanol, and pure water, in that order. The top and bottom of the electrode were then coated with silicone (FC-112RTV; Fine Chemical, Japan) to insulate the electrode sides. The electrolyte was then injected between the two electrodes, and then the injection ports were sealed with epoxy resin.

The electrolyte was prepared by mixing lithium bis(fluorosulfonyl)amide (LiFSA; 99.9% pure; Nippon Shokubai, Japan) and tetraglyme (G4; 98% pure; Kishida Chemical, Japan) at 50 °C on a hot plate with stirring. The LiFSA to G4 molar ratio is

later labeled $M_{LiFSA/G4}$. Five electrolyte solutions were used in the experiments. The $M_{LiFSA/G4}$s of the five electrolyte solutions were 0.7, 0.85, 1.0, 1.15, and 1.3 and the LiFSA concentrations were 2.52, 2.91, 3.27, 3.59, and 3.89 mol L^{-1}, respectively.[11] The electrochemical cell and electrolyte solutions were all prepared in a dry room with a dew point < −50 °C.

Each electrochemical experiment was performed at 23 °C. The Li electrodeposition and chemical dissolution experiments were performed at 3 mA cm^{-2} using a potentiostat (HZ-Pro S12; Hokuto Denko, Japan). The deposition and dissolution times were both 200 s. The cut-off voltage was ±3 V. Li deposition and dissolution on the Cu electrode surface was observed in situ using a DM instrument (VHX-1000; Keyence, Japan) using a magnification of 500×. The DM image acquired at each selected time point was trisected horizontally and the largest Li deposit in each region was measured.[17]

The morphologies of the Li deposits on the Cu electrode after the first and sixth deposition processes were assessed using a field emission SEM instrument (JSM-7800F; JEOL, Tokyo, Japan). The electrochemical cell was disassembled at the end of the deposition process, and the electrode to be assessed was carefully washed with G4 and transferred to the SEM instrument in an air-tight holder.

Changes in the electrolyte concentration near the electrode during the deposition–dissolution processes were measured using a digital holographic interferometer (DHM T1000; Lyncée Tec, Switzerland). The wavelength of the laser beam was 683.6 nm. The optical path length was 200 μm. The objective lens magnification was 5×. The holograms produced by the digital holographic interferometer were analyzed using Koala software (Lyncée Tec) to get the LiFSA concentration profile in the electrolyte.[11]

5.3 Results and Discussions

(a) $M_{LiFSA/G4}$ = 0.7

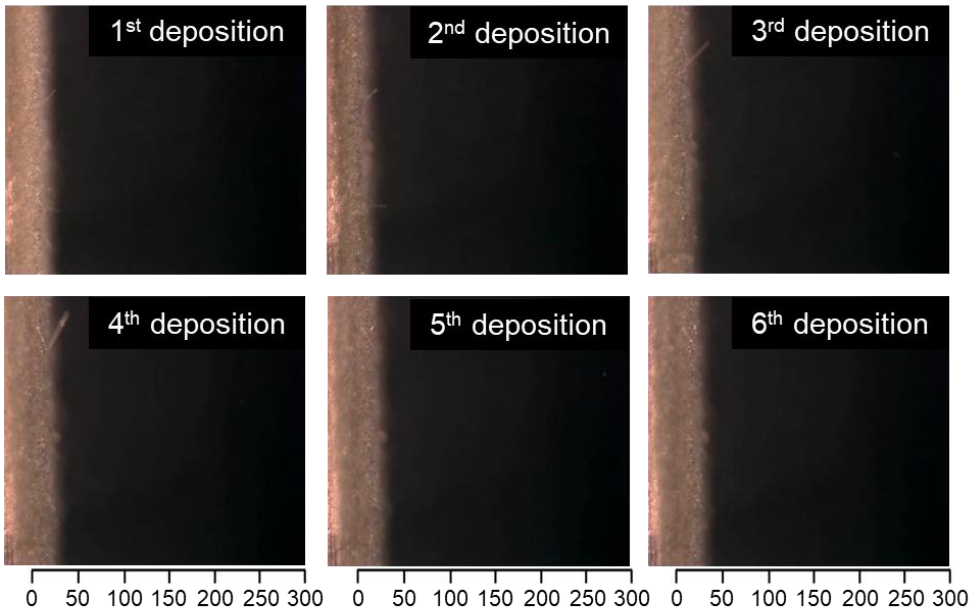

Distance from the Cu electrode surface / μm

(b) $M_{LiFSA/G4}$ = 1.0

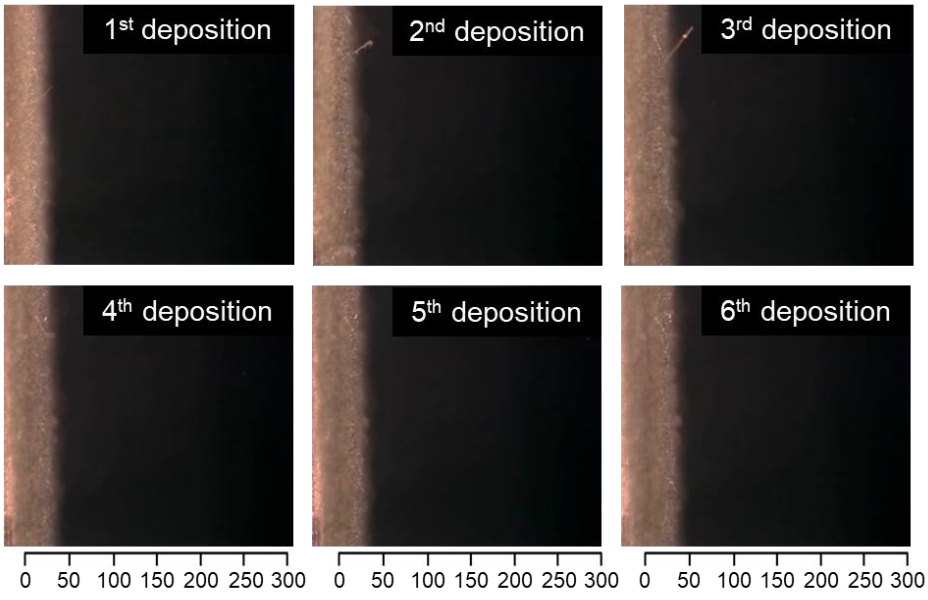

Distance from the Cu electrode surface / μm

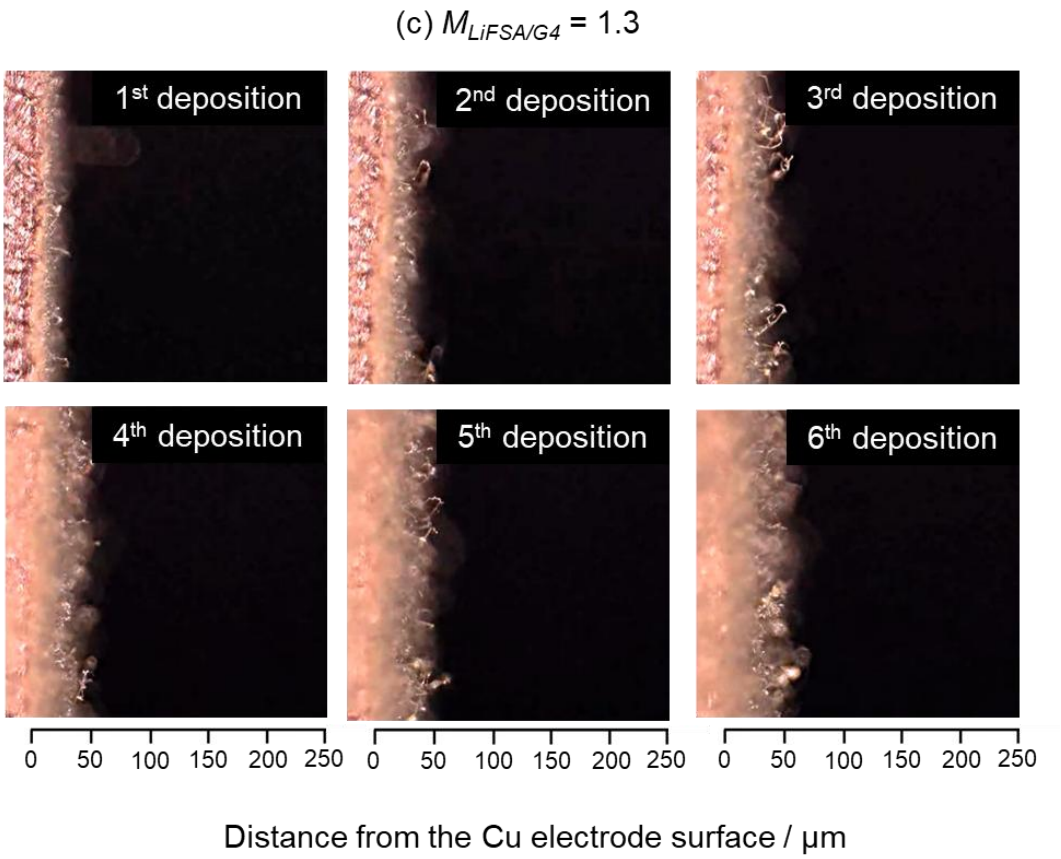

Figure 2 Electrodeposition process observation in $M_{LiFSA/G4}$ = (a) 0.7, (b) 1.0, (c) 1.3 by optical microscopy.

Li deposition and dissolution on the electrode surfaces in the experiments with $M_{LiFSA/G4}$s of 0.7, 1.0, and 1.3 recorded by DM are shown in Figures 2(a), 2(b), and 2(c), respectively. When electrodeposition in the experiment with $M_{LiFSA/G4}$ = 0.7 started, fibrous silver-colored deposits started to be produced and eventually covered the entire electrode surface. DM was focused on the electrode edge, so the view of the deposits in the depth direction was blurred. Needle-like deposits protruded from various points on the deposit surfaces. When dissolution started, the deposits stopped growing and the deposits became darker in color. This color change was probably caused by changes in the way light was reflected as the deposits dissolved. The needles became thinner and

dissolved. When electrodeposition resumed, the deposits became silver-colored again and became thicker. The deposits grew by pushing the residues that had not fully dissolved during the dissolution reaction in the direction of the bulk solution. Needles again grew from the same locations as before dissolution. When dissolution recommenced, less shadowing occurred than in the previous cycle. Some needles became broken and lay horizontally on the deposit surfaces. Similar dynamic behaviors were observed on both the anode and cathode surfaces during repeated cycles. However, fewer needles formed in the later cycles. The deposits appeared to be slightly coarser in the experiment with $M_{LiFSA/G4}$ = 1.0 than with $M_{LiFSA/G4}$ = 0.7.

In the experiment with $M_{LiFSA/G4}$ = 1.3, thick silver-colored deposits formed during electrodeposition but were in specific areas rather than uniformly distributed like in the experiments with $M_{LiFSA/G4}$ = 0.7 and 1.0. The fibers were large, and some deposits broke as they grew and formed loop-like structures. During dissolution, the deposits dissolved from the tips, shrank, and eventually lay horizontally. The deposits were darker at the end of the dissolution process than at the onset of dissolution. When electrodeposition resumed, silver-colored deposits formed again. The deposits grew by filling in the gaps between undissolved fibers. The deposit became unevenly shaped because many loop-like deposits formed. Dissolution caused the deposits to shrink. Undissolved fibers became subsumed by the layered deposit. The old layer gradually became uneven.

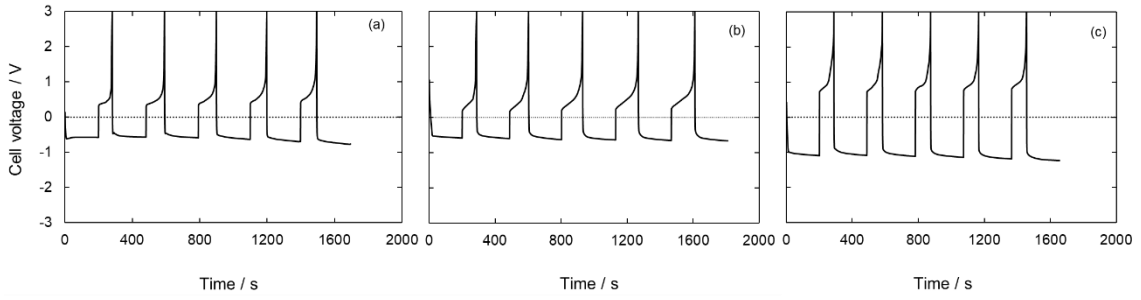

Figure 3. Voltage profiles during the Li electrodeposition and chemical dissolution experiments with $M_{LiFSA/G4}$ = (a) 0.7, (b) 1.0, and (c) 1.3.

Changes in the cell voltage during the deposition–dissolution cycles are shown in Figure 3(a)–3(c). When a cathodic current was applied, the cell voltage remained almost constant for 200 s whatever the $M_{LiFSA/G4}$ and cycle number. This indicated that reduction of Li^+ occurred continually. The cell voltage increased as $M_{LiFSA/G4}$ increased. When the direction of the applied current was reversed, the cell voltage became positive. The voltage increased over time at all $M_{LiFSA/G4}$s. The voltage increased sharply until the reactive deposits were almost completely dissolved. We calculated the coulombic efficiency (CE), defined as the deposition time to dissolution time ratio. The CEs for the first cycle in the experiments with $M_{LiFSA/G4}$ = 0.7, 1.0, and 1.3 were 41%, 45%, and 44%, respectively. The mean CEs for the second to fifth cycles in the experiments with $M_{LiFSA/G4}$ = 0.7, 1.0, and 1.3 were 51%, 65%, and 46%, respectively. The relationship between the electrolyte concentration and CE is discussed below.

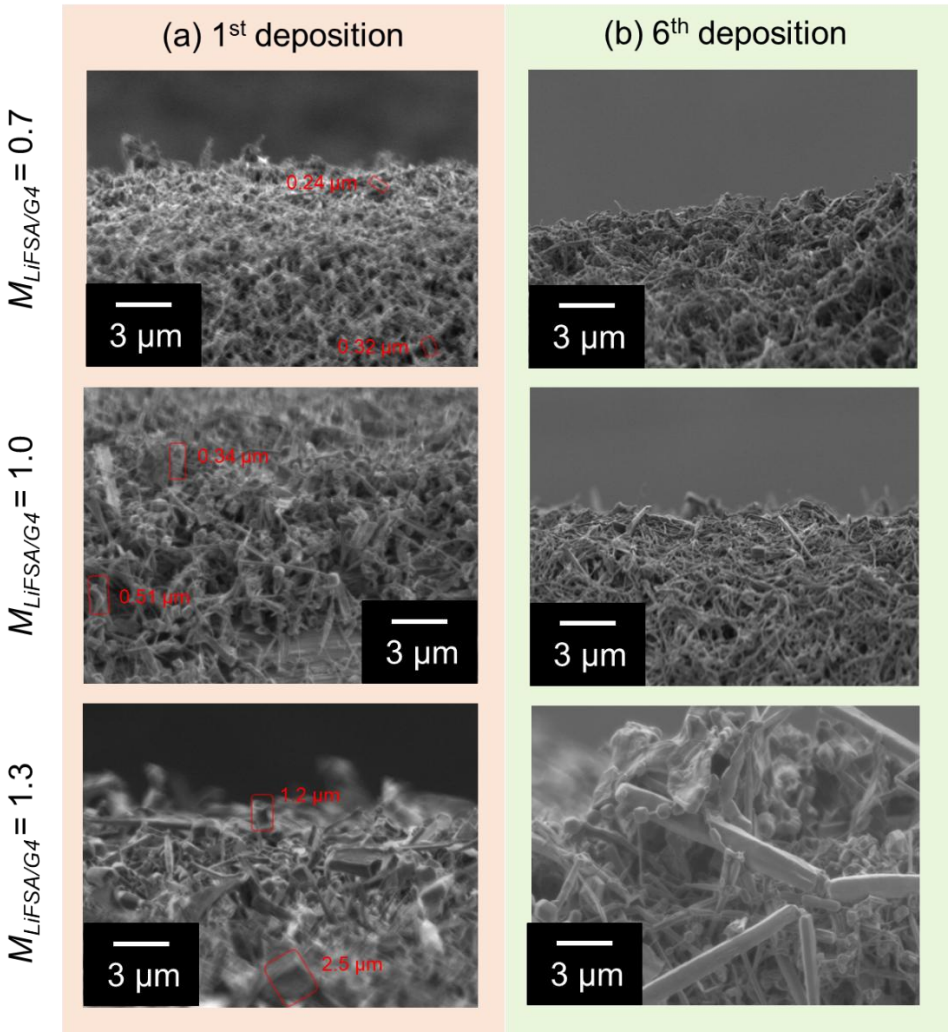

Figure 4. Scanning electron microscopy images of the electrode surfaces after the (a) first and (b) sixth deposition processes.

For the experiments with $M_{LiFSA/G4}$ = 0.7, 1.0, and 1.3, SEM images of the electrode surfaces after the (a) first and (b) sixth deposition processes are shown in Figure 4. In all of these experiments, needle-like or fibrous Li deposits covered the electrode surfaces. The morphologies of the deposits did not depend strongly on the cycle number. The SEM images clearly indicated that thick fibers with large diameters formed when $M_{LiFSA/G4}$ was high. SEM images of the electrode edges were acquired, like for the DM movies. The

lower part of each SEM image therefore shows the area near the substrate surface and the upper part shows the area in contact with the electrolyte. The diameters of the deposits in the red boxes were measured. The deposits near the substrates had larger diameters than the deposits near the surfaces. This tendency became more pronounced as $M_{LiFSA/G4}$ increased. The diameters of the deposits near the substrates and surfaces were 0.32 and 0.24 μm, respectively, at $M_{LiFSA/G4}$ = 0.7, 0.51 and 0.34 μm, respectively, at $M_{LiFSA/G4}$ = 1.0, and 2.5 and 1.2 μm, respectively, at $M_{LiFSA/G4}$ = 1.3. The deposits near the substrates formed characteristic morphologies early in the cycling process. The direct supply of Li^+ from the bulk solution probably caused the deposits to be larger near the substrates than near the surfaces. The deposits in the deposition layer grew as the number of cycles increased. Li^+ was supplied to these deposits through spaces between undissolved fibers. As the cycle number increased, undissolved fibers accumulated on the substrate. This accumulation is expected to reduce the flux of Li^+ supplied from the bulk to the electrode surface, as the fibers can obstruct the flow. Consequently, the Li^+ flux may decrease with the number of cycles. This decrease in Li^+ flux is likely to promote the formation of smaller diameter deposits, resulting in a porous deposition layer with larger pore size.

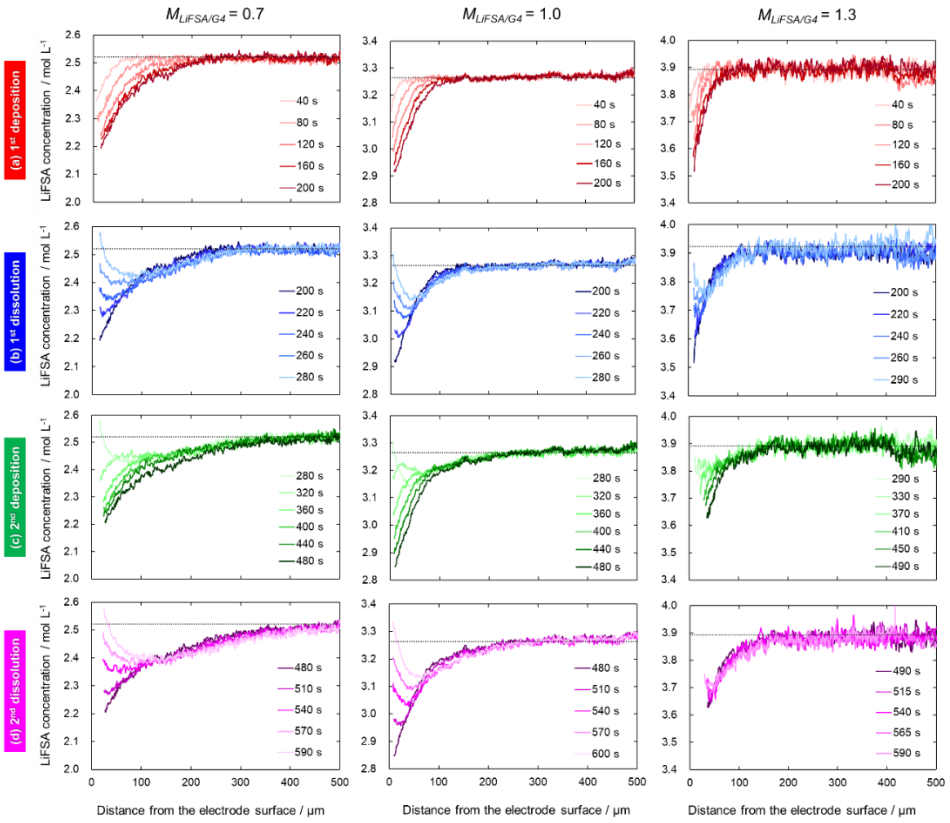

Figure 5. Concentration profiles near the electrodes during (a) the first deposition process, (b) the first dissolution process, (c) the second deposition process, and (d) the second dissolution process.

Temporal changes in the concentrations near the electrodes during the Li deposition–dissolution cycles, determined by interferometry, are shown in Figures 5(a)–5(d). During the first deposition process, Li^+ was consumed at the electrode surface and C_s decreased. Li^+ diffused from the bulk solution toward the electrode surface because of the concentration gradient. When the direction of the applied current was reversed, the Li deposits started to be dissolved and C_s increased. A concave concentration profile was found near the electrode. When the current direction was reversed again, Li electrodeposition occurred and C_s again decreased, resulting in a positive concentration

gradient. During the second dissolution process, a concave concentration profile formed again. These changes in the concentration gradient were consistent with the results of a previous study.[11]

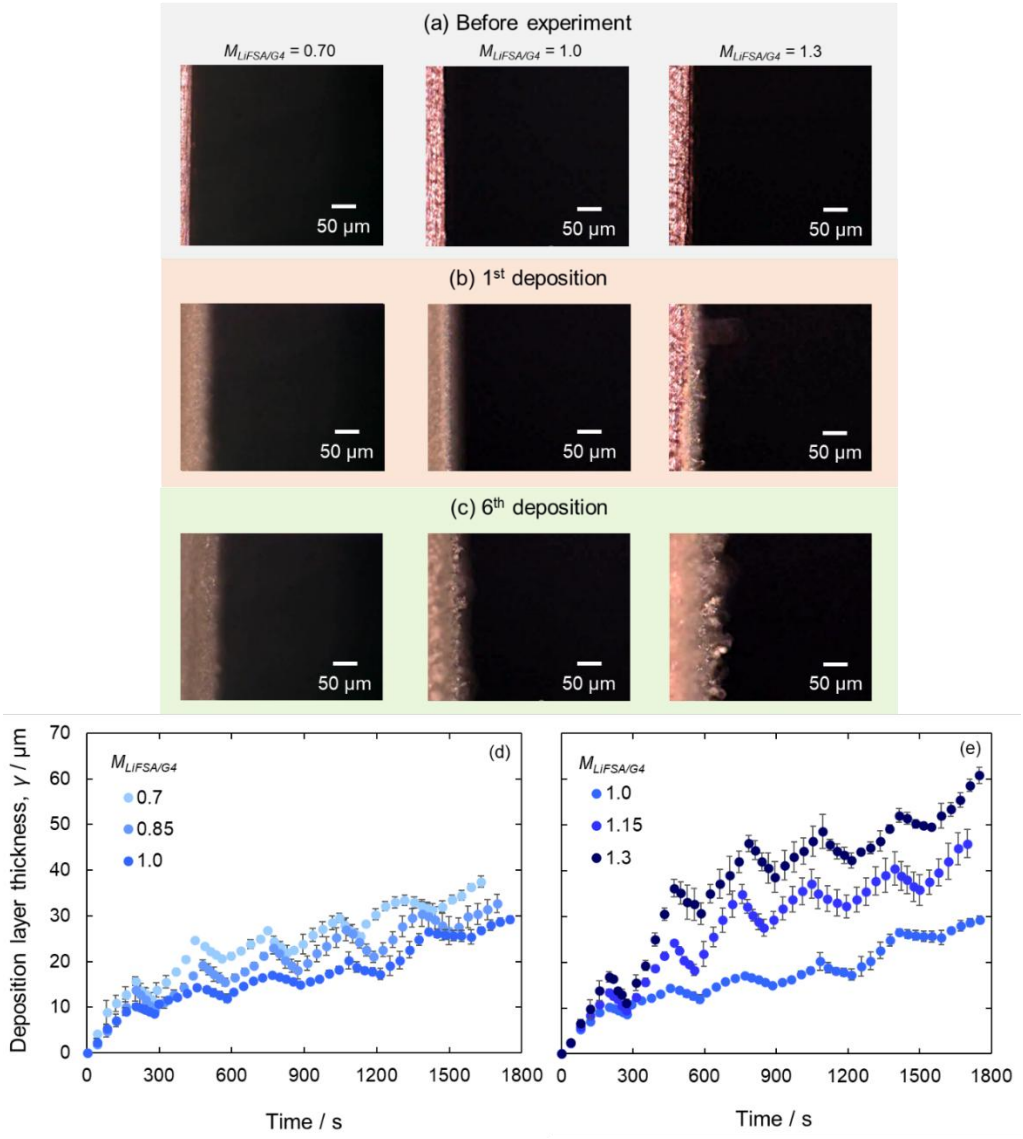

Figure 6. Digital microscopy images acquired near the electrodes (a) before the experiment and after the (b) first and (c) sixth deposition processes. Temporal changes in the deposition layer thickness at $M_{LiFSA/G4}$ = (d) 0.7–1.0 and (e) 1.0–1.3 during the Li deposition–dissolution cycles.

Some DM images acquired near the electrodes (a) before the experiment and after the (b) first and (c) sixth deposition processes are shown in Figures 6(a)–6(c). The DM images confirmed that the diameters of the deposits increased as $M_{LiFSA/G4}$ increased. The deposition layer thickness, γ, increased as the number of cycles increased.

Plots of γ against time for the experiments at different $M_{LiFSA/G4}$s are shown in Figures 6(d)–6(e). At all $M_{LiFSA/G4}$s, γ increased as the number of cycles increased. The increase in γ during deposition was not completely lost during dissolution, suggesting that inactive Li formed during the dissolution process. The lowest γ values throughout the cycles were found at $M_{LiFSA/G4} = 1.0$. At $M_{LiFSA/G4} \leq 1$, γ increased as $M_{LiFSA/G4}$ decreased. At $M_{LiFSA/G4} \geq 1$, γ increased as $M_{LiFSA/G4}$ increased. The trends in γ found during the first electrodeposition process recurred in the second cycle.

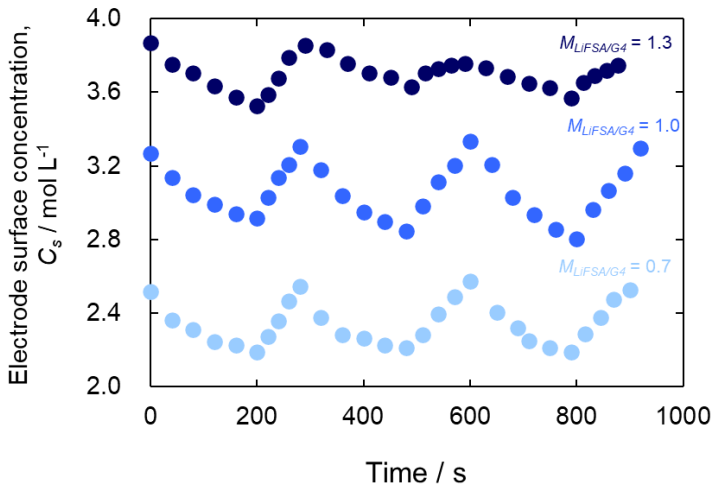

Figure 7. Changes in the electrode surface concentrations during the deposition–dissolution reaction cycles.

Temporal variations in C_s for the first–third deposition–dissolution cycles are

shown in Figure 7. In the first cycle, the maximum changes in C_s (ΔC_s) at $M_{LiFSA/G4}$ = 0.7, 1.0, and 1.3 were 0.33, 0.35, and 0.34 mol L^{-1}, respectively. Generally, in a binary salt–solvent electrolyte, the lower the diffusion coefficient of the salt, the higher the ΔC_s during electrolysis. However, the higher the cation transference number for the electrolyte, the smaller was ΔC_s. We previously found LiFSA diffusion coefficients of 1.6×10^{-7}, 1.2×10^{-7}, and 1.1×10^{-7} cm^2 s^{-1} and Li^+ transference numbers of 0.39, 0.53, and 0.72 for the LiFSA–G4 electrolyte at $M_{LiFSA/G4}$ = 0.7, 1.0, and 1.3, respectively.[11] ΔC_s was very similar for $M_{LiFSA/G4}$ = 0.7, 1.0, and 1.3, possibly because of the trade-off between the diffusion coefficient and transference number.

In the first–third cycles, the C_s ranges at $M_{LiFSA/G4}$ = 0.7, 1.0, and 1.3 did not overlap. ΔC_s remained almost constant during each cycle at each $M_{LiFSA/G4}$. This was consistent with the morphologies of the deposits remaining unchanged between the first and sixth deposition processes. The DM and SEM images confirmed that the morphologies of the deposits at $M_{LiFSA/G4}$ = 0.7, 1.0, and 1.3 were different. The dependence of the deposit morphology on the concentration was attributed to the electrode surfaces being exposed to different C_ss at different $M_{LiFSA/G4}$s.

As $M_{LiFSA/G4}$ increased, C_s also increased, supplying a greater amount of Li^+ to the surface of the deposits. This led to the formation of deposits with larger diameters. As the deposition reaction progressed, C_s decreased, resulting in a reduced supply of Li^+ to the surface. Consequently, the diameter of the deposits near the surface became smaller.

In the early stages of deposition, Li first deposited onto the substrate surface. As the deposition reaction progressed, a layer of deposits accumulated. Over time, C_s decreases, causing the diameter of the deposits to decrease as they approach the surface layer. When C_s was high, a greater amount of Li^+ was supplied to the tip of the deposits,

leading to the formation of larger deposits near the substrate. In particular, when $M_{LiFSA/G4}$ was 1.3, larger deposits formed near the substrate. In contrast, near the electrolyte surface, C_s was lower than in the early stages of deposition. As a result, the supply of Li^+ decreased, leading to smaller deposit diameters.

We previously found that the viscosity of the binary LiFSA–G4 electrolyte increased exponentially as $M_{LiFSA/G4}$ increased above 1.0, being 81, 127, and 376 mPa s at $M_{LiFSA/G4}$ = 0.7, 1.0, and 1.3, respectively.[11] The lower the electrolyte viscosity the more the deposits could swing during the growth process. Deposit swinging was also found in a previous study[23] and was indicated by our DM movies.

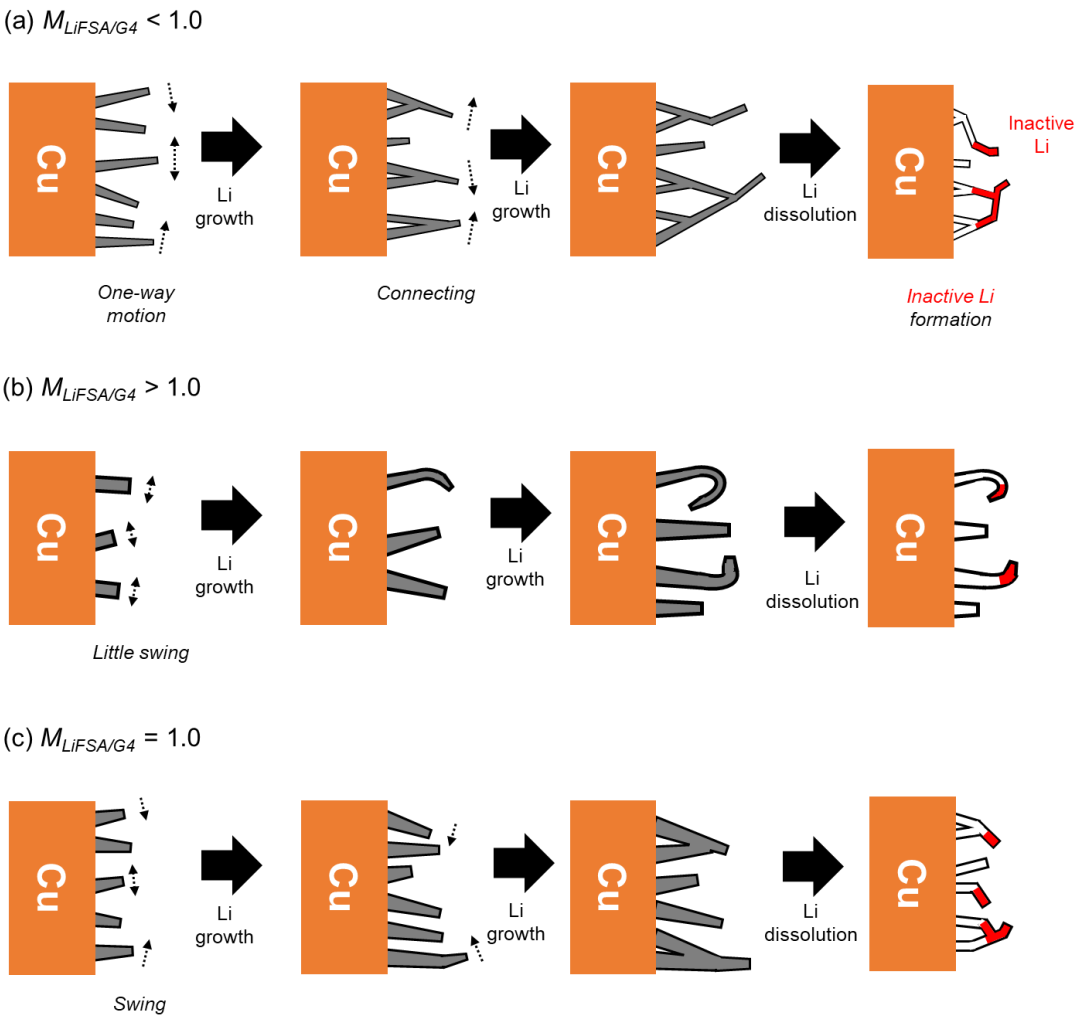

Figure 8. Li deposition–dissolution mechanisms at (a) $M_{LiFSA/G4} < 1.0$, (b) $M_{LiFSA/G4} > 1.0$, and (c) $M_{LiFSA/G4} = 1.0$.

Different Li deposition–dissolution behaviors were found for $M_{LiFSA/G4} \leq 1.0$ and $M_{LiFSA/G4} \geq 1.0$. Here, we discuss the mechanisms at $M_{LiFSA/G4} < 1.0$, $M_{LiFSA/G4} > 1.0$, and $M_{LiFSA/G4} = 1.0$.

I. Li Deposition–Dissolution Mechanism at $M_{LiFSA/G4} < 1.0$ (Figure 8(a))

At $M_{LiFSA/G4} < 1.0$, the electrolyte has a lower viscosity, which promotes the

formation of a large number of small Li deposits. [24] These deposits are able to grow in a more dynamic manner due to the low electrolyte viscosity, leading to more pronounced, one-way motion as they grow. The dynamic growth results in neighboring deposits connecting with each other, which causes a reticulated and porous deposition layer.

During dissolution, the movement of these interconnected deposits becomes less controlled. As the Li dissolves, the deposits lose contact with the electrode, and their swinging motion results in the disconnection of the tips from the electrode. This leads to the formation of inactive Li, as these disconnected portions are no longer electrochemically accessible. [25] The high porosity and loss of electrical contact contribute to the increased formation of inactive Li, explaining why the CE is lower at $M_{LiFSA/G4} < 1.0$ compared to higher concentrations.

II. Li Deposition–Dissolution Mechanism at $M_{LiFSA/G4} > 1.0$ (Figure 8(b))

At $M_{LiFSA/G4} > 1.0$, the higher electrolyte viscosity limits the motion of the Li deposits. As a result, fewer but larger deposits are formed during the deposition process. These deposits grow in a more rigid and constrained manner, making it less likely for neighboring deposits to interact with each other. Instead of connecting, the deposits tend to grow outward from the electrode surface toward the bulk solution.

The limited swinging motion during deposition also affects the dissolution process. The rigid and thick deposits bend slightly during dissolution, but they remain mostly intact, with only small portions of the deposits becoming inactive. However, due to the limited flexibility and larger size of the deposits, inactive Li still forms at the tips and stems of the deposits. The increased viscosity also reduces the mobility of ions, which can lead to electrolyte decomposition, [17,26] further lowering the CE at $M_{LiFSA/G4} > 1.0$.

III. Li Deposition–Dissolution Mechanism at $M_{LiFSA/G4}$ = 1.0 (Figure 8(c))

At $M_{LiFSA/G4}$ = 1.0, the viscosity of the electrolyte is moderate, allowing Li deposits to exhibit a controlled swinging behavior. The deposits swing but in a way that maintains connection with neighboring deposits, leading to a dense and compact deposition layer. The swinging motion allows for uniform growth and prevents excessive accumulation of inactive Li during the dissolution process. As a result, the deposition layer exhibits the minimum thickness. The balance between electrolyte viscosity and the mobility of the Li deposits leads to the most efficient deposition and dissolution, resulting in the smallest overall layer thickness.

5.4 Conclusions

The concentration dependence of the morphologies of Li deposits formed during Li deposition–dissolution reactions at 3 mA cm^{-2} were investigated by DM and laser interferometry. Transient changes in electrolyte concentration and concentration at the electrode surface dramatically changed the thickness of the deposition layer and the diameter of the deposits. The Li deposit diameters increased as the electrolyte concentration increased. The dependence of the deposit morphology on the electrolyte concentration was confirmed by the deposit diameters at depth and at the surface of the deposition layer. The Li deposition–dissolution mechanism changed at $M_{LiFSA/G4}$ = 1.0. Increases in the deposition layer thickness were most strongly suppressed at $M_{LiFSA/G4}$ = 1.0. The morphologies of the deposits and the deposition layer thicknesses led us to conclude that an equimolar LiFSA–G4 mixture is an appropriate electrolyte for AFBs. Further suppression of increases in the deposition layer thickness will be essential for further development of AFBs.

References

[1] X. Shen, H. Liu, X.-B. Cheng, C. Yan, J.-Q. Huang, *Energy Storage Materials* **2018**, *12*, 161–175.

[2] P. K. Nayak, L. Yang, W. Brehm, P. Adelhelm, *Angew Chem Int Ed* **2018**, *57*, 102–120.

[3] F. Lionetto, N. Arianpouya, B. Bozzini, A. Maffezzoli, M. Nematollahi, C. Mele, *Journal of Energy Storage* **2024**, *84*, 110849.

[4] Y. Yamada, K. Furukawa, K. Sodeyama, K. Kikuchi, M. Yaegashi, Y. Tateyama, A. Yamada, *J. Am. Chem. Soc.* **2014**, *136*, 5039–5046.

[5] Y. Yamada, A. Yamada, *Journal of The Electrochemical Society* **2015**, *162*, A2406.

[6] S. Ko, Y. Yamada, A. Yamada, *Joule* **2021**, *5*, 998–1009.

[7] T. Mandai, K. Yoshida, K. Ueno, K. Dokko, M. Watanabe, *Physical chemistry chemical physics* **2014**, *16*, 8761–8772.

[8] S. Nanda, A. Gupta, A. Manthiram, *Advanced Energy Materials* **2021**, *11*, 2000804.

[9] C.-J. Huang, H.-C. Tao, P.-J. Chao, C.-Y. Li, B. T. Hotasi, H.-Y. Liu, M.-H. Lin, S.-H. Wu, W.-N. Su, B. J. Hwang, *ACS Nano* **2023**, *17*, 13241–13255.

[10] A. Miki, K. Nishikawa, G. Kamesui, H. Matsushima, M. Ueda, M. Rosso, *Journal of Materials Chemistry A* **2021**, *9*, 14700–14709.

[11] G. Kamesui, K. Nishikawa, M. Ueda, H. Matsushima, *J. Electrochem. Soc.* **2024**, *171*, 040519.

[12] P. Bai, J. Li, F. R. Brushett, M. Z. Bazant, *Energy & Environmental Science* **2016**, *9*, 3221–3229.

[13] C. Gabrielli, E. Ostermann, H. Perrot, V. Vivier, L. Beitone, C. Mace, *Electrochemistry communications* **2005**, *7*, 962–968.

[14] A. A. Wang, A. B. Gunnarsdóttir, J. Fawdon, M. Pasta, C. P. Grey, C. W. Monroe, *ACS Energy Lett.* **2021**, *6*, 3086–3095.

[15] F. R. McLarnon, R. H. Muller, C. W. Tobias, *JOSA* **1975**, *65*, 1011–1018.

[16] I. Arise, Y. Fukunaka, F. R. McLarnon, T. Abe, *Journal of The Electrochemical Society* **2021**, *168*, 080509.

[17] G. Kamesui, K. Nishikawa, M. Ueda, H. Matsushima, *ACS Energy Lett.* **2022**, *7*, 4089–4097.

[18] G. Kamesui, K. Nishikawa, H. Matsushima, M. Ueda, *Journal of The Electrochemical Society* **2021**, *168*, 031507.

[19] G. Kamesui, K. Nishikawa, M. Ueda, H. Matsushima, *Electrochemistry Communications* **2023**, *151*, 107506.

[20] F. R. McLarnon, R. H. Muller, C. W. Tobias, *Electrochimica Acta* **1976**, *21*, 101–105.

[21] R. N. O'Brien, K. S. V. Santhanam, *J Appl Electrochem* **1990**, *20*, 427–437.

[22] K. Wang, Y. Chen, X. Dou, Y. Han, *Advanced Powder Technology* **2021**, *32*, 1766–1773.

[23] T. Nishida, K. Nishikawa, M. Rosso, Y. Fukunaka, *Electrochimica acta* **2013**, *100*, 333–341.

[24] Y. Chen, M. Li, Y. Liu, Y. Jie, W. Li, F. Huang, X. Li, Z. He, X. Ren, Y. Chen, X. Meng, T. Cheng, M. Gu, S. Jiao, R. Cao, *Nat Commun* **2023**, *14*, 2655.

[25] J. Steiger, D. Kramer, R. Mönig, *Electrochimica Acta* **2014**, *136*, 529–536.

[26] M. Metzger, P. Walke, S. Solchenbach, G. Salitra, D. Aurbach, H. A. Gasteiger, *Journal of The Electrochemical Society* **2020**, *167*, 160522.

Chapter 6: The Relationship between Dilution Effects and Mass Transport in Highly Concentrated Electrolytes: Impact on Lithium Electrodeposition Morphology

6.1 Introduction

Lithium-ion batteries (LIBs), since their commercialization in 1989, have been widely integrated into portable electronic devices. Their applications are expected to expand to electric vehicles and satellites.[1] Advancing battery energy density through material development is essential for these broader applications. The energy density is calculated by multiplying the cell voltage and the electrode capacity.[2] Development of electrolytes resistant to decomposition under high cell voltage conditions is crucial for enhancing energy density.

HCEs were first reported by Yamada et al. in 2014.[3] HCEs contain Li salt concentrations exceeding three times that of conventional 1 mol L^{-1} commercial LIB electrolytes. The distinctive feature of HCEs is that almost all solvent molecules coordinate with Li^+, resulting in a wide electrochemical window. [4] LHCEs, formed by mixing HCEs with low-dielectric diluents at 1-2 mol L^{-1}, maintain the local coordination environment of Li^+ while offering lower viscosity and higher ionic conductivity than HCEs.[5] This unique combination of properties makes LHCEs promising candidates for high-energy-density secondary batteries. [6]

During initial battery charging, electrolyte decomposition forms a solid-electrolyte interphase (SEI) on the negative electrode surface.[7] The susceptibility to decomposition is governed by the lowest unoccupied molecular orbital (LUMO). While conventional electrolytes form solvent-derived SEI due to their LUMO characteristics, both HCEs and LHCEs form anion-derived SEI layers.[8] Anion-derived SEIs exhibit superior structural stability during charge-discharge cycles, enhancing battery cyclability.

Lithium metal possesses distinctive characteristics among electrode materials: the lowest density of any metal (0.534 g cm^{-3}), low electrode potential (-3.04 V vs.

standard hydrogen electrode), and high theoretical capacity (3860 mAh g^{-1}).[9] Implementation of Li metal anodes could dramatically enhance battery energy density. However, Li tends to form irregular surface deposits during charging, a tendency that intensifies with repeated charge-discharge cycles.[10] Understanding Li deposition mechanisms in HCEs and LHCEs is therefore critical for their practical implementation in batteries.

Li^+ transport phenomena near the cathode significantly influence electrodeposition behavior.[11,12] When Li deposition begins at the cathode surface, Li^+ consumption creates a concentration gradient between the electrode surface and bulk electrolyte. Li^+ moves from bulk to cathode driven by this gradient, either as solvated species or through an inter-solvent hopping mechanism. During deposition, the Li^+ concentration at the cathode surface progressively decreases, leading to an increase in uncoordinated solvent molecules near the electrode.[13] The magnitude of surface concentration changes depends on Li^+ diffusivity and transference number in the electrolyte. The increase in uncoordinated solvent molecules may affect SEI composition.[14]

Previous studies have compared HCEs and LHCEs in terms of mass transport phenomena, [15,16] cycling performance,[17,18] and Li electrodeposition behavior.[19,20] While LHCEs demonstrate superior Li^+ diffusivity, cycling performance, and more compact Li deposits compared to HCEs, the interconnected relationships between Li electrodeposition, dilution effects, and mass transport remain incompletely understood. A comprehensive understanding of these dilution effects is essential for advancing next-generation high-energy-density batteries.

In this study, we employed laser interferometry to conduct in situ observations

of mass transport phenomena near the electrode during electrodeposition in both HCEs and LHCEs. This non-contact, non-destructive technique enabled real-time observation of concentration changes.[12,14,21–24] We monitored Li growth processes using digital microscopy and examined deposit morphology using scanning electron microscopy (SEM) and scanning transmission electron microscopy (STEM). The SEI was characterized using energy-dispersive X-ray spectroscopy (EDS) in SEM and electron energy loss spectroscopy (EELS) in STEM. By integrating these findings, we elucidated the distinct Li deposition mechanisms in HCEs and LHCEs.

6.2 Experimental

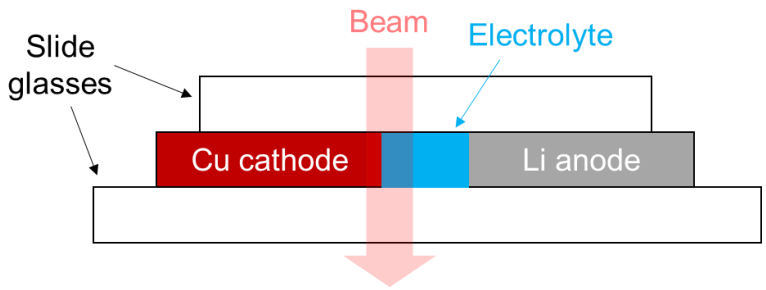

Figure 1. Schematic of the electrochemical cell.

Figure 1 illustrates the electrochemical cell configuration. A Cu plate (99.99%, Nilaco, Japan) served as the cathode and Li foil (99.9%, Honjo Metal, Japan) as the anode. Both electrodes had cross-sectional dimensions of 15 mm (width) × 200 μm (thickness), with an inter-electrode distance of 2 mm. A Cu foil (2 μm thickness) was positioned beneath the Li electrode as a current collector. The electrodes were arranged parallel to each other in a quasi-two-dimensional cell configuration to suppress natural convection in the electrolyte. Prior to experiments, the Cu plate underwent sequential polishing with water-resistant abrasive paper (#800, #1200, and #3000), followed by oxide layer removal

using 0.1 mol L^{-1} nitric acid solution. The electrode surface was then cleaned sequentially with acetone, ethanol, and pure water. The electrode sides were insulated with silicone coating (FC-112RTV, Fine Chemical, Japan). The electrolyte was injected between the electrodes, and the injection port was sealed with epoxy resin.

Lithium bis(fluorosulfonyl) amide (LiFSA, Nippon Shokubai Co., Ltd.) was used as the Li salt, with tetraglyme (G4, Kishida Chemical Co., Ltd.) as the solvent and 1,1,2,2-tetrafluoroethyl-2,2,3,3-tetrafluoropropyl ether (HFE, Daikin Industries Ltd.) as the diluent. These components were mixed in varying ratios. Electrolyte preparation involved stirring the mixtures at 50 °C on a hot plate. All cell assembly and electrolyte preparation were conducted in a dry room maintained at a dew point below -50°C.

Physicochemical property measurements and electrochemical experiments were performed at 23 °C. Electrolyte viscosity and density were measured using a falling ball viscometer (Lovis2000ME, Anton Paar). Refractive indices were determined using a digital refractometer (RX-7000, ATAGO). Li electrodeposition was conducted using a potentiostat (HZ-Pro S12, Hokuto Denko) at current densities of 1, 2, and 3 mA cm^{-2} for 500 s.

Concentration changes near the Cu electrode during Li electrodeposition were monitored using a digital holographic interference microscope (DHM T1000, Lyncée Tec). The system employed a laser with wavelength λ = 683.6 nm, utilizing an optical path length of 200 μm and 5 times objective lens magnification. The relationship between refractive index change (Δn) and concentration change (ΔC) follows:

$$\Delta n = \left(\frac{\partial n}{\partial C}\right)\Delta C \tag{1}$$

where $\partial n/\partial C$ represents the relationship between concentration and refractive index.

From the interference equation:

$$d\Delta n = \left(\frac{\Delta\theta}{2\pi}\right)\lambda \tag{2}$$

where d denotes the cell thickness and $\Delta\theta$ represents the phase difference change. Combining Eqs. 1 and 2 yields:

$$\Delta C = \frac{\lambda}{d} \times \left(\frac{\partial C}{\partial n}\right) \times \frac{\Delta\theta}{2\pi} \tag{3}$$

The holograms were analyzed using Eq. 3 and Koala software (Lyncée Tec) to generate phase change profiles in the electrolyte.

Raman spectra were acquired using a laser micro-Raman spectrometer (LabRAM 1B, HORIBA) with an excitation wavelength of 632.7 nm and spectral resolution of ~1 cm^{-1}. Reference data were collected with exposure time and accumulation settings of 10 s - 5 times, while in-situ measurements employed settings of 10 s - 3 times. For in-situ measurements, the focal point was positioned 20 μm from the electrode surface.

Li electrodeposition on the Cu electrode surface was observed in-situ using a digital optical microscope (VHX-1000, Keyence) at 1000 times magnification. Images were divided horizontally into three equal regions for analysis. The longest Li deposit in each region was measured over time, with average values plotted and standard errors indicated by error bars.[12]

Electrodeposited Li analysis was conducted using SEM (JSM-7800F, JEOL) and STEM (JEM-ARM200F, JEOL). Following cell disassembly, electrode surfaces

were carefully cleaned with G4 and transferred to the microscopes using an air-non-exposure holder. Surface chemical analysis was performed using EDS and EELS. EELS analysis was conducted at -160 °C.

6.3 Results and discussion

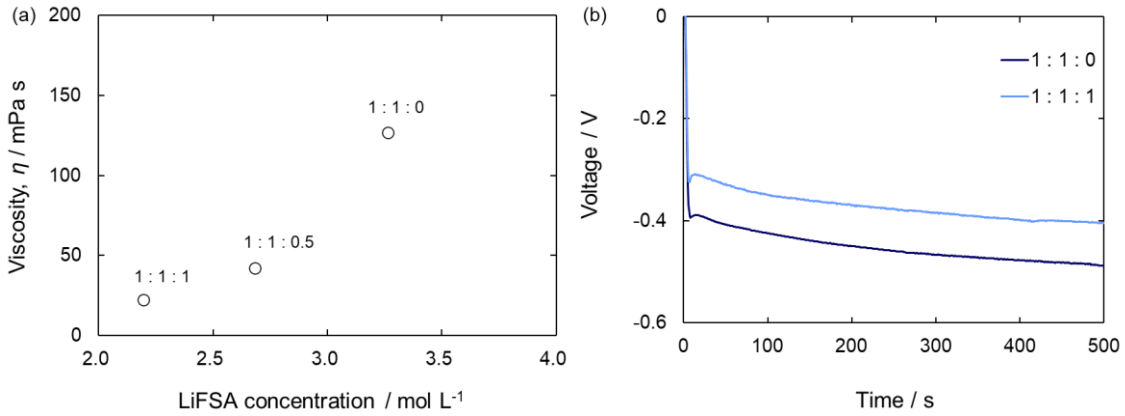

Figure 2. (a) Viscosity of the electrolyte with various LiFSA concentrations. (b) Voltage changes during Li electrodeposition at 3 mA cm^{-2}.

Figure 2(a) presents the electrolyte viscosity, η, as a function of electrolyte concentration. The numerical ratios above the plots represent LiFSA-G4-HFE molar ratios. The LiFSA concentrations were determined from the electrolyte densities. While maintaining a constant LiFSA-G4 ratio, increasing HFE content substantially reduced η; values decreased from 127 mPa s (1:1:0) to 42 mPa s (1:1:0.5) and 22 mPa s (1:1:1).

Figure 2(b) shows the temporal evolution of cell voltage during Li electrodeposition at 3 mA cm^{-2}. Both electrolytes exhibited an overpotential attributed to Li nucleation at 7 seconds after deposition initiation. Subsequently, concentration polarization led to increased overpotential,[25] transitioning from -0.39 V to -0.49 V in

1:1:0 and from -0.31 V to -0.40 V in 1:1:1. Previous potentiostatic impedance measurements by Guo et al. using Li | $LiNi_{0.8}Mn_{0.1}Co_{0.1}O_2$ cells demonstrated higher solution resistance in HCEs compared to LHCEs.[18] The addition of HFE to HCEs likely enhanced ionic conductivity, resulting in lower absolute cell voltage during deposition in LHCEs.

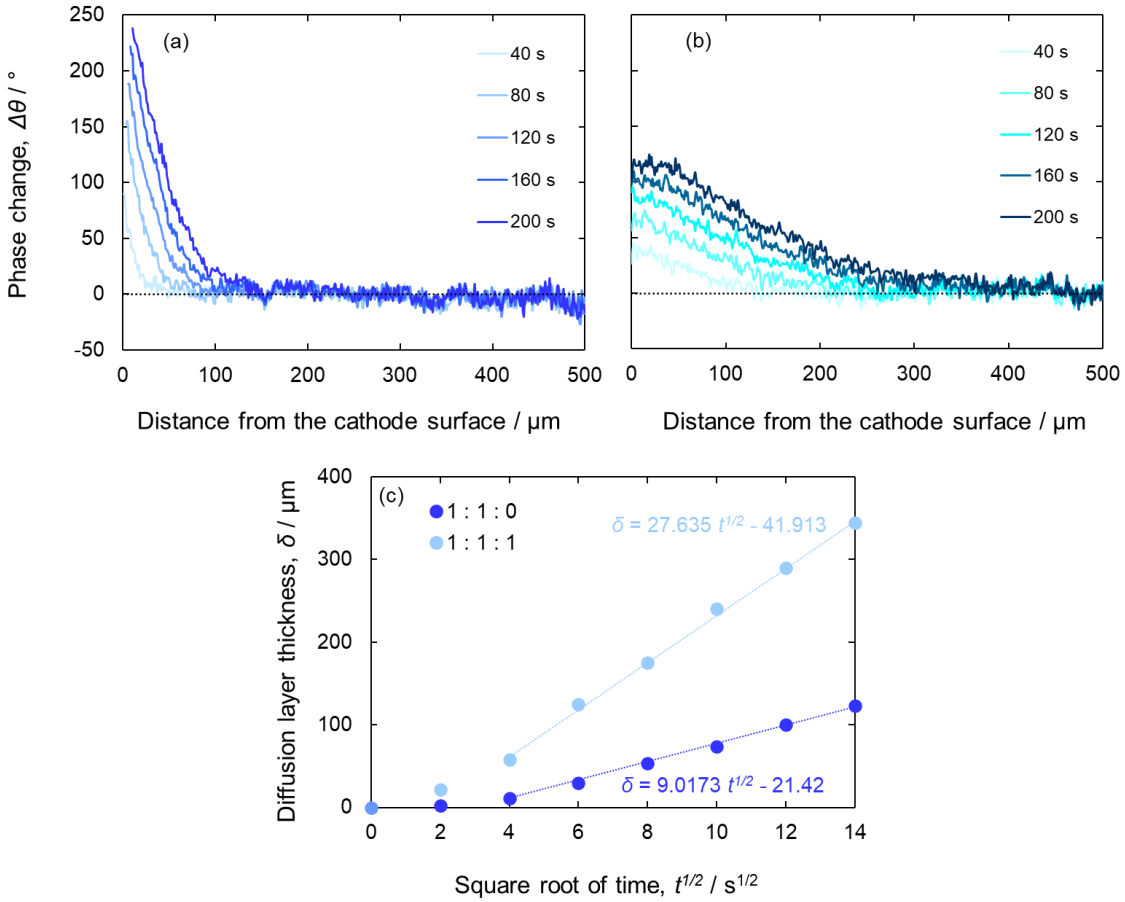

Figure 3. Phase change near the electrode in (a) 1:1:0 and (b) 1:1:1 during electrodeposition at 3 mA cm^{-2}. (c) Time variation of the apparent diffusion layer thickness during electrodeposition.

Figure S1(a) documents concentration changes near the electrode in 1:1:0 during

electrodeposition at 3 mA cm^{-2} from 0 s to 200 s. The interferogram displays the cathode as a mottled region on the left and the electrolyte as a light blue region on the right. The correlation between hologram colors and phase changes is shown in the video. Upon current application, color changes near the electrode signaled decreasing LiFSA concentration due to Li electrodeposition. A concentration gradient developed between the electrode surface and bulk, driving Li^+ diffusion toward the electrode. The diffusion layer, characterized by lower LiFSA concentration than bulk, progressively thickened. Hologram colors within this layer transitioned from light blue (initial state) through green, yellow, and red to blue from bulk to electrode surface, indicating the formation of a LiFSA concentration gradient.[14] We defined the concentration boundary between bulk and diffusion layer as the position where phase change reached 1% of the total change between electrode surface and bulk. After 200 s, the diffusion layer thickness, δ, developed to approximately 120 μm.

Figure S1(b) reveals analogous concentration changes in 1:1:1 under identical conditions. Li electrodeposition initiated upon current application, with LiFSA diffusing from bulk toward the electrode to form a diffusion layer of reduced concentration. The diffusion layer exhibited greater spatial extent in 1:1:1 compared to 1:1:0, reaching $\delta \approx$ 340 μm after 200 s. The $\Delta\theta$ within the diffusion layer was smaller at 1:1:1 than at 1:1:0.

Figure 3(a) depicts the temporal evolution of $\Delta\theta$ near the electrode in 1:1:0 at 3 mA cm^{-2}. $\Delta\theta$ near the electrode increased with deposition time. Figure S1(a) shows the refractive indices of non-HFE solutions at various LiFSA concentrations. When decreasing LiFSA concentration from the equimolar LiFSA-G4 composition, the refractive index increased. The relationship, combined with Eq. 3 and interferometric measurements, demonstrated the reduction in LiFSA concentration near the electrode

during deposition.[14]

Figure 3(b) depicts the temporal evolution of $\Delta\theta$ near the electrode in 1:1:1 at 3 mA cm^{-2}. Similar to 1:1:0, $\Delta\theta$ near the electrode increased with deposition time. LiFSA concentration decreased near the electrode due to Li^+ consumption at the electrode surface. Figure S1(b) shows the refractive indices of HFE-added solutions at various LiFSA concentrations. When decreasing LiFSA concentration while maintaining constant G4 and HFE composition, the refractive index decreased. Figures S1(c)-S1(d) show the refractive indices of HFE-added solutions at various concentrations of (c) G4 or (d) HFE. Increasing only G4 concentration raises the electrolyte refractive index, while increasing only HFE concentration lowers it. As Li^+ is consumed at the electrode surface during electrodeposition, G4 concentration becomes relatively higher than LiFSA concentration. Additionally, Olbrich et al. reported that G4 concentration increases near the cathode during deposition in 1 mol L^{-1} LiFSA-G4 binary electrolyte using in-situ Raman spectroscopy.[26] Both G4 coordinated with Li^+ and uncoordinated G4 exist near the cathode. In this study, G4 concentration may also be increasing near the cathode. These factors likely caused the transient increase in $\Delta\theta$ near the electrode.

Figure 3(c) presents the temporal evolution of δ. In both electrolytes, δ developed gradually until 16 s after deposition initiation. During the initial deposition period, both Cu electrode surface oxide film reduction and Li electrodeposition proceed simultaneously.[12] The δ growth rate accelerated following completion of surface film reduction, subsequently increasing proportionally to the square root of time until observation concluded. The consistently larger δ in 1:1:1 compared to 1:1:0 reflects fundamental differences in mass transport behavior. The apparent diffusion coefficient, D_{app}, can be estimated using the following equation:[12]

$$D_{app} = \frac{\pi}{4} \times \left(\frac{\delta}{\sqrt{t}}\right)^2 \quad (1)$$

where t represents deposition time and the bracketed term corresponds to the slope in the figure. D_{app} can be calculated from the time evolution of δ. Analysis yielded D_{app} values of 1.0×10^{-7} and 6.4×10^{-7} cm^2 s^{-1} for 1:1:0 and 1:1:1, respectively. This difference can be understood through the Stokes-Einstein relationship:[27]

$$D = \frac{RT}{6\pi\eta a} \quad (2)$$

where D denotes the diffusion coefficient, a shows the ionic radius of the Li^+-G4 complex, R is the gas constant, and T is absolute temperature. The η of 1:1:1 was about one sixth part that of 1:1:0. Additionally, HFE does not coordinate with Li^+, and its presence does not affect a.[15] Mixing HFE into the electrolyte significantly improves the diffusion coefficient of LiFSA in the electrolyte.[16] This supports the approximately sixfold difference in D_{app} between the two electrolytes.

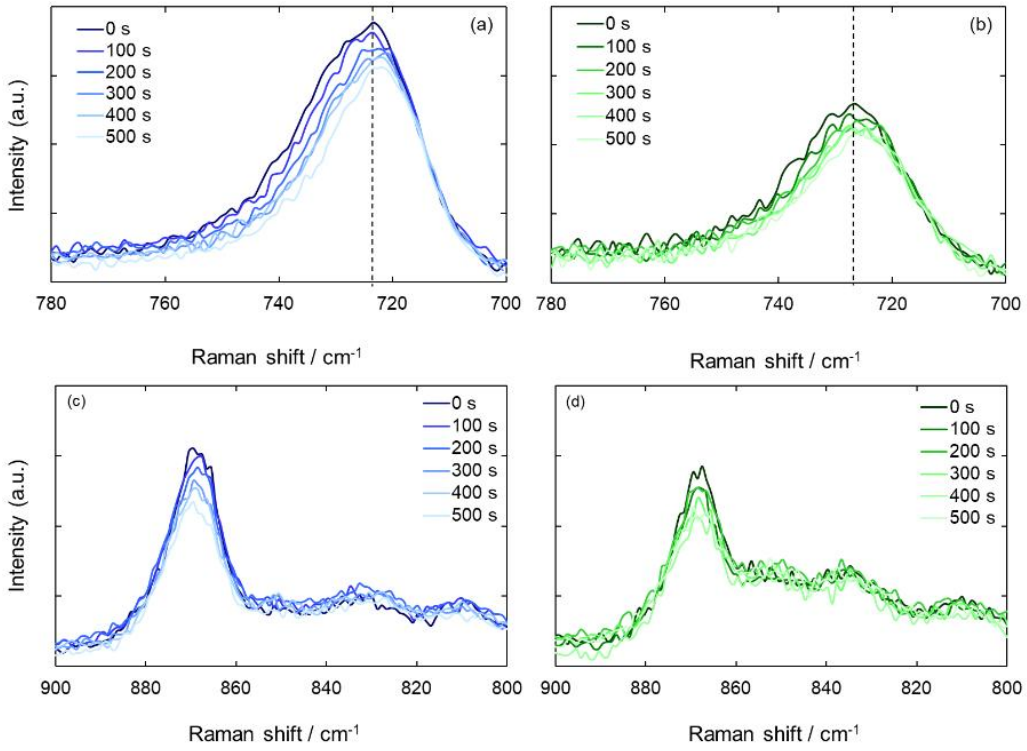

Figure 4. In-situ Raman spectra at 700-780 cm^{-1} obtained near the cathode during electrodeposition at 3 mA cm^{-2} using (a) 1:1:0 and (b) 1:1:1. In-situ Raman spectra at 800-900 cm^{-1} obtained near the cathode during electrodeposition at 3 mA cm^{-2} using (c) 1:1:0 and (d) 1:1:1.

Figure S2(a) presents Raman spectra of non-HFE solutions at 700-780 cm^{-1}. The ratios shown correspond to LiFSA-G4-HFE molar ratios. Previous studies by Yoon et al. identified peaks in the 700-760 cm^{-1} range as characteristic of S-N-S bond stretching vibrations.[28] Specifically, peaks at 720-730 cm^{-1} and 730-750 cm^{-1} correspond to uncoordinated and Li^+-coordinated FSA^-, respectively.[29] Decreasing LiFSA concentration systematically reduced peak intensities while shifting positions toward lower wavenumbers, indicating increased proportions of uncoordinated FSA^-.[14] Figure S2(b) demonstrates Raman spectra of HFE-added solutions at 700-780 cm^{-1}. The spectra

showed peak positions similar to those of the non-HFE solution, and the intensity changed with decreasing LiFSA concentration. Figure S2(c) shows Raman spectra of solutions with various HFE concentrations at 700-780 cm^{-1}. Increasing HFE concentration while maintaining constant LiFSA-G4 molar ratio did not change peak positions, confirming HFE's non-participation in LiFSA-G4 coordination.[30] Peak intensity decreased with increasing HFE content due to reduced LiFSA concentration in the electrolyte.

Figure 4(a) shows in-situ Raman spectra obtained near the cathode during electrodeposition at 3 mA cm^{-2} in 1:1:0 with 800-900 cm^{-1}. Peak intensity decreased and peak position shifted to lower wavenumbers with deposition time, suggesting decreasing LiFSA concentration near the electrode during deposition. Figure 4(b) shows in-situ Raman spectra obtained similarly for 1:1:1. Similar spectral changes were observed with deposition time. Raman spectroscopy confirmed decreasing LiFSA concentration near the electrode during deposition regardless of HFE addition. The peak wavenumber shift was larger in 1:1:0 than in 1:1:1, suggesting greater LiFSA concentration changes in the non-HFE electrolyte during deposition.

Figure S2(d) shows Raman spectra of non-HFE solutions at 800-900 cm^{-1}. As reported by Grondin et al., peaks in this range arise from C-O stretching vibrations.[31] The systematic decrease in 868 cm^{-1} peak intensity with decreasing LiFSA concentration indicates progressive de-solvation of G4 from Li^+.[14,32] Figure S2(e) shows Raman spectra of HFE-added solutions at 800-900 cm^{-1}. Peak intensity decrease due to G4 de-solvation from Li^+ was also observed in HFE-added solutions with decreasing LiFSA concentration.

Figure 4(c) shows in-situ Raman spectra obtained near the cathode during electrodeposition at 3 mA cm^{-2} in 1:1:0 with 800-900 cm^{-1}. Peak intensity at 868 cm^{-1}

decreased with deposition time, suggesting increasing de-solvated G4 with Li^+ near the electrode as LiFSA concentration decreased during deposition. Figure 4(d) shows in-situ Raman spectra obtained similarly for 1:1:1 electrolyte. Peak intensity decrease was also detected with deposition time in 1:1:1, confirming increasing de-solvated G4 near the electrode during deposition.

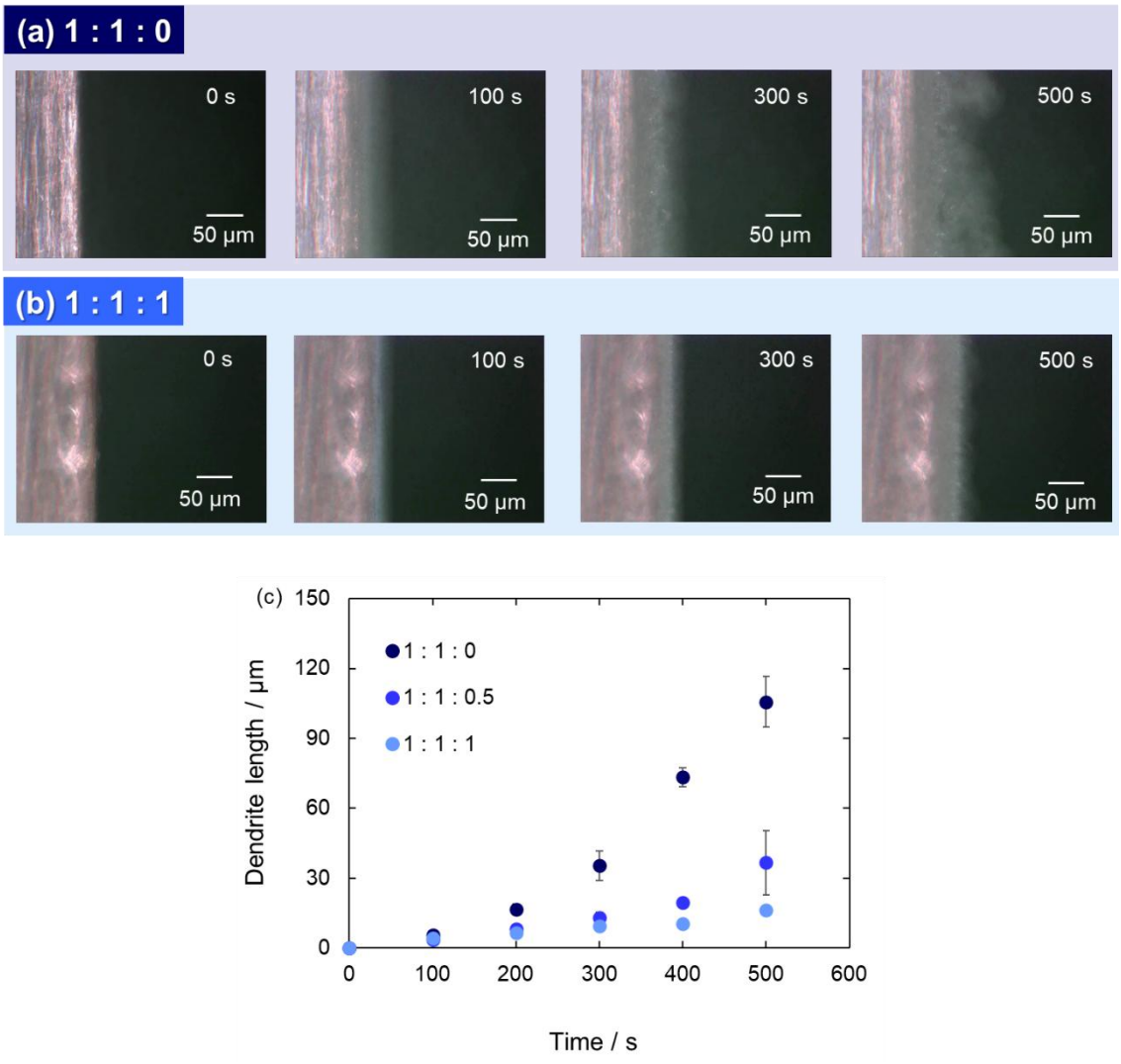

Figure 5. Li electrodeposition in (a) 1:1:0 and (b) 1:1:1 at 3 mA cm^{-2} measured by optical microscopy.

Figure 5(a) shows Li electrodeposition at 3 mA cm^{-2} in 1:1:0 observed by optical microscopy. Initial deposition produced mossy gray deposits that aggregated into a nominally flat layer composed of numerous needle-like structures. [33] After 300 s, as the deposit thickness reached 30 μm, deposit length increased rapidly in localized areas. The video captured deposits growing while swaying left and right in the electrolyte. After 500 s, deposits grew to a maximum length of 105 μm. Due to localized deposit growth, the deposit layer surface became irregular.

Figure 5(b) shows Li electrodeposition at 3 mA cm^{-2} in 1:1:1 observed by optical microscopy. While gray deposits similarly formed upon initiation, individual deposits exhibited larger diameters in 1:1:1 than in 1:1:0. The deposit layer developed uniformly across the electrode surface without significant irregularities. Although some deposits merged after 300 s forming larger structures, these did not continue growing throughout deposition. The final deposit layer reached 15 μm thickness at 500 s, displaying substantially smoother morphology compared to 1:1:0.

Figures S3(a)-S3(b) show Li electrodeposition processes in electrolytes at (a) 1 and (b) 2 mA cm^{-2} observed by optical microscopy, respectively. At both current densities, electrolytes with HFE produced thinner deposit layers with smoother surface morphology compared to those without HFE.

Figure 5(c) quantifies deposit length evolution with time at varying HFE concentrations. 1:1:0 exhibited exponential length increase. Increasing HFE content progressively suppressed deposit growth; final lengths at 500 s measured 106 μm, 37 μm, and 16 μm for 1:1:0, 1:1:0.5, and 1:1:1 compositions, respectively.

Figure S4 illustrates a mechanism for Li electrodeposition in these electrolyte systems. The process initiates with electron transfer to solvated Li^+ at the cathode surface,

inducing de-solvation and subsequent deposition. This consumption establishes a Li^+ concentration gradient between the electrode surface and bulk electrolyte. The gradient drives Li^+ transport through either solvated species conveyance or inter-solvent hopping mechanisms.[13] Upon contact with the deposited metallic Li surface, both anions and solvent molecules undergo partial decomposition to form the SEI layer. [34] Subsequently, solvated Li^+ at the cathode surface loses its coordination structure and deposits on the metallic Li surface through the SEI.

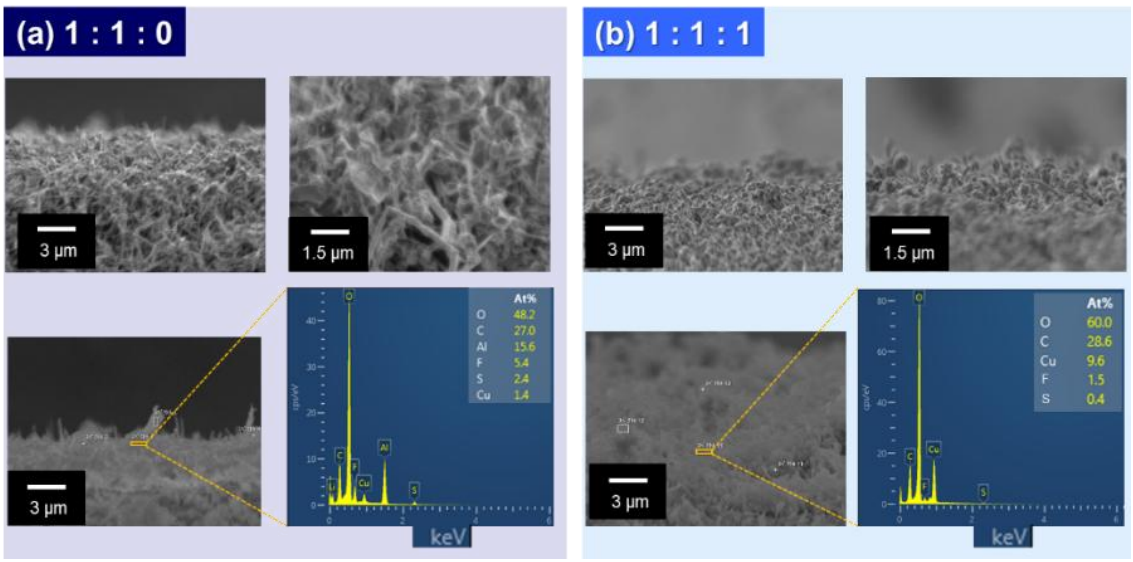

Figure 6. SEM images and EDS spectra of Li deposits in (a) 1:1:0 and (b) 1:1:1 at 3 mA cm^{-2}.

Figure 6 presents SEM images and EDS spectra of deposits formed in both electrolytes. Deposits from 1:1:0 displayed noticeably smaller diameters compared to 1:1:1. EDS analysis detected four elements (O, C, F, and S) in deposits from both electrolytes. O originated from both FSA^- and G4, C from G4, and F and S from FSA^-, indicating deposit surfaces were covered with SEI layers formed through decomposition

of these species.[35]

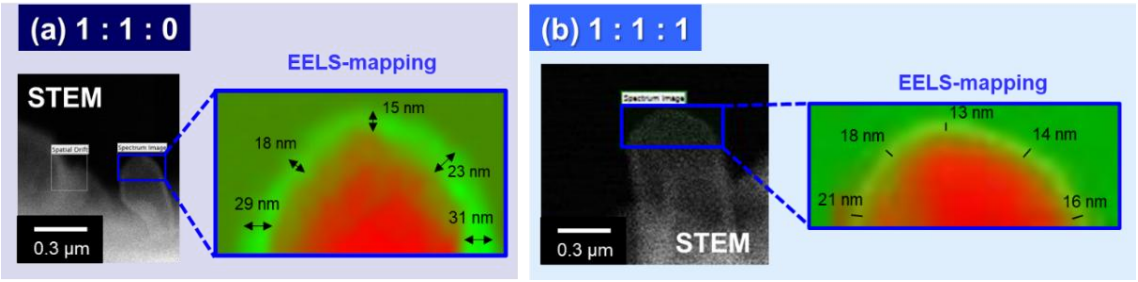

Figure 7. STEM and EELS mapping images of Li deposits in (a) 1:1:0 and (b) 1:1:1 at 3 mA cm^{-2}.

Figure 7 provides STEM images and EELS mapping of the deposits. The red and green regions represent metallic Li and SEI layers, respectively. Both electrolytes produced deposits with minimum SEI thickness at their tips, but overall thickness distributions differed significantly: 15-31 nm in 1:1:0 versus 13-21 nm in 1:1:1. The difference between tip and side SEI thickness was markedly larger in 1:1:0 than in 1:1:1.

Figures S5(a)-S5(b) show EELS line spectra obtained from deposit tips. Both spectra showed distinct peaks at 55, 58.5, and 63.2 eV, attributed to metallic Li and Li_2O.[36] This revealed Li_2O as one of the SEI constituent compounds. This is consistent with EDS measurements. Here, SEI thickness is defined as the distance from where the metallic Li peak disappears to where the Li_2O peak vanishes.[12] These thicknesses were 25 nm (1:1:0) and 15 nm (1:1:1), confirming that HFE addition to the electrolyte results in thinner SEI.[18]

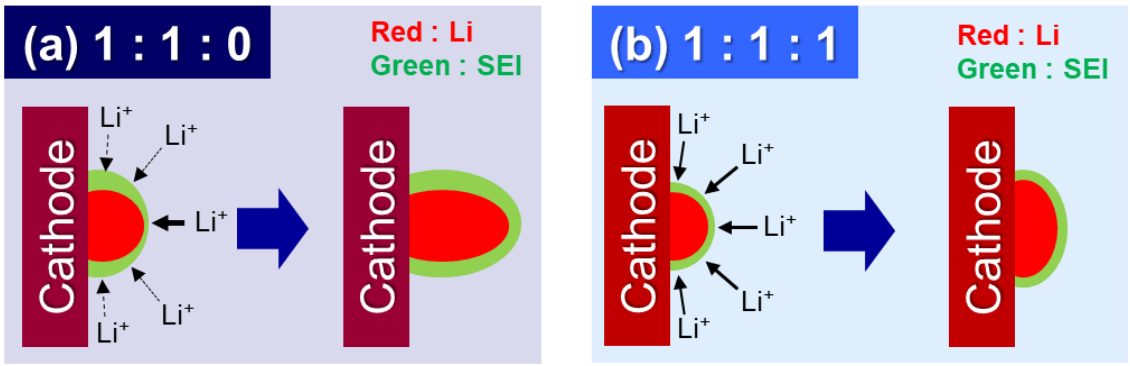

Figure 8. Schematic of Li electrodeposition in (a) 1:1:0 and (b) 1:1:1.

Figure 8(a) illustrates the Li deposition mechanism in 1:1:0. Thicker SEI formed in 1:1:0 compared to 1:1:1. The SEI was 16 nm thicker at deposit tips than sides. The rate of Li^+ transport through SEI decreases with increasing SEI thickness.[37] Consequently, Li^+ supply was faster at deposit tips than sides, leading to preferential tip-directed growth and formation of deposits with thin stems. Li deposited in a moss-like morphology in 1:1:0. The rough, porous deposit surface likely disturbed Li^+ diffusion flux from the bulk, creating localized Li^+ concentration variations in the electrolyte near the surface. Deposits grew locally in Li^+-rich regions, resulting in an increasingly irregular deposit layer.

Figure 8(b) depicts the Li deposition mechanism in 1:1:1. The SEI thickness difference between deposit tips and sides was 8 nm. Therefore, the difference in Li^+ transport rates through SEI between tips and sides was smaller in 1:1:1 than in 1:1:0. This enables growth in both tip and lateral directions, producing thicker stems. The deposit surface had fewer irregularities and voids in 1:1:1 than in 1:1:0. Consequently, Li^+ flux from bulk to electrode surface remained undisturbed, reaching the deposit surface uniformly. This likely prevented localized Li^+ concentration variations along the electrode surface. The uniform Li^+ supply across the deposit surface resulted in smooth, thin deposit morphology.

Murai et al. demonstrated that increased concentration polarization enhances decomposition reactions of anions and solvent molecules.[38] Such enhanced side reactions produce thicker SEI layers.[12,39] The magnitude of concentration polarization varies inversely with D_{app} in the electrolyte. Indeed, the absolute cell voltage during deposition was lower in 1:1:1 than in 1:1:0. Additionally, there was a sixfold difference in D_{app} between 1:1:0 and 1:1:1. Consequently, side reactions at the deposit surface were suppressed more in 1:1:1 than in 1:1:0. Furthermore, 1:1:1 contained less FSA^- and G4 than 1:1:0, resulting in fewer decomposition reactions of these species. These factors likely contributed to thinner SEI formation in 1:1:1.

6.4 Conclusion

This research elucidated the effects of HFE addition on Li^+ transport and deposit morphology through combined laser interferometry and microscopic analyses. In HCEs, low apparent Li^+ diffusion coefficients led to enhanced side reactions and thick SEI formation, particularly on deposit sides, promoting preferential tip growth that produced long, pointed deposits. Conversely, LHCEs exhibited higher apparent Li^+ diffusion coefficients, suppressing side reactions and forming thin, uniform SEI layers. This resulted in shorter deposits with rounded tips, lacking the pronounced tip-directed growth observed in HCEs. In future work, we will use atomic force microscopy[40] to conduct in-situ observations of Li nucleation processes in HCEs and LHCEs. We aim to elucidate the essence of Li deposition mechanisms by analyzing nuclei morphology and numbers.

6.5 Additional experiments

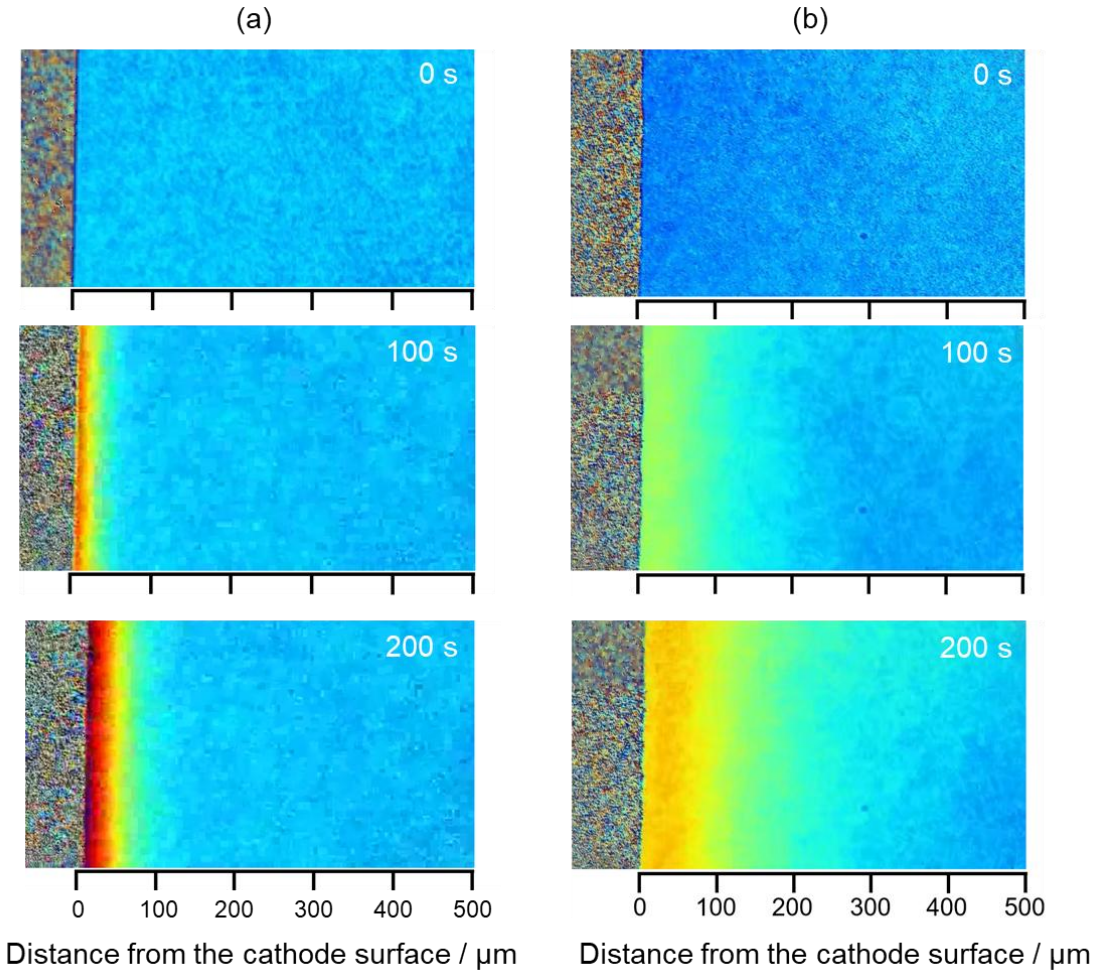

Figure S1. Phase change observation in (a) 1:1:0 and (b) 1:1:1 using in-situ interferometry.

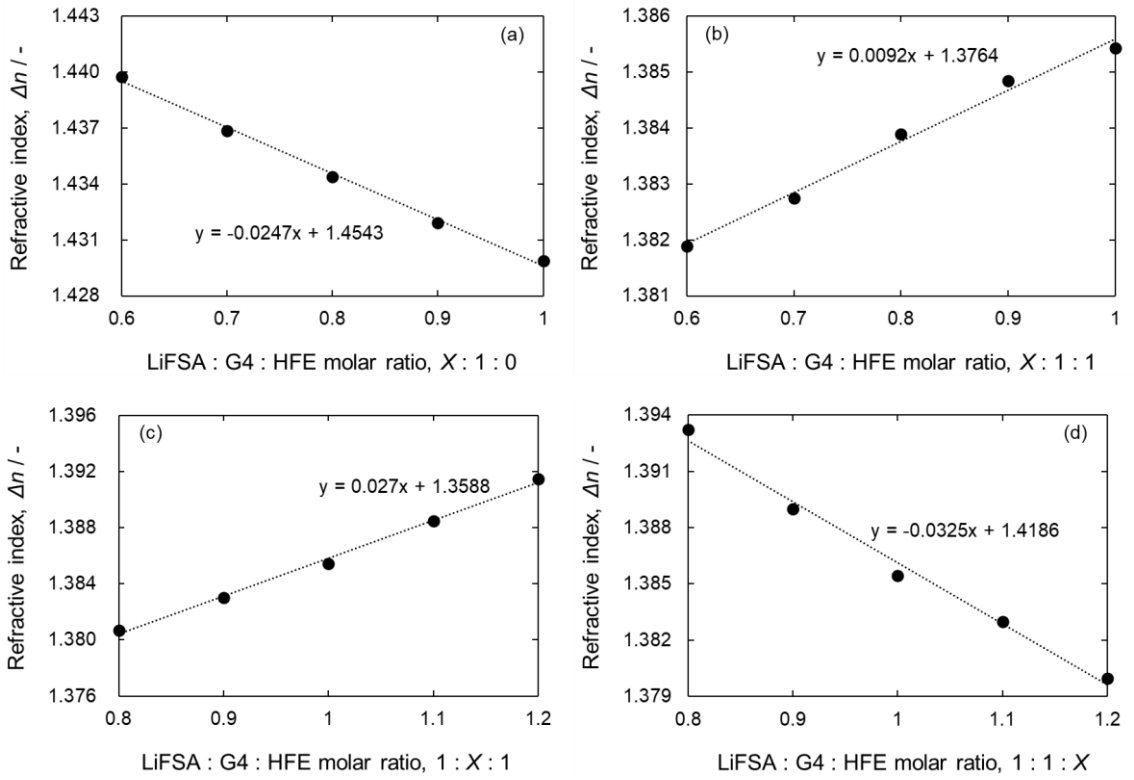

Figure S2. Refractive index of the electrolyte. (a) Non-HFE solutions at various LiFSA concentrations. HFE-added solutions at various (b) LiFSA, (c) G4, and (d) HFE concentrations.

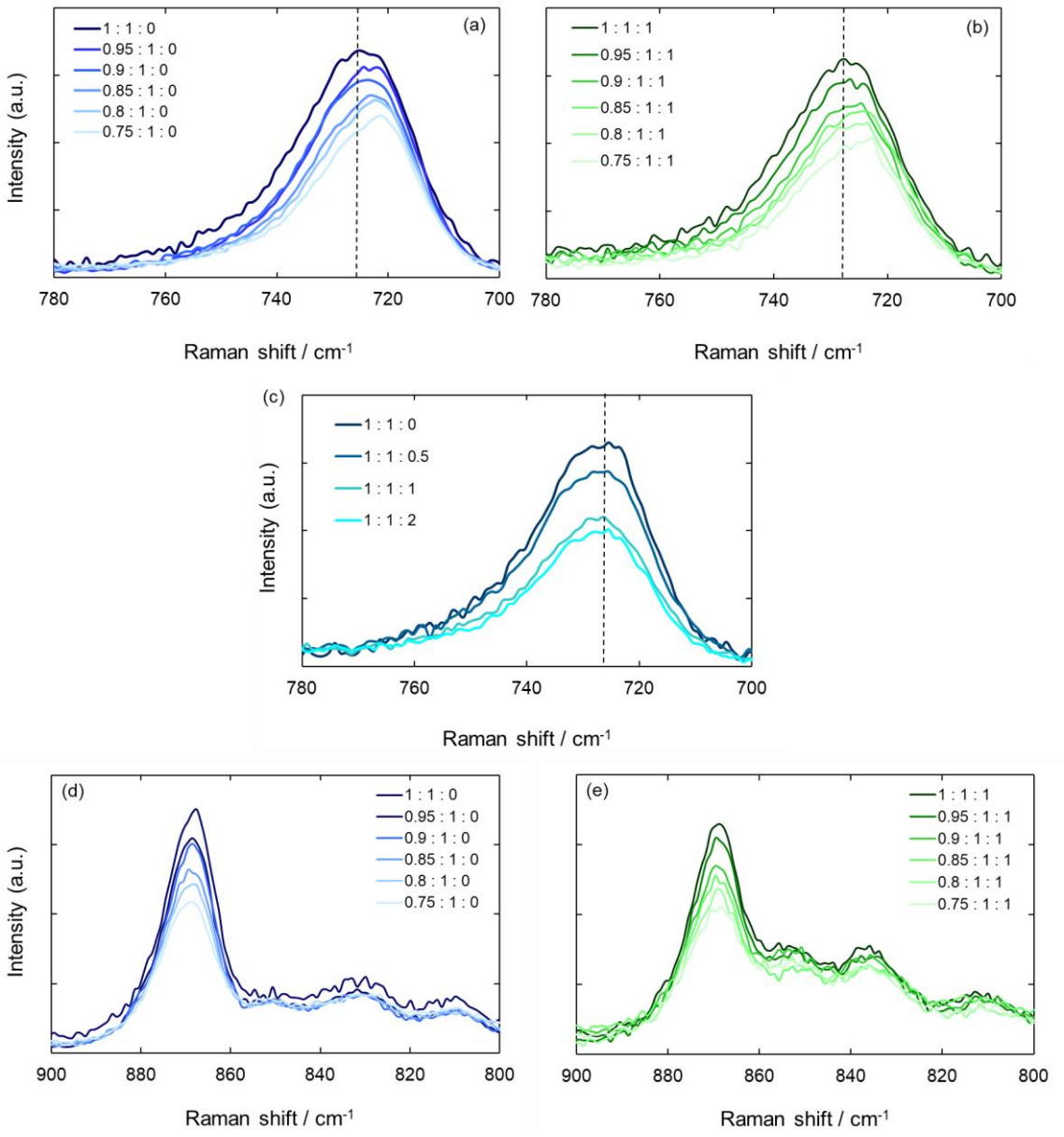

Figure S3. Raman spectra of solutions at 700-780 cm^{-1} (a) without HFE, (b) with HFE, and (c) various HFE concentrations. Raman spectra of solutions at 800-900 cm^{-1} (d) without HFE and (e) with HFE.

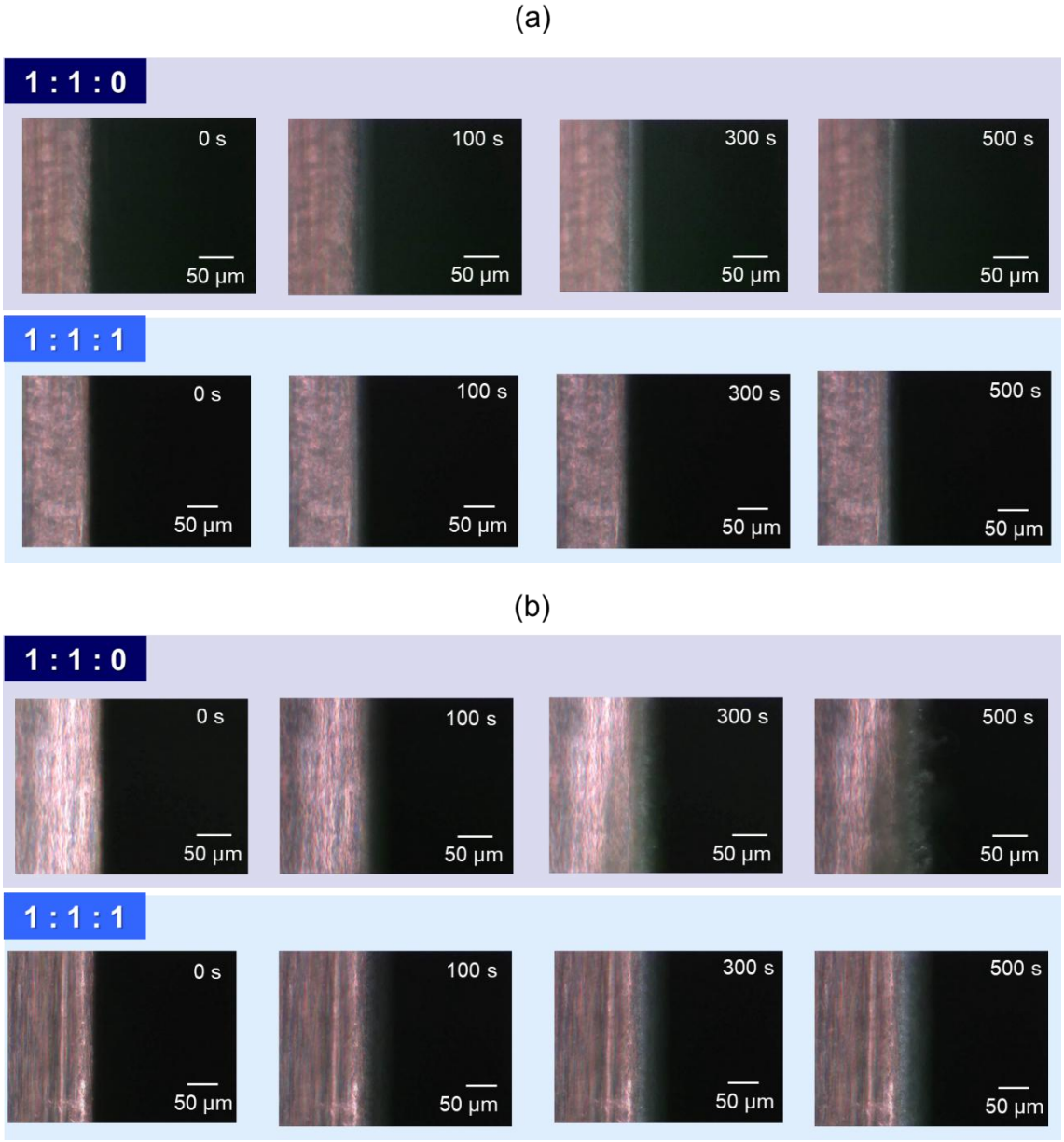

Figure S4. Li electrodeposition in 1:1:0 or 1:1:1 at (a) 1 or (b) 2 mA cm^{-2} measured by optical microscopy.

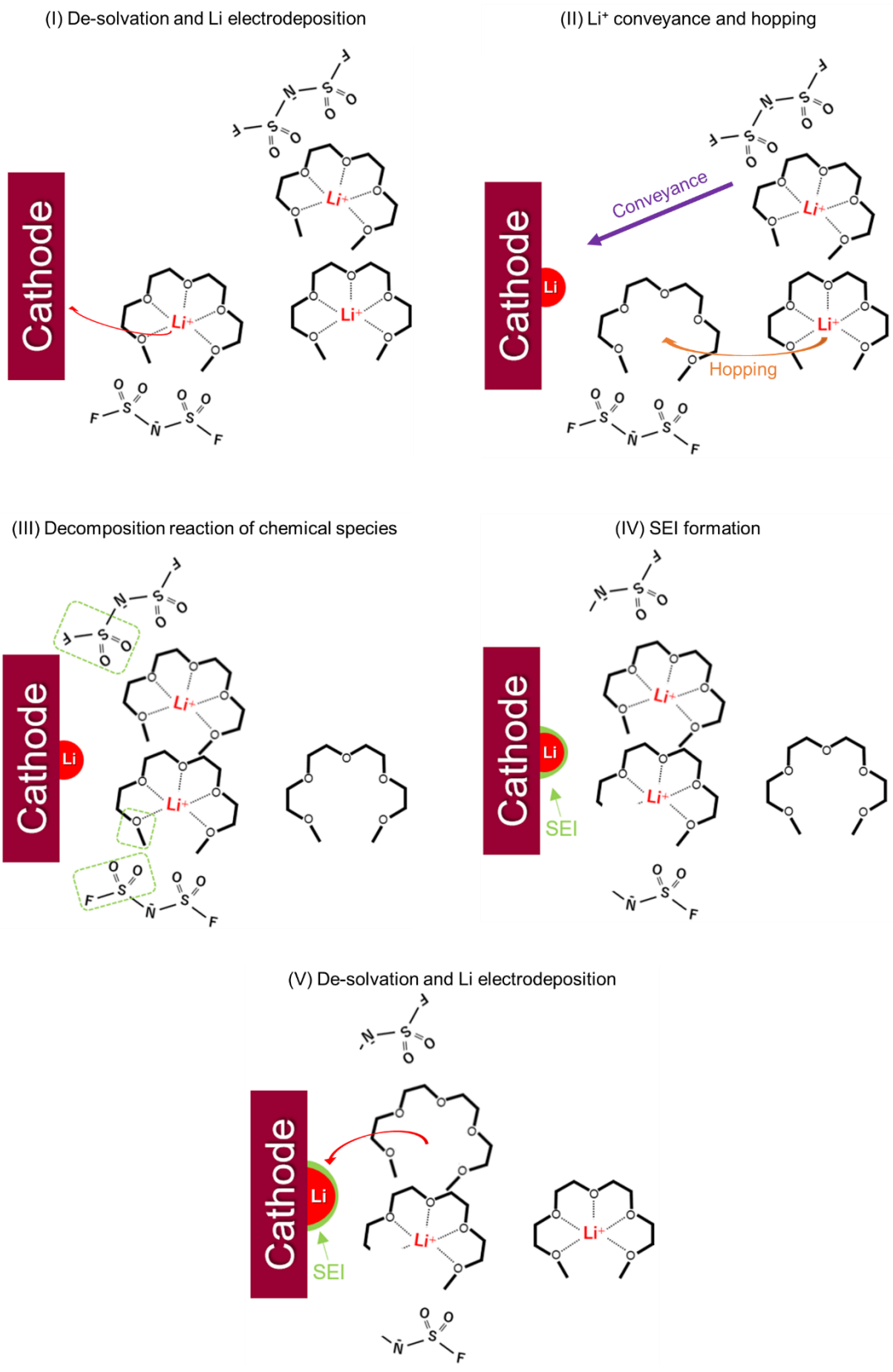

Figure S5. Schematic of the process of Li electrodeposition in electrolyte.

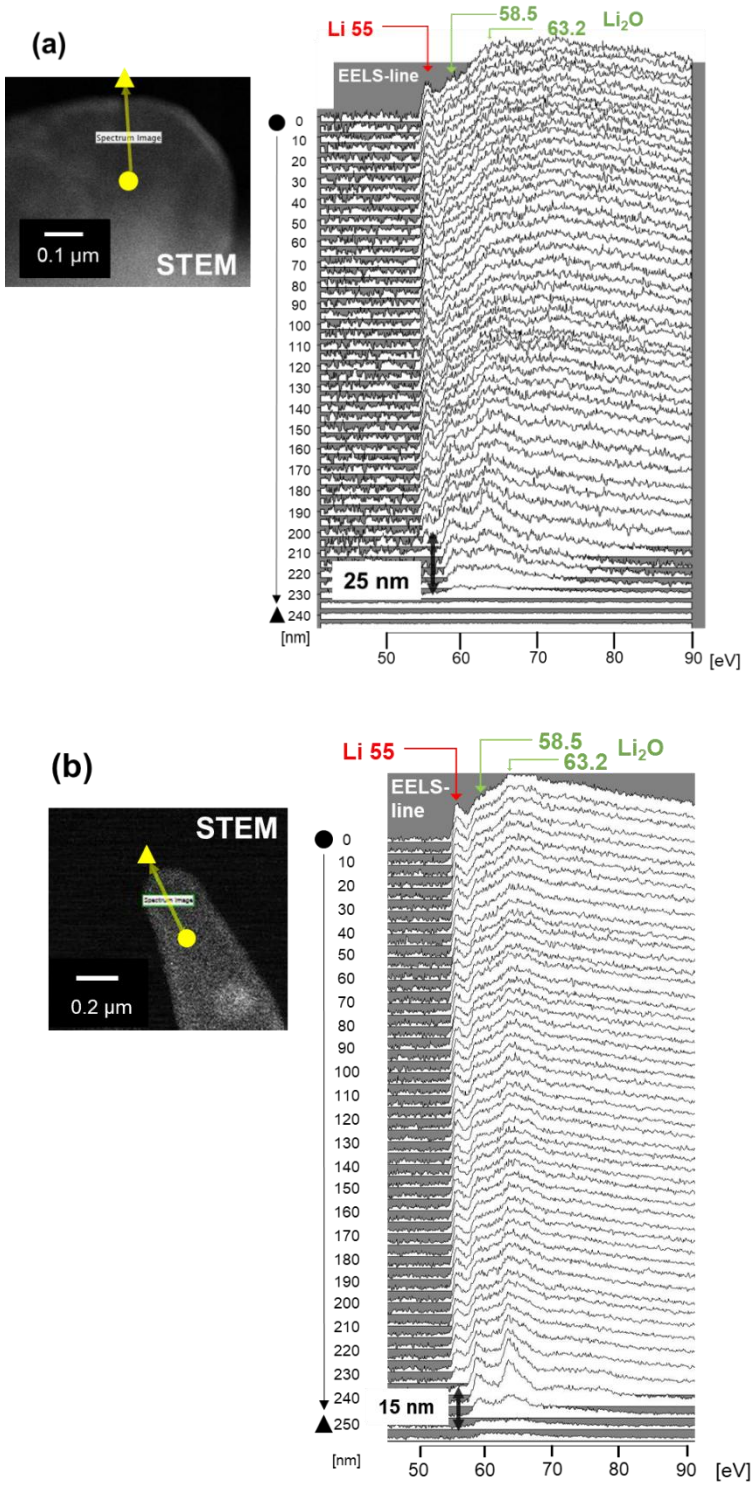

Figure S6. STEM image and EELS-line spectra of Li deposits in (a) 1:1:0 and (b) 1:1:1.

References

[1] M. Li, J. Lu, Z. Chen, K. Amine, *Advanced Materials* **2018**, *30*, 1800561.

[2] J. W. Choi, D. Aurbach, *Nature reviews materials* **2016**, *1*, 1–16.

[3] Y. Yamada, K. Furukawa, K. Sodeyama, K. Kikuchi, M. Yaegashi, Y. Tateyama, A. Yamada, *J. Am. Chem. Soc.* **2014**, *136*, 5039–5046.

[4] O. Borodin, J. Self, K. A. Persson, C. Wang, K. Xu, *Joule* **2020**, *4*, 69–100.

[5] X. Cao, H. Jia, W. Xu, J.-G. Zhang, *Journal of The Electrochemical Society* **2021**, *168*, 010522.

[6] J.-G. Zhang, W. Xu, J. Xiao, X. Cao, J. Liu, *Chem. Rev.* **2020**, *120*, 13312–13348.

[7] M. R. Busche, T. Drossel, T. Leichtweiss, D. A. Weber, M. Falk, M. Schneider, M.-L. Reich, H. Sommer, P. Adelhelm, J. Janek, *Nature chemistry* **2016**, *8*, 426–434.

[8] Y. Xiao, R. Xu, L. Xu, J.-F. Ding, J.-Q. Huang, *Energy Mater* **2021**, *1*, 100013.

[9] Q. Wang, B. Liu, Y. Shen, J. Wu, Z. Zhao, C. Zhong, W. Hu, *Advanced Science* **2021**, *8*, 2101111.

[10] C. Fang, X. Wang, Y. S. Meng, *Trends in Chemistry* **2019**, *1*, 152–158.

[11] K. Nishikawa, T. Mori, T. Nishida, Y. Fukunaka, M. Rosso, *Journal of electroanalytical chemistry* **2011**, *661*, 84–89.

[12] G. Kamesui, K. Nishikawa, M. Ueda, H. Matsushima, *ACS Energy Lett.* **2022**, *7*, 4089–4097.

[13] K. Dokko, D. Watanabe, Y. Ugata, M. L. Thomas, S. Tsuzuki, W. Shinoda, K. Hashimoto, K. Ueno, Y. Umebayashi, M. Watanabe, *J. Phys. Chem. B* **2018**, *122*, 10736–10745.

[14] G. Kamesui, K. Nishikawa, M. Ueda, H. Matsushima, *Journal of The Electrochemical Society* **2024**, *171*, 040519.

[15] S. Chen, J. Zheng, D. Mei, K. S. Han, M. H. Engelhard, W. Zhao, W. Xu, J. Liu, J. Zhang, *Advanced Materials* **2018**, *30*, 1706102.

[16] Y. Watanabe, Y. Ugata, K. Ueno, M. Watanabe, K. Dokko, *Physical Chemistry Chemical Physics* **2023**, *25*, 3092–3099.

[17] W. Dai, N. Dong, Y. Xia, S. Chen, H. Luo, Y. Liu, Z. Liu, *Electrochimica Acta* **2019**, *320*, 134633.

[18] F. Guo, X. Chen, Y. Hou, W. Wei, Z. Wang, H. Yu, J. Xu, *Small* **2023**, *19*, 2207290.

[19] X. Ren, S. Chen, H. Lee, D. Mei, M. H. Engelhard, S. D. Burton, W. Zhao, J. Zheng, Q. Li, M. S. Ding, M. Schroeder, J. Alvarado, K. Xu, Y. S. Meng, J. Liu, J.-G. Zhang, W. Xu, *Chem* **2018**, *4*, 1877–1892.

[20] Z. Wang, F. Zhang, Y. Sun, L. Zheng, Y. Shen, D. Fu, W. Li, A. Pan, L. Wang, J. Xu, J. Hu, X. Wu, *Advanced Energy Materials* **2021**, *11*, 2003752.

[21] F. R. McLarnon, R. H. Muller, C. W. Tobias, *JOSA* **1975**, *65*, 1011–1018.

[22] K. Nishikawa, T. Saito, H. Matsushima, M. Ueda, *Electrochimica Acta* **2019**, *297*, 1104–1108.

[23] G. Kamesui, K. Nishikawa, M. Ueda, H. Matsushima, *Electrochemistry Communications* **2023**, *151*, 107506.

[24] G. Kamesui, K. Nishikawa, M. Ueda, H. Matsushima, *Journal of The Electrochemical Society* **2024**, *171*, 100507.

[25] A. A. Wang, A. B. Gunnarsdóttir, J. Fawdon, M. Pasta, C. P. Grey, C. W. Monroe, *ACS Energy Lett.* **2021**, *6*, 3086–3095.

[26] L. F. Olbrich, B. Jagger, J. Ihli, M. Pasta, *ACS Energy Lett.* **2024**, *9*, 3636–3642.

[27] J. Newman, N. P. Balsara, *Electrochemical Systems*, John Wiley & Sons, **2021**.

[28] H. Yoon, A. S. Best, M. Forsyth, D. R. MacFarlane, P. C. Howlett, *Phys. Chem.*

Chem. Phys. **2015**, *17*, 4656–4663.

[29] K. Fujii, H. Hamano, H. Doi, X. Song, S. Tsuzuki, K. Hayamizu, S. Seki, Y. Kameda, K. Dokko, M. Watanabe, Y. Umebayashi, *J. Phys. Chem. C* **2013**, *117*, 19314–19324.

[30] A. Nakanishi, K. Ueno, D. Watanabe, Y. Ugata, Y. Matsumae, J. Liu, M. L. Thomas, K. Dokko, M. Watanabe, *J. Phys. Chem. C* **2019**, *123*, 14229–14238.

[31] J. Grondin, J.-C. Lassègues, M. Chami, L. Servant, D. Talaga, W. A. Henderson, *Phys. Chem. Chem. Phys.* **2004**, *6*, 4260–4267.

[32] A. Miki, K. Nishikawa, G. Kamesui, H. Matsushima, M. Ueda, M. Rosso, *Journal of Materials Chemistry A* **2021**, *9*, 14700–14709.

[33] P. Bai, J. Li, F. R. Brushett, M. Z. Bazant, *Energy & Environmental Science* **2016**, *9*, 3221–3229.

[34] D. Cao, C. Tan, Y. Chen, *Nature Communications* **2022**, *13*, 4908.

[35] Y. Liu, Y. Huang, X. Xu, Y. Liu, J. Yang, J. Lai, J. Shi, S. Wang, W. Fan, Y. Cai, Y. Lan, Q. Zheng, *Adv Funct Materials* **2023**, *33*, 2303667.

[36] K. Nishikawa, K. Shinoda, *J. Phys. Chem. Lett.* **2021**, *12*, 3922–3927.

[37] S. Das, P. M. Attia, W. C. Chueh, M. Z. Bazant, *Journal of The Electrochemical Society* **2019**, *166*, E107–E118.

[38] J. Murai, T. Ishikawa, G. Wada, K. Dokko, M. Watanabe, K. Ueno, *ChemElectroChem* **2024**, *11*, e202400054.

[39] X. Du, B. Zhang, *ACS Nano* **2021**, *15*, 16851–16860.

[40] R. Ohashi, M. Ueda, H. Matsushima, *Electrochemical Science Adv* **2024**, e202400008.

Chapter 7 General Conclusions

7.1 General conclusion

The present study has elucidated the lithium electrodeposition mechanisms in electrolytes through the utilization of various in-situ observation techniques, with particular emphasis on laser interferometry. The interferometric methodology facilitates non-destructive observations of concentration distributions with exceptional temporal resolution, whilst minimizing perturbation of the specimen through the implementation of low-energy laser irradiation. The correlation between mass transfer and deposit morphology was comprehensively characterised through the synergistic application of real-time digital microscopy for electrodeposition observation and scanning electron microscopy for microstructural analyses. The principal findings may be summarised as follows:

In Chapter 2, investigations were conducted into the mass transfer phenomena accompanying lithium electrodeposition and dissolution in highly concentrated electrolytes. Quantitative evaluations of concentration variations in the vicinity of the electrode revealed a pronounced dependence of deposit morphology on current density. Of particular significance was the observation that solid-electrolyte interphase (SEI) formation at the electrode surface exhibited governing influence over the deposition morphology, with systematic analyses establishing correlations between SEI thickness and resultant morphological characteristics. During dissolution at elevated current densities, supersaturation at the electrode surface was found to induce potential divergence. These observations not only suggest the feasibility of morphological control through current density optimisation but also provide critical insights into the reaction mechanisms operative during rapid charge-discharge processes.

In Chapter 3, laser interferometry was employed to observe the formation and

relaxation processes of concentration gradients in solvate ionic liquids. Successful measurements of concentration distributions were achieved at an inter-electrode distance of 600 μm, closely approximating actual battery conditions. These measurements revealed distinct diffusion coefficients between the anodic and cathodic regions, with the disparity being attributed to variations in electrolyte viscosity. Detailed analyses of the relaxation processes following current interruption elucidated the significant influence of concentration-dependent diffusion coefficients on relaxation behaviour.

In Chapter 4, comprehensive analyses were performed on mass transfer phenomena during current reversal. The formation of characteristic concentration profiles in the immediate aftermath of reversal was discovered and subsequently validated through finite difference method simulations. Moreover, Raman spectroscopic analyses established quantitative correlations between lithium ion solvation structures and transference numbers, thereby providing fundamental insights into ion transport mechanisms.

In Chapter 5, systematic investigations were conducted into the correlation between electrolyte concentration and deposit morphology. The molar ratio of salt to solvent was found to be determinative of the deposited layer thickness, leading to the theoretical proposition of three distinct deposition growth models contingent upon electrolyte concentration. The growth processes of deposits were meticulously tracked through the complementary application of in-situ digital microscopy and electron microscopic analyses of microstructures. Furthermore, evaluations of morphological evolution during repeated charge-discharge cycles yielded crucial guidelines for electrolyte design optimisation.

In Chapter 6, investigations focused on the effects of dilution with low dielectric

solvents. Quantitative analyses demonstrated that dilution resulted in decreased electrolyte viscosity and enhanced apparent diffusion coefficients of lithium ions. The combined application of laser interferometry and Raman spectroscopy facilitated comprehensive analyses of dilution effects on solvation structures and mass transfer characteristics. Additionally, suppression of interfacial side reactions was observed to promote more uniform deposition morphology. The implications of electrolyte property modifications through dilution on battery performance were thoroughly examined through both electrochemical measurements and structural analyses.

The experimental methodologies established and fundamental understanding gained through this investigation provide a significant foundation for the development of high-energy-density batteries utilising lithium metal anodes. In particular, the controlled manipulation of deposition morphology through electrolyte composition optimisation shows considerable promise for the suppression of dendritic growth and enhancement of long-term battery stability. Furthermore, the laser interferometric technique developed herein for concentration distribution measurements demonstrates broad applicability to mass transfer analyses in diverse electrochemical systems, thereby contributing to the fundamental understanding of electrochemical processes.

7.2 Future prospects

This research has established foundational insights into lithium electrodeposition mechanisms and mass transport phenomena in advanced electrolytes, illuminating a path toward transformative developments in energy storage technology. The laser interferometric methodology developed herein represents a significant advancement in our ability to observe and understand electrochemical processes in real-time, offering

possibilities for studying diverse electrochemical processes critical to next-generation energy storage systems.

For lithium-sulfur, all-solid-state, and lithium-air batteries, our understanding of mass transport phenomena and interfacial interactions could enable unprecedented control over electrochemical processes. The laser interferometric techniques could be adapted to study various electrochemical systems, offering insights into ion transport at solid-solid interfaces and complex electrode reactions. Integration of artificial intelligence with these interferometric techniques could enable predictive control of electrodeposition processes, maximizing efficiency while minimizing degradation.

Intriguingly, the pursuit of harmony between powerful yet potentially hazardous energy systems mirrors ancient Japanese wisdom embodied in the concept of "aramitama" and "nigimitama" - the dual aspects of kami's spirit representing both raw power and controlled beneficence. Just as ancient Japanese people developed sophisticated approaches to harness and live harmoniously with natural forces, this research seeks to control and optimize the powerful electrochemical processes within batteries. Like the ancient craftsmen who learned to work with natural materials by understanding their inherent properties, our investigation reveals the fundamental behaviors of ions and electrolytes to achieve optimal performance, reflecting the Japanese cultural value of seeking balance and harmony in all things.

The implications of this research extend far beyond conventional energy storage, potentially catalyzing a fundamental restructuring of human civilization. In the near term, advances in battery technology could enable a complete transition to renewable energy within a generation, eliminating energy poverty worldwide. The development of microscale energy storage systems could lead to self-powered medical implants that

continuously monitor and regulate body functions, potentially extending human lifespans by decades. Neural interfaces powered by these advanced batteries could restore mobility to paralyzed individuals and enhance human cognitive capabilities, blurring the line between biological and technological enhancement.

In urban environments, the integration of high-density energy storage could transform cities into living organisms of sorts, with buildings that breathe and adapt to environmental conditions. Imagine cities where every surface doubles as an energy harvester and storage medium, where the very walls of buildings incorporate advanced battery systems that learn and adapt to usage patterns. The massive energy storage capacity could enable atmospheric carbon capture at unprecedented scales, potentially reversing centuries of environmental damage within decades. The democratization of energy through advanced storage technologies could reshape global power structures, potentially eliminating energy-based geopolitical conflicts. Communities could become truly autonomous, managing their own microgrids powered by renewable sources and stabilized by next-generation batteries.

The implications of this research extend beyond terrestrial applications into the realm of space exploration. In microgravity conditions, where natural convection is absent, the insights gained regarding diffusion-controlled processes become particularly valuable for developing specialized batteries for satellites, space stations, and deep-space missions. High-energy-density batteries could power personal spacecraft for recreational space tourism, making orbital experiences accessible to ordinary citizens. Long-duration energy storage could enable permanent human settlements on Mars and beyond, while advanced interferometric techniques developed in this research could be adapted for real-time monitoring of life support systems in space habitats.

Looking even further ahead, these technologies could enable the development of planet-scale energy networks, where power can be instantaneously transferred anywhere on Earth through quantum entanglement-based energy transmission systems. The possibility of storing and transmitting massive amounts of energy could allow humanity to harness the power of astronomical phenomena, perhaps even capturing energy from solar flares or utilizing the electromagnetic fields of black holes. Most profoundly, this research contributes to humanity's grand project of becoming a Type I civilization on the Kardashev scale - a civilization capable of utilizing and storing all available energy on its planet.

The integration of these technologies with artificial intelligence could lead to self-evolving energy systems that anticipate and adapt to human needs before we're even aware of them. Cities could become living entities that breathe and pulse with the rhythm of human activity, automatically adjusting their energy consumption and storage patterns to optimize human wellbeing and environmental health. This future is not just about better batteries - it's about better lives, better societies, and ultimately, a better relationship between humanity and the cosmos we inhabit.

The long-term impact of this research extends far beyond the immediate technological implications, pointing toward a fundamental transformation in humanity's relationship with energy and our place in the universe. The enhanced understanding of electrochemical processes at the molecular level provides a foundation not just for better batteries, but for a reimagining of how we might live in harmony with both our planet and the cosmos. As these technologies mature, they promise to enable a society where sustainable energy is as ubiquitous as air, where the distinction between energy consumer and producer blurs, and where communities are empowered to manage their own energy

destinies. As we look toward the stars while keeping our feet firmly planted on Earth, this research represents more than just scientific advancement—it embodies humanity's aspiration to grow beyond our current limitations while preserving the delicate balance that sustains life on our planet. This harmonious integration of progress and preservation, of innovation and sustainability, may well be the key to ensuring that our species not only survives but flourishes in the centuries to come.

Appendices

Papers

1. **Mass Transfer during Electrodeposition and Dissolution of Li Metal within Highly Concentrated Electrolytes**

   Go Kamesui, Kei Nishikawa, Hisayoshi Matsushima and Mikito Ueda

   ACS Energy Letters. **7**, 4089-4097 (2022)

2. **In situ observation of the formation and relaxation processes of concentration gradients in a lithium bis(fluorosulfonyl) amide–tetraglyme solvate ionic liquid using digital holographic interference microscopy**

   Go Kamesui, Kei Nishikawa, Mikito Ueda and Hisayoshi Matsushima

   Electrochemistry Communications. **151**, 107506 (2023)

3. **Elucidation of Mass Transport Phenomena in Highly Concentrated Electrolytes during Current Cycling Using In-Situ Interferometry and Finite Difference Method**

   Go Kamesui, Kei Nishikawa, Mikito Ueda and Hisayoshi Matsushima

   Journal of the Electrochemical Society. **171**, 4, 040519 (2024)

4. **Correlation between Electrolyte Concentration and Lithium Morphology during Lithium Bis(fluorosulfonyl)amide–Tetraglyme Electrolyte Deposition–Dissolution Reactions**

   Go Kamesui, Kei Nishikawa, Mikito Ueda and Hisayoshi Matsushima

   Journal of the Electrochemical Society. **171**, 10, (2024)

5. **The Relationship between Dilution Effects and Mass Transport in Highly Concentrated Electrolytes: Impact on Lithium Electrodeposition Morphology**

   Go Kamesui, Kei Nishikawa, Mikito Ueda and Hisayoshi Matsushima

   Journal of the Electrochemical Society (Submitted)

Presentations

6. **Measurement of concentration profile near the electrode during lithium electrodeposition in high-concentration electrolytes**

   Go Kamesui, Kei Nishikawa, Mikito Ueda and Hisayoshi Matsushima

   2023 Joint Summer Session of both the Japan Institute of Metals and the Japan Iron and Steel Institute, Hokkaido Branch (Poster Presentation)

7. **Measurement of concentration profile in solvated ionic liquids and calculation of the Li^+ transference numbers during electrochemical reactions using interferometry**

   Go Kamesui, Kei Nishikawa, Mikito Ueda and Hisayoshi Matsushima

   2023 Autumn meeting of the Electrochemical Society of Japan (oral presentation)

8. **In-Situ Observation of the Formation and Relaxation Processes of Concentration Gradients in a Lithium Bis(fluorosulfonyl) Amide–Tetraglyme Solvate Ionic Liquid Using Digital Holographic Interference Microscopy**

   Go Kamesui, Kei Nishikawa, Mikito Ueda and Hisayoshi Matsushima

   244th ECS Meeting (Poster Presentation)

9. **Measurement of concentration profile in electrolyte with applied current reversal using interferometry and finite difference methods**

   Go Kamesui, Kei Nishikawa, Mikito Ueda and Hisayoshi Matsushima

   The 65th Battery Symposium in Japan (Oral Presentation)

Others

10. In Situ Observation of Cu^{2+} Concentration Profile During Cu Dissolution in Magnetic Field

Go Kamesui, Kei Nishikawa, Mikito Ueda and Hisayoshi Matsushima

Journal of the Electrochemical Society. **168**, 031507 (2021)

11. In-situ interferometry study of ionic mass transfer phenomenon during the electrodeposition and dissolution of Li metal in solvate ionic liquids

Akinori Miki, Kei Nishikawa, Go Kamesui, Hisayoshi Matsushima, Mikito Ueda, Michael Rosso

Journal of Materials Chemistry A. **9**, 14700–14709, 2021

12. **Study of Electrode Interface Phenomenon by Laser Interference Microscope**

Go Kamesui and Hisayoshi Matsushima

表面技術, Vol. 73, No. 7, P343-348, 2022

13. JSPS Research Fellowship DC1

Acknowledgments

First and foremost, I would like to express my deepest gratitude to my supervisor, Associate Prof. Matsushima, who has taught me not only academic skills such as scientific writing and data analysis but also provided invaluable life guidance. Thanks to his excellent letter of recommendation, I was fortunate to secure the JSPS DC1 fellowship. His wise counsel was particularly helpful when I was deliberating between industry employment and an academic research career. I am truly grateful for his patient guidance in leading me, despite my indecisiveness, to the completion of my doctoral degree.

I am deeply indebted to Dr. Nishikawa at NIMS for his invaluable advice regarding my research direction during my stay in Tsukuba. His careful and repeated revisions of my academic manuscripts greatly improved their quality. His guidance has been instrumental in my development as a researcher. I would also like to acknowledge the support from the Battery Platform at NIMS, which provided access to cutting-edge facilities and technical expertise crucial for my research.

My sincere appreciation extends to Professors Ueda and Kikuchi, who served as deputy examiners for my doctoral thesis. Their insightful comments and rigorous examination significantly enhanced the quality of my dissertation. Although their stringent feedback was sometimes challenging, the process of incorporating their suggestions strengthened both my research and character. I am grateful for their time and effort in thoroughly reviewing my thesis despite their busy schedules.

I am grateful for the opportunity to spend three months at the University of Oxford. Although the research itself faced various challenges, the experience taught me valuable lessons in perseverance and adaptability. The time spent in Oxford's historic academic environment, with its centuries of scholarly tradition, helped me develop a

deeper appreciation for the cultural aspects of scientific pursuit. While I encountered numerous setbacks in my experiments, these challenges ultimately strengthened my resilience and analytical capabilities. The experience of conducting research in a different cultural context broadened my perspective and contributed significantly to my growth as a researcher. I would like to express my sincere gratitude to Professor Fukunaka for his assistance in arranging my study opportunity at the University of Oxford. His support in establishing the connection with Oxford made this valuable international experience possible.

I would like to express my profound gratitude to the Japan Society for the Promotion of Science (JSPS) for their support through the DC1 fellowship program (Grant Number 23KJ0054). This fellowship not only provided essential financial support for my research activities but also enabled my stay at the University of Oxford. The prestigious nature of this fellowship boosted my confidence as a researcher and opened doors to valuable opportunities. The financial security it provided allowed me to focus entirely on my research without external pressures, significantly contributing to the successful completion of my doctoral studies. Furthermore, the fellowship's support for international research activities broadened my academic horizons and enriched my research experience.

Finally, I would like to express my gratitude to all laboratory members. Ms. Jinba provided invaluable assistance with travel arrangements and expense settlements during my study in the United Kingdom. Ms. Matsubara helped process my conference travel expenses efficiently. I am thankful to my fellow students for their companionship in the laboratory; our daily conversations provided welcome breaks from thesis writing. To Mr. Takahashi, the fourth-year undergraduate student who will continue my research: your

dedication to learning gives me confidence that you will develop into an outstanding researcher.

With everyone's support, I was able to complete my doctoral program. After graduation, I will begin my career in battery development at a major corporation in my hometown of Hiroshima. This decision reflects both my personal attachment to the region and my professional ambition to contribute to Japan's technological advancement from a local base. Starting my career in Hiroshima, a city that has risen from adversity to become a symbol of peace and progress, feels particularly meaningful. I aim to combine the fundamental research skills gained during my doctoral studies with practical industrial applications, bridging the gap between academic research and commercial technology development. As Japan faces increasing competition in the global battery industry, I aspire to grow into a leading technical expert who can help maintain and advance our country's position at the forefront of energy storage technology. Looking ahead, I hope to develop into a professional who can not only drive technological innovation but also mentor the next generation of engineers and researchers. The knowledge, skills, and values I have gained through this doctoral program will serve as the foundation for this journey. I am deeply grateful to everyone who has supported me in reaching this point, and I look forward to repaying their faith by contributing to society through my future work.

February 2025